

POLITECNICO DI TORINO
co-directed with
ECOLE POLYTECHNIQUE

SCUOLA INTERPOLITECNICA DI DOTTORATO

Doctoral Program in Material Sciences and Technology

Final Dissertation

**Preparation and characterization of metallic and
metal oxide nanoparticles for biomedical
applications**



Julia AMICI

Tutors
prof. Marco Sangermano
prof. Jean-Eric Wegrowe

Co-ordinator of the Research Doctorate Course
prof. Claudio Badini

February 28th, 2013

Index

Introduction	1
1. Nanoparticles for biomedical applications	5
1.1 Different nano-vectors	5
1.1.1 Nanocarriers	5
1.1.2 Magnetic nanoparticles.....	8
1.1.3 Gold nanoparticles.....	14
1.1.4 Hollow gold nanoparticles.....	18
1.1.5 Gold nanoshell.....	20
1.2 Different therapies	22
1.2.1 Drug delivery.....	22
1.2.2 Hyperthermia.....	26
1.2.3 Photothermal therapy	29
References	33
2. Nanoparticles properties for biomedical applications	43
2.1 Biocompatibility	43
2.2 Stealthiness	46
2.3 Targeting	49
References	52
3. Nanoparticles preparation strategies for biomedical applications.....	59
3.1 Photopolymerization.....	59
3.2 Click chemistry	65
3.2.2 Thiol-ene addition	66
3.2.3 Huisgen 1,3-dipolar cycloaddition	72
3.3 Emulsion polymerization.....	78

References 85

4. Materials and Methods 91

4.1 PEG coated magnetite nanoparticles via photopolymerization 91

4.1.1 Materials 91

4.1.2 Synthesis of Fe₃O₄ nanoparticles..... 91

4.1.3 Polymeric coating of Fe₃O₄ nanoparticles..... 92

4.1.4 Characterization techniques..... 92

4.2 PEG coated magnetite nanoparticles via UV-thiol-ene addition reaction 94

4.2.1 Materials 94

4.2.2 Synthesis of Fe₃O₄ nanoparticles..... 94

4.2.3 Vinyl surface functionalization of magnetite nanoparticles 95

4.2.4 Polyethyleneglycol coating of vinyl functionalized Fe₃O₄ nanoparticles 96

4.2.5 Characterization techniques..... 96

4.3 Polymer grafting onto magnetite nanoparticles via click-reaction 97

4.3.1 Materials 97

4.3.2 Synthesis of Acetylene End-Functionalized PCL..... 98

4.3.3 Synthesis of Acetylene End-Functionalized PEG 98

4.3.4 Synthesis of Magnetite nanoparticles 99

4.3.5 Functionalization of Magnetite nanoparticles with (3-Bromopropyl)trimethoxysilane 99

4.3.6 Azidation of Bromine-functionalized Magnetite nanoparticles 100

4.3.7 Functionalization of Azide-magnetite nanoparticles with a-PCL via Click Reaction 100

4.3.8 Functionalization of the azide-magnetite nanoparticles with alkyne-PEG via Click reaction 100

4.3.9 Characterization techniques..... 101

4.4 Photochemical synthesis of gold-PEG core-shell nanoparticles..... 102

4.4.1 Materials 102

4.4.2 Synthesis of gold nanoparticles 102

4.4.3	Characterization techniques	103
4.5	Hollow-gold nanoparticles coated with Poly(ethylene glycol) methyl ether thiol.....	104
4.5.1	Materials	104
4.5.2	Preparation of hollow gold nanoparticles.....	104
4.5.3	Coating of hollow gold nanoparticles with Poly(ethylene glycol) methyl ether thiol.....	105
4.5.4	Characterization techniques	106
4.6	SiO ₂ @Au nanoshell coated with Poly(ethylene glycol) methyl ether thiol	106
4.6.1	Materials	107
4.6.2	Preparation of SiO ₂ nanoparticles (Stöber method – 110 nm) ..	107
4.6.3	Functionalization of SiO ₂ nanoparticles with (3-aminopropyl) triethoxysilane (APTES)	108
4.6.4	Synthesis of gold nanoparticles (GNPs).....	108
4.6.5	Functionalization of SiO ₂ -APTES nanoparticles with GNPs....	108
4.6.6	GNPs reduction on SiO ₂ -APTES nanoparticles surface	109
4.6.7	Preparation of SiO ₂ nanoparticles (Stöber method – 25-65 nm)	109
4.6.8	Coating of Sample with Poly(ethylene glycol) methyl ether thiol	111
4.6.9	Characterization techniques	111
	References	112
5.	Hyperthermia	113
5.1	PEG coated magnetite nanoparticles via photopolymerization	113
	Conclusions	119
5.2	PEG coated magnetite nanoparticles via UV-thiol-ene addition reaction	120
	Conclusions	128
5.3	Polymer grafting onto magnetite nanoparticles via click-reaction...	129
	Conclusions	139
	References	140

6. Photothermal therapy	143
6.1 Photochemical synthesis of gold-PEG core-shell nanoparticles.....	143
Conclusions	150
6.2 Hollow-gold nanoparticles.....	151
Conclusions	157
6.3 SiO ₂ @Au nanoshell	158
Conclusions	172
References	172
Conclusions	175
List of Publications	179
Acknowledgements	181

Nomenclature

ABPP: Activity Based Protein Profiling

AGFM: Alternated Gradient Field Magnetometer

a-PCL: acetylene-polycaprolactone

a-PEG: acetylene-polyethylene glycol

APTES: (3-Aminopropyl)triethoxysilane

ATR: Attenuated Total Reflectance

BBB: Blood Brain Barrier

BP: Benzophenone

CMC: Critical Micelle Concentration

CT: Computed Tomography

DCC: *N,N'*-dicyclohexylcarbodiimide

DLS: Dynamic Light Scattering

DMAP: 4-dimethylaminopyridine

DMF: *N,N*-Dimethyl formamide

DMPA: Dimethoxyphenyl Acetophenone

DNA: Deoxyribonucleic acid

EGFR: Epidermal Growth Factor Receptor

EPR: Enhanced Permeation and Retention

FT-IR: Fourier Transform - Infra Red Spectroscopy

GNPs: Gold Nanoparticles

HGNs: Hollow Gold Nanoparticles

ICP: Inductively Coupled Plasma

IR: Infra Red

LSPR: Localized Surface Plasmon Resonance

MeO-PEG-SH: Polyethylene Glycol Methyl Ether Thiol

MFH: Magnetic Fluid Hyperthermia

MNPs: Magnetic Nanoparticles

MRI: Magnetic Resonance Imaging

MSH: Melanocyte Stimulating Hormone

MW: Molecular Weight

MWCO: Molecular Weight Cut Off

NIR: Near Infra Red

NPs: Nanoparticles

PCL: Polycaprolactone

PEG: Polyethylene Glycol

PEGDA: Polyethylene Glycol di-Acrylate

PEG-SH: Polyethylene Glycol di-Thiol

PGLA: Poly(D,L-lactic/glycolic acid)

phr: per hundred resins

PLA: Poly(D,L-lactic acid)

PMDETA: *N,N,N', N',N''*-pentamethylethylenetetramine

PTA: Photothermal Ablation

RES: Reticulo Endothelial System

SERS: Surface Enhanced Raman Spectroscopy

SPION: Superparamagnetic Iron Oxide Nanoparticles

SPR: Surface Plasmon Resonance

TEM: Transmission Electron Microscopy

TEOS: Tetraethoxysilane

TGA: Thermogravimetric Analysis

THF: Tetrahydrofuran

THPC: Tetrakis (Hydroxymethyl) Phosphonium Chloride

UV: Ultra Violet

VSM: Vibrating Sample Magnetometer

VTMS: Vinyltrimethoxysilane

XPS: X-ray Photoelectron Spectroscopy

Introduction

Two of the 21st century most promising technologies are biotechnology and nanotechnology. This science of nanoscale structures deals with the creation, investigation and utilization of systems that are 1000 times smaller than the components currently used in the field of microelectronics. Convergence of these two technologies results in growth of nanobiotechnology. This interdisciplinary combination can create many innovative tools. The biomedical applications of nanotechnology are the direct products of such convergence.

Indeed, due to their unique size-dependent properties, nanomaterials have the potential to revolutionize the detection, diagnosis, and treatment of diseases by offering superior capabilities compared to conventionally used materials. Today nanomaterials have been designed for a variety of biomedical and biotechnological applications, including biosensors, enzyme encapsulation; neuronal nanotechnology, on the other hand, is based on the introduction of novel nanomaterials which can result in revolutionary new structures and devices using extremely biologically sophisticated tools to precisely position molecules. Nanotechnology in biomedical sciences presents many revolutionary opportunities in the fight against all kinds of cancer, cardiac and neurodegenerative disorders, infection and other diseases. Utility of nanotechnology to biomedical sciences imply creation of materials and devices designed to interact with the body at sub-cellular scales with a high degree of specificity. This could be potentially translated into targeted cellular and tissue-specific clinical applications aimed at maximal therapeutic effects with very limited adverse-effects.

Nanoparticles are part of the family of devices nanotechnology had given birth to. By their size and morphologic properties they encounter a large panel of different applications, biomedical applications are part of this panel. These specific nanoparticles can cover different functions from diagnosis to direct treatment; more specifically they can be used as carriers for specific delivery of drugs or as vector for specific therapies. In a first chapter different kind of

nanoparticles will be described in a first time, and the related therapy they apply to will be explained in a second time.

In order to be used for this specific kind of application, the nanoparticles should comply with a certain number of requirements and specifications. To this end, not only the materials used for their preparation, but also the method employed should satisfy such requirements. In a second chapter, the requirements will be listed and their implications will be explained, and in the third chapter specific preparation methods meeting these criteria will be described.

A lot of research is currently being conducted on this specific topic, for this reason it is a challenge to constantly find new methods of preparation and new materials meeting all the previously described requirements and in the same time bringing and improvement in the potential treatments.

In the fourth chapter will be described the materials and methods I used to prepare devices and take up that challenge.

Firstly, a new fast and convenient method is reported for preparing magnetic nanoparticles with a Fe_3O_4 core and a Poly(ethylene glycol)-diacrylate shell in water. A reduction coprecipitation method was used to obtain Fe_3O_4 in aqueous solution whereas the PEGDA coating was obtain via photochemical reaction at room temperature in an initiator free aqueous system. The fact that this method is solvent free and initiator free makes it ideal for biomedical applications.

Secondly, magnetite nanoparticles were coated following a previous surface functionalization. The Fe_3O_4 nanoparticles were obtained as before and further stabilized with citric acid. Afterwards nanoparticles surface was modified by a silanization reaction with vinyltrimethoxysilane involving magnetite hydroxyl groups. Vinyl functionalized nanoparticles were coated with poly (ethylene-glycol) (PEG) using PEG dithiol (PEG-SH) under UV irradiation. Thiol-ene is a free-radical reaction that proceeds by a step-growth mechanism, involving two main steps, a free-radical addition followed by a chain transfer reaction; this reaction is well known for occurring in absence of any radical photoinitiator making it ideal for eventual biomedical applications.

Thirdly, the use of “click” reactions for preparing magnetic NPs with Fe_3O_4

core and different biocompatible polymeric shells is reported. Magnetite nanoparticles were obtained following the same procedure that in the first two studies. As a next step, magnetic nanoparticles surface was modified by a silanization reaction with (3-bromopropyl)trimethoxysilane in order to introduce bromine groups on the particles surface. Afterwards the bromine groups were converted to azide groups by the reaction with sodium azide in order to obtain azide groups to take part to click reaction with alkyne functionalized polymers. For this reason, acetylene functionalized poly(ethylene glycol) (a-PEG) and poly(ϵ -caprolactone) (a-PCL) were synthesized and grafted onto the surface of azide functionalized nanoparticles via “click” reaction to obtain monodisperse magnetic nanoparticles. The peculiar characteristics of this method make it ideal for biomedical applications.

Fourthly, a new, fast and convenient method for preparing gold nanoparticles with a poly(ethylene glycol)-diacrylate (PEGDA) shell in water is reported. Polyethyleneglycol (PEG) was used as hydrophilic monomer in emulsifier-free emulsion polymerization to form polymeric nanoparticles by the UV-induced process. At the same time, gold was generated as the core of the PEG nanospheres by the reduction of HAuCl_4 activated through the radical photogenerated from 2-hydroxy-2-methyl-1-phenyl-1-propanone. This one-step procedure is very easy to implement and fast. Moreover, the fact that this method is performed in water makes it ideal for biomedical applications.

Fifthly, hollow gold nanoparticles were prepared and coated with Poly(ethylene glycol) methyl ether thiol. In a first time, cobalt nanoparticles were prepared by reduction of cobalt salts and in a second time gold salts were reduced on the surface of cobalt nanoparticles forming a gold shell while consuming the cobalt, leaving at the end of the reaction a hollow gold nanoparticles. Successively these devices were coated with the polymer taking advantage of the natural affinity between thiol groups and gold.

Sixthly, gold nanoshell were prepared and coated with Poly(ethylene glycol) methyl ether thiol. Gold nanoshells are constituted by a silica core and a gold shell. Silica nanoparticles were obtained by the well-known Stöber method,

then gold seeds (3 nm diameter) were grafted on the surface of these silica nanoparticles and successively grown by gold salts addition until obtaining a continuous and homogeneous gold shell. In the end these devices were coated with the polymer taking advantage of the natural affinity between thiol groups and gold.

The fifth and sixth chapters describe the characterization of these devices correlated to their potential applications.

1. Nanoparticles for biomedical applications

Most treatments distribute to the whole body, which gives rise to general toxicity and poor patient acceptance. Since transporting across the membrane is one of the key obstacles therapeutic treatments must overcome to effectively function in the cell, potential treatments should be designed taking into account these specific membrane-transport properties [1]. This aim can be reached by using vectors. However, although a variety of treatments have been designed as vectors with their own advantages and limitations, scientists are still learning to optimize delivery to enhance the bioavailability of the treatment toward diseased cells, promoting the required response while minimizing side-effects. Therefore, in the field of targeted therapies the way to develop treatment vectors able to target defined cells by means of specific recognition mechanisms, and to overcome biological barriers, has become a common goal to reach.

1.1 Different nano-vectors

Nanovectors are multifunctional organic and inorganic nanoparticles, nanowires, or nanotubes. In the laboratory setting, nanovectors can improve both the targeted delivery of anticancer drugs and the targeted localized killing of cancerous cells [2]. Moreover nanovectors have the potential to be a generic platform for different types of cancer treatments localized on a unique device. Last but not least, in near future nanovectors could also give rise to nanosurgical tools for surgical treatments of cancer. The main characteristics of the vectors are biocompatibility and biodegradability so as to be easily eliminated afterwards and avoid any toxic accumulation.

1.1.1 Nanocarriers

Therapeutic efficacy of a drug is linked to its pharmaco-kinetic behavior. The drug should reach quickly and in sufficient quantity its target and remain active on the same site long enough to complete its therapeutic action. Furthermore, the drug should be able to avoid accumulating in healthy tissues and organs in

order not to cause toxic effects. In this way it would be possible to decrease side effects as well as drug concentration. On the contrary, very often, the drug distribution in the body is not the one expected: drug quantity is too low on the target site and too high in healthy tissues causing damages. Different strategies have been studied in order to increase the drug concentration on the target site avoiding contact with healthy tissues. One of these strategies consists in linking the drug to a vector. The drug is encapsulated in this vector, which is able to transport it to the target and release it in a controlled way. Nanoparticles are one of the many vectors that can be used to this aim and have been widely studied lately.

Nanoparticles are colloidal systems, generally constituted from polymer, preferentially biodegradable, from natural or synthetic origins. They can be matricials (nanospheres) or empty (nanocapsule) as can be seen in Figure 1.1.

In the first case the drug can be molecularly dispersed inside the polymeric matrix and then be released either by osmotic diffusion from inside the nanoparticles to the outside, or by biodegradation of the device inside the organism.

Nanocapsules, on the other hands, are constituted from a generally liquid core and a thin polymeric shell.



Figure 1.1: schematic representation of a nanosphere (A), and a nanocapsule (B)

Compared to other colloidal systems, such as liposomes, nanoparticles are characterized by a higher stability in biological fluids. This behavior can be explained by their polymeric structure which is a lot more stable than the lipidic bilayer of the liposomes. Moreover, nanoparticles constitute a very versatile colloidal system; as a matter of fact a wide range of biocompatible polymers is available allowing to choose the most suitable system for the

controlled release of the encapsulated drug, adjusting the vector degradation. Furthermore, the surface of nanoparticles-based vectors designed for drug delivery can be decorated with various targeting agents or biological materials, such as antibodies, imaging agents or reporter molecules which can be used to target a specific receptor in malignant cells, image these cells and trace the device during the treatment.

Depending on the materials of preparation, nanoparticles have been synthesized most frequently by three methods: dispersion of preformed polymers, polymerization of monomers and ionic gelation or coacervation of hydrophilic polymers [3]. The application of nanoparticulate delivery systems should be applied to sites as varied as brain cells or epithelial cells and includes not only drug delivery, but also delivery of peptides, proteins or whole genes.

The potential applications of colloidal drug carriers by the intravenous route can be summarized as concentrating drugs in accessible sites, rerouting drugs away from sites of toxicity and increasing the circulation time of labile or rapidly eliminated drugs (e.g. peptides and proteins).

Liposomes or nanoparticles can be used to concentrate antibiotics at the site of infection for direct treatment of bacterial and parasitic infections, particularly when the microorganism is within the lysosomes [4]. For example, nanoparticles containing ampicillin were more effective than the free drug against both *Salmonella typhimurium* and *Listeria monocytogenes*. Colocalization of the particles and bacteria was seen in *Salmonella* infected macrophages *in vitro* [4].

Colloidal carriers can also be used to divert drugs from sites of toxicity after intravenous administration. For example, the anticancer drug doxorubicin (adriamycin) is active against a wide spectrum of tumors, but provokes dose-limiting cardiotoxicity. Encapsulation within liposomes or nanoparticles reduces this toxicity, by reducing the amount of drug which reaches the myocardium [5][6].

A corollary is that concentrations of doxorubicin in the liver increase considerably. In one study in mice, this was not associated with any overall toxicity [6]. However, another group reported a temporary depletion of Kupffer

cells and hence the ability to clear bacteria, in rats, which was less marked when long-circulating liposomes were used [7]. A systematic study using unloaded nanoparticles confirmed a reversible decline in the phagocytic capacity of the liver after prolonging dosing, as well as a slight inflammatory response [8]. Thus, altered distribution may generate new types of toxicity and this must be borne in mind when developing carrier systems.

In recent years, gene therapy is also opening up a possibility for treating some incurable diseases. Broadly defining, gene therapy is the insertion of genes into specific cells and/or tissues to treat a defect, as example a hereditary disease in which a deleterious mutant allele is replaced with a functional one. Although the technology is still in its beginning, it has been used with some success [9] and has the potential to change medical science dramatically in the future.

1.1.2 Magnetic nanoparticles

Lately, magnetic nanoparticles (MNPs) have attracted attention because of their potential application not only in drug delivery and magnetic resonance imaging (MRI) but also in magnetic hyperthermia. MNPs for such biomedical application should be hydrophilic and biocompatible [10]. To that end, variety of inorganic nanoparticles such as magnetic nanoparticles, metal nanoparticles and metal oxide nanoparticles have gained increasing interest in the field of material sciences because of their specific optical, electronic and magnetic properties [11]. Among these particles, iron oxide nanoparticles such as magnetite, or its oxidized form maghemite, are the most biocompatible agents. These particles are typically coated with a biocompatible polymer to prevent their aggregation and biodegradation for *in vivo* applications [12].

Magnetite (Fe_3O_4) is a common magnetite oxide that has a cubic inverse spinel structure [13][10]. The most common method to prepare magnetite nanoparticles consists in mixing solutions of FeCl_3 and FeCl_2 , followed by precipitation of magnetite by addition of a base [14]. Fe_3O_4 nanoparticles may then be superficially oxidized to the more stable maghemite ($\gamma\text{-Fe}_2\text{O}_3$) by addition of ferric nitrate to the colloidal suspension [15]. Size, shape and composition of iron oxide nanoparticles depend on the operating conditions

(pH, nature of the base, Fe²⁺ and Fe³⁺ ratio...). The content of magnetite and maghemite in these nanoparticles can be estimated by techniques such as Mössbauer spectroscopy [16] and X-ray diffraction [17]. Moreover, it is possible to deduce the magnetite/maghemite ratio in the solid phase of ferrofluids from Raman spectra [18] by using the ratio of their respective characteristic vibrational bands (671 cm⁻¹/ 721 cm⁻¹). It has also been observed that exposure to oxygen and elevated temperatures favored the formation of undesirable species like antiferromagnetic hematite. Usually, the iron oxide nanocrystals are nearly spherical and their size is most often described in the literature to be 6-12 nm.

The iron oxide nanoparticles can be dispersed in suitable solvents to form homogeneous suspensions called ferrofluids or magnetic fluids. They present a very interesting amphoteric character (Figure 1.2) due to the presence of hydroxyl groups at their surface [15]. Because the stability of an aqueous ferrofluid is mainly due to electrostatic repulsion between charged particles, they flocculate around the point of zero charge (PZC, established around pH 7). Typically, the iron oxide nanoparticles are used as cationic ferrofluids, which means that the particle surface is positively charged and accompanied by anionic counterions (usually nitrates). A PZC close to physiological pH should not necessarily be considered an inconvenient as the particles still have to be coated before injection. Thus, the iron oxide nanoparticle is just a precursor, and its surface properties need only to be compatible with coating and eventual drug loading.

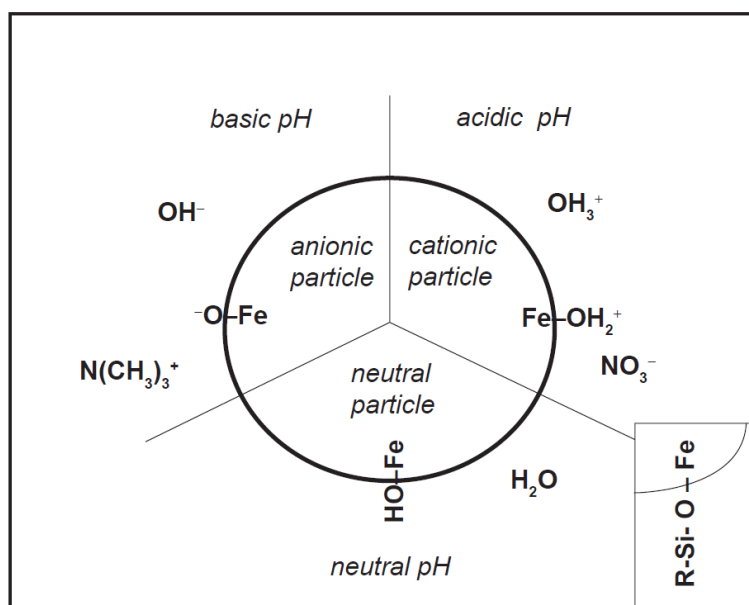


Figure 1.2: Diagram of surface properties of iron oxide nanoparticles. Insert: surface silanization

As the nanoparticles have large surface area/volume ratios, they tend to adsorb plasma proteins and agglomerate *in vivo*. As a result, without coating the ferrite nanoparticles are rapidly cleared by macrophages in the reticulo-endothelial system.

For this reason, usually, the iron oxide nanoparticles constitute the core of the final forms of therapeutic nanovectors. From a physiochemical point of view, the main objective is the preparation of magnetic nanoparticles consists in a strict control of particle size and colloid stability/dispersibility under physiological conditions. These properties can be modulated by coating the particles in 2 different ways: either the iron oxide nanoparticles are physically incorporated in a polymer matrix or their surface is functionalized with polymer molecules (see Figure 1.3).

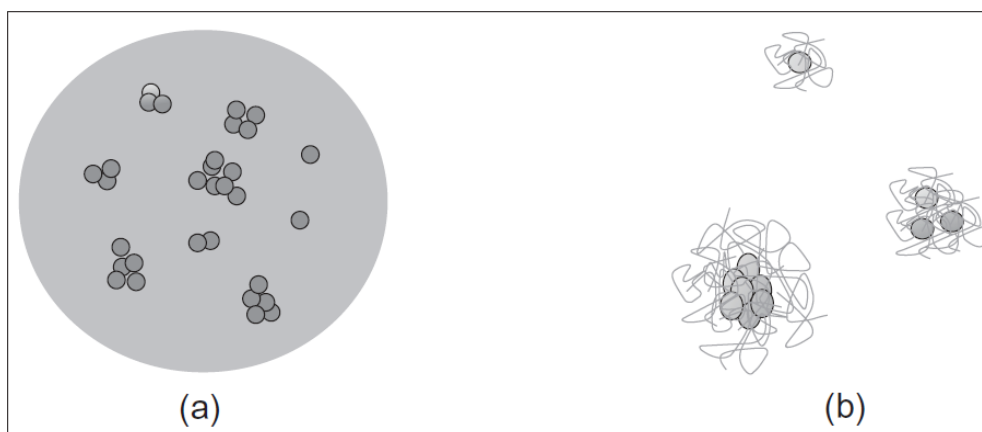


Figure 1.3: Schematic representation of the coating of iron oxide nanoparticles with polymers via encapsulation (a) or via surface treatment (b). In this latter case, a polymer layer may form around individual iron oxide particles or around aggregates.

After coating, the particles size is increased, but it still should remain in the sub-micron range. In this case, they will not block vessels and capillaries and thus avoid embolization [19]. Moreover, size and surface of resulting particles are determinant with respect to pharmacokinetics *in vivo*, where major limitations are quick blood clearance and non-specific uptake by macrophages. To maximize circulation times and targeting ability, the optimal size should be less than 100 nm in diameter and the surface should be hydrophilic [20][21]. Ideally, these properties should render the particles “furtive”, which means that they are not cleared by the reticulo-endothelial system.

As we noted above, one possibility of coating is to encapsulate the magnetic particles in a solid polymer matrix. Alternatively, the hydroxyl groups at the surface of iron oxide nanoparticles can be used to directly anchor active molecules or polymers. To enrich the choice of possible reactions, one can use silane (Figure 1.2 insert) as coupling intermediated: silanes form Fe-O-Si bonds with the particle surface and offer on their opposite end functional groups (amines, thiols) that can interact with therapeutical agents, biologically relevant ligands and polymers [22].

To increase both the stability and furtivity (or stealthiness) of magnetic suspensions, iron oxide nanoparticles are often coated with hydrophilic polymers adsorbed or chemically attached to their surface. Polyethylene glycol

(PEG) seems to be one of the most appropriate ones because of its unique properties such as hydrophilicity, flexibility, nontoxicity, and non immunogenicity.

As a matter of fact, data from physico-chemical characterization indicate that coating with PEG efficiently reduces nanoparticles agglomeration [23]. A first study to demonstrate that polyethylene oxide exhibits low protein adsorption was performed by Jeon and Andrade [24]. Consecutively to this study, many authors tried to link such polymers to the surface of different kinds of nanoparticles with the hope to decrease their uptake by the mononuclear phagocyte system [25]. Zhang et al [26] immobilized silane modified PEG on the surface of magnetite nanoparticles. A rather similar approach was proposed for coating magnetic nanoparticles with PEG by Butterwoth et al [27].

Using fluorimetry, confocal fluorescence microscopy and inductively coupled plasma emission spectroscopy (ICP), Zhang et al [26] measured the uptake of their magnetic nanoformulations in breast cancer cells (BT20 cells) and in mouse macrophage cells (RAW 264.7). The results of this study suggest that PEG coating of iron oxide nanoparticles limits protein adsorption on their surface and avoids their recognition by macrophages. Furthermore, PEG-modified surfaces facilitated incorporation of nanoparticles by cancer cells, probably due to high affinity of the polymer to cellular membranes.

The main difficulty with using PEG for the formulation of nanovectors is that, except for the terminal (hydroxyl) group, this long-chain polymer lacks functional groups useful to attach therapeutic agents and/or specific ligands. Zhang circumvented this difficulty by introducing PEG modified with a trifluoroethylester-silane terminus [28]. This modification allowed them to bind folic acid ligand to PEG-treated magnetic nanoparticles. Since folate receptors are overexpressed on membrane of many cancer cells, the folic acid ligand should provide better access of nanovectors to tumor. Rupta et. al also studied iron oxide nanoparticles modified with PEG and found them to be internalized within lysosomes of fibroblasts [29]. In a different way, Acar covered iron oxide nanoparticles with PEGylated polymers [30]. In that case the coating consisted of two layers, the inner layer composed by an ionic surfactant such as

10-undecenoic acid, and an outer layer made of PEG modified by etherification with the same surfactant. These particles were synthesized according to various modes of preparation and present really interesting sizes for a possible administration *in vivo*.

As an alternative to PEG, natural polymers such as dextran, chitosan or starch can be attached to the surface of iron oxide nanoparticles in order to minimize the adsorption of proteins and to protect them for macrophages [23]. Dextran is a polymer of anhydroglucose having mainly alpha-D(1-6) linkages with side chains attached to the 3-positions of the backbone glucose units. Thirty years ago, Molday and Mackenzie prepared iron oxide nanoparticles modified with dextran [31]. They mixed a solution of ferrous chloride and ferric chloride with dextran under alkaline conditions. Similar preparations, where dextran was physically adsorbed, were then studied by various authors [32][33]. Recently, Xu et al [34] contributed to optimize the protocol by their study of various operating conditions. The authors reported that reaction time and size of the polymer are the main parameters essential for the quality of preparations. The high biological tolerance [35] of these modified particles has been demonstrated and justified their extensive use as contrast agents for magnetic-resonance imaging (MRI).

The main interest of these nanoparticles is based on their superparamagnetic behavior: superparamagnetic iron oxide nanoparticles (SPION) are small synthetic γ -Fe₂O₃ or Fe₃O₄ particles with a core size of < 10 nm and an organic or inorganic coating. If the crystal size is small enough the thermal energy kT (where k is Boltzmann's constant and T is the absolute temperature) may be sufficient to cause fluctuations of the magnetization direction. The term "superparamagnetism" is used to infer an analogy between the behavior of the small magnetic moment of a single paramagnetic atom and that of the much larger magnetic moment of a nanosized magnetic particle which arises from the coupling of many atomic spins. After eliminating the magnetic field, the particles no longer show magnetic interactions; a feature that is important for their usability for medical application, the particles are well dispersed in a liquid, normally in water, or form composites with organic or inorganic

matrices, the so-called beads. Superparamagnetic magnetization is, compared to normal paramagnetic materials, much higher and can reach nearly the magnetization saturation of ferromagnetic iron oxide. This behavior allows the tracking of such particles in a magnetic field gradient without losing the advantage of a stable colloidal suspension. Additionally, applying an alternating magnetic field, heating of the particles can be observed based on the Néel relaxation mechanism. In the Néel mechanism, the magnetic moment of the nanoparticle, originally locked along the crystal easy axis rotates away from that axis toward the external field. The Néel mechanism is analogous to the hysteresis loss in multi-domain magnetic particles whereby there is an “internal friction” due to the movement of the magnetic moment in an external field that results in heat generation [36][37].

1.1.3 Gold nanoparticles

Gold nanoparticles (AuNPs) possess many unique features and have been investigated in a variety of imaging related areas, such as computed tomography (CT), photoacoustics and surface-enhanced Raman spectroscopy (SERS). AuNPs have been brought to the forefront of cancer research in recent years because of their easy synthesis and surface modification, strongly enhanced and tunable optical properties, as well as excellent biocompatibility. High quality, high yield and size controllable colloidal gold can be quickly prepared by the well-known citrate reduction method [38][39][40]. Synthesis of AuNPs has been well established, and those in the forms of spheres [41][42][43], cubes [44], rods [45][46], cages [47] and wires [48] can now be acquired with accurate quality control and in large quantity. Such morphology control is important as it greatly influences the physical properties of the products and in turn affects their role as imaging probes. For instance, 10 nm spherical AuNPs have characteristic surface plasmonic absorption at around 520 nm. Increasing the particle size leads to some, but not dramatic, red-shift of the particle absorption spectrum; the maximum absorption of 48.3 and 99.4 nm AuNPs is at 533 nm and 575 nm, respectively [49]. Changing the nanoparticle shape to rod-like, on the other hand, can push the absorption to the

NIR region (650–900 nm), which suggests their role as probes in photoacoustic imaging or mediators in photothermal therapeutics [50]. The AuNPs of different shapes and structure [51] including gold nanorods [52][53][54] (Figure 1.4) silica/gold nanoshells [55] (Figure 1.5 A) and hollow Au NPs [56] (Figure 1.5 B) all show largely red-shifted properties, boosting their values in photothermal cancer therapy [57][58][59]. The strongly enhanced radiative properties such as absorption, scattering and plasmonic field for surface enhanced Raman of adjacent molecules make them extremely useful as well for molecular cancer imaging [60][61] (Figure 1.4).

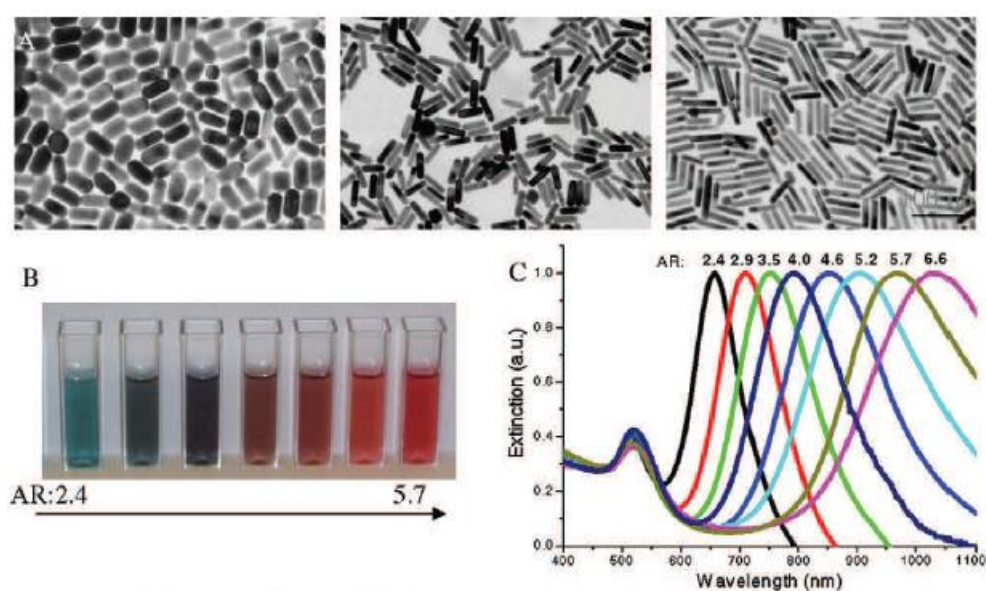


Figure 1.4: Tunable optical properties of gold nanorods by changing the aspect ratios. Gold nanorods of different aspect ratios exhibit different dimensions as seen by TEM (A), in different color (B) and different SPR wavelength (C) [62][63]

AuNPs have interested scientist for decades largely due to the ability of optical tuning by synthetic controlling of the particle shape, composition and structure. As predicted by Gan theory in 1915 [64], when the shape of AuNPs change from spheres to rods (Figure 1.4 A), the SPR band is split into two bands: a strong band in NIR region corresponding to electron oscillations along the long axis, referred to as longitudinal band, and a weak band in the visible region at a wavelength similar to that of gold nanospheres, referred to as transverse bands. While the transverse band is insensitive to the size changes, the longitudinal

band is red shifted largely from the visible to near-infrared region with increasing aspect ratios (Length/Width), causing the color changes from blue to red (Figure 1.4 B and C). Currently, the aspect ratio can be precisely controlled by changing the experimental parameters such as the catalyst of silver ions in the seed-mediated growth method developed by Murphy and El- Sayed groups [65][66]. The nanorods are formed by asymmetric growth of small gold spheres in the presence of shape-forming surfactants, weak reducing agents and the catalysts [67].

Besides the shape factor for optical tuning into NIR region, structure variation results in similar phenomenon. Two examples are the gold nanoshells (Figure 1.5 A) and nanocages (Figure 1.5 B). Au nanocages are a type of hollow and porous gold nanostructures which are formed by a galvanic replacement reaction between silver nanocubes and auric acid in aqueous solution [68]. Simultaneous deposition of gold atoms and depletion of silver atoms results in Au nanoshells which then anneal to generate smooth hollow and porous structures. General size of the nanocages is around 50 nm edge width with few nanometers walls and holes for SPR wavelength around 800 nm [69]. By controlling the amount of auric acid solution, the SPR of gold nanocages could be tuned to NIR region with specified wavelength. The total light extinction of Au nanocages with SPR around 800 nm is dominated by absorption, which makes them suitable for photothermal therapy [70].

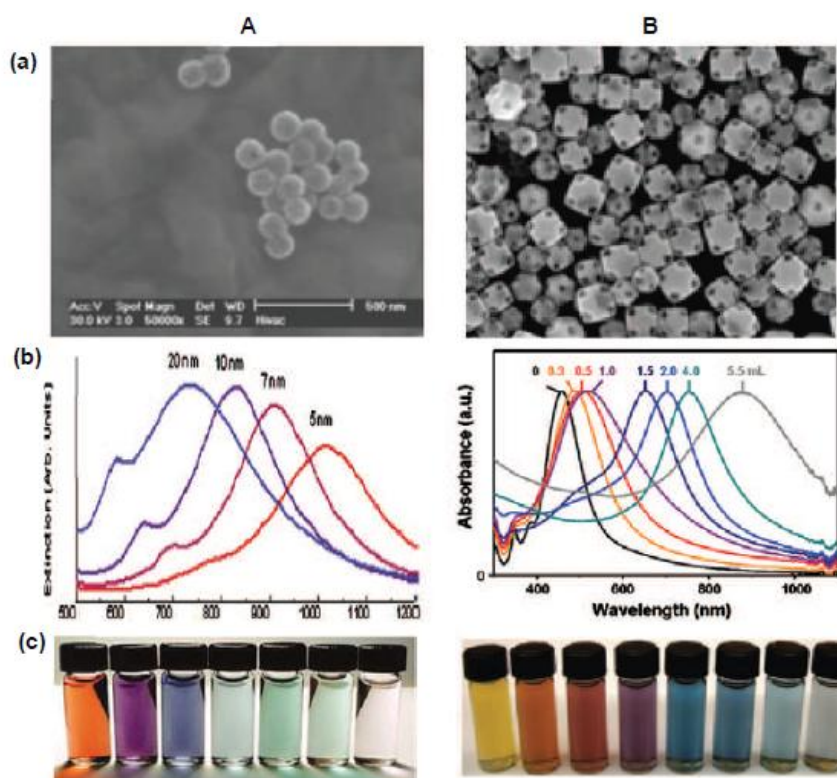


Figure 1.5: TEM images (a), absorption spectra (b), and physical appearance (c) of the tunable optical properties of gold nanoshells(A) by changing the shell thickness [71] and gold nanocages (B) by changing the auric acid in the synthetic procedure [72]

The bioapplications of AuNPs in life sciences can be classified into four areas: sensing, labeling, delivery, and heating.

AuNPs can be used as sensors. Their optical properties can change upon binding to certain molecules, allowing the detection and quantification of analytes. The absorption spectra of AuNPs change drastically when several particles come close to each other. In the business of colloids aggregation is actually rather annoying but it can be exploited for very sensitive DNA detection, even of a single-base mismatch.

Secondly, certain properties of the particles are exploited to generate contrast to use as labeling. For example in transmission electron microscopy, the strong electron absorbing properties of gold nanoparticles make them suitable as a stain for samples with poor contrast, such as tissue samples. Their small size and the possibility of functionalizing the particles, for instance with antibodies

(immunostaining), mean that they also provide extremely high spatial resolution and specificity in many labeling applications. Similarly, the particles' optical properties - strong absorption, scattering and especially plasmon resonance – make them of value for a large variety of light-based techniques including combined schemes such as photothermal or photoacoustic imaging. In addition, gold nanoparticles can be radioactively-labeled by neutron activation, which allows for very sensitive detection, and used as an x-ray contrast agent.

Thirdly, AuNPs can serve as carriers for drug and gene delivery. Biologically active molecules adsorbed on the particle surfaces can be guided inside cells and released. DNA delivery, for instance, is the basis for gene therapy.

Finally, their strong light absorbing properties makes AuNPs suitable as heat-mediating objects; the absorbed light energy is dissipated into the particles' surroundings, generating an elevated temperature in their vicinity. This effect can be used to open polymer microcapsules, for example, for drug delivery purposes. Moreover, appropriately functionalized nanoparticles can bind specifically to certain cells, and find a use in cancer targeting and hyperthermal therapy by heating the particle-loaded tissue in order to destruct the malignant cells.

1.1.4 Hollow gold nanoparticles

Recently, a new class of molecular-specific photothermal coupling agents based on hollow gold nanoparticles (HGNs) has been developed [73][74]. The synthesis process of such nanostructures is based on templating using cobalt (Co) nanoparticles as initial seeds via a galvanic reaction with Au³⁺ ions. On the basis of theoretical calculation, a large diameter and thinner shells result in redder SPR peaks. Moreover, the SPR bandwidth depends sensitively in the uniformity of the shell diameter and thickness, and poorer uniformity results in broader spectral width, thus the combination of shell diameter and thickness determines the peak position of the SPR absorption [75]. Therefore, one can control the shell diameter and thickness to manipulate the color of the HGNs at will for different applications. In addition to the strong, narrow, and tunable

NIR absorption desired for PTA, the HGNs have small size (30-50 nm) and spherical shape, and both are highly desired for delivery and membrane penetration [76]. These HGNs have been successfully utilized in both *in vitro* and *in vivo* PTA of carcinoma and melanoma cancer cells [77][78]. In the carcinoma PTA study, HGNs were covalently attached to a monoclonal antibody directed at the epidermal growth factor receptor (EGFR) overexpressed in carcinoma cancer cells [77].

In the melanoma PTA study, the HGNs were stabilized with a PEG coating and attached with a melanocyte stimulating hormone (MSH) analogue, [Nle⁴,D-Phe⁷]α-MSH (NDP-MSH), which is a potent agonist of melanocortin type-1 receptor (MC1R) overexpressed in melanoma [78]. The intracellular uptake of the NDP-MSH conjugated PEGylated HGNs (MSH-PEG-HGNs) and the distribution of h-arrestin were examined in murine B16/F10 melanoma cells. The biodistribution of NDP-MSH-PEG-HGNs was assessed at 4h post intravenous injection in tumor bearing nude mice. The final results showed that the HGNs were specifically taken up by melanoma cells, which initiated the recruitment of h-arrestins, the adapters to link the activated G-protein-coupled receptors to clathrin, indicating the involvement of receptor-mediated endocytosis [78]. This resulted in enhanced extravasation of the NDP-MSH-PEG-HGNs from tumor blood vessels and their dispersion into a tumor matrix compared with non-specific PEGylated HGNs. Successful selective photothermal ablation of B16/F10 melanoma with targeted HGNs was confirmed by histologic and positron emission tomography.

Both *in vitro* and *in vivo* studies have shown that the HGNs are ideally suited for PTA applications because of their unique combination of spherical shape, small size (average outer diameter of 30-50 nm) as well as narrow, tunable, and strong absorption in the NIR region. Using a small molecular weight peptide as a targeting ligand and attaching it at the end of PEG chains, receptor-mediated active targeting of melanoma and efficient PTA with photothermal coupling agents *in vivo* have been shown, for the first time. Direct comparison with solid gold nanoparticles shows that the HGNs are, at least, eight times more effective, mainly due to much stronger NIR absorption and more effective

photothermal conversion. Both size and shape have been recognized to be critical in determining cell uptake of nanostructures [78].

1.1.5 Gold nanoshell

Metallic nanoshells are a new class of subwavelength optical components with geometrically tunable plasmon resonances, allowing materials to be specifically designed to match the wavelength required for a particular application. A metallic nanoshell is composed of a spherical dielectric core surrounded by a concentric metallic thin shell. By varying the core and shell dimensions, the nanoshell plasmon resonances can be fine-tuned all the way across the visible and infrared spectral regions. In 1998, Naomi Halas and coworkers at Rice University demonstrated that the nanoshell geometry could be experimentally realized by growing a thin layer of Au onto a spherical silica nanoparticle through seed-mediated electroless plating [79]. This synthetic method allows independent control over the core and the shell radii. The as-fabricated nanoshells exhibit LSPRs that can be tuned from the visible all the way into mid-infra-red.

Because nanoshells are spherically symmetric, their resonances can be analytically described by Mie theory. In 1951, Aden and Kerker [80] first proposed the model for simulating the scattering of electromagnetic waves from a composite spherical particle consisting of a metallic shell and a dielectric core based on the Mie Scattering theory. Neeves and Birnboim [81] proposed in 1989 that such a core-shell geometry could give rise to Localized Surface Plasmon Resonance (LSPR) modes with their wavelengths tunable over a broad range of the electromagnetic spectrum.

The geometry dependent nanoshell plasmon resonances result from the interaction between the essentially fixed frequency plasmon response of a sphere and that of a cavity (see Figure 1.6 A). The sphere and cavity plasmons are electromagnetic excitations at the outer and inner interfaces of the metal shell, respectively. Because of the finite thickness of the shell layer, the sphere and cavity plasmons interact with each other and hybridize in a way analogous to the hybridization between atomic orbitals. As illustrated in Figure 1.6 A, this

interaction results in the splitting of the plasmon resonance into 2 new resonances, the lower energy symmetric or “bonding” plasmon (ω_-) and the higher energy antisymmetric or “anti-bonding” plasmon (ω_+). The strength of the interaction between the sphere and cavity plasmons is controlled by the thickness of the metal shell layer (Figure 1.6 B).

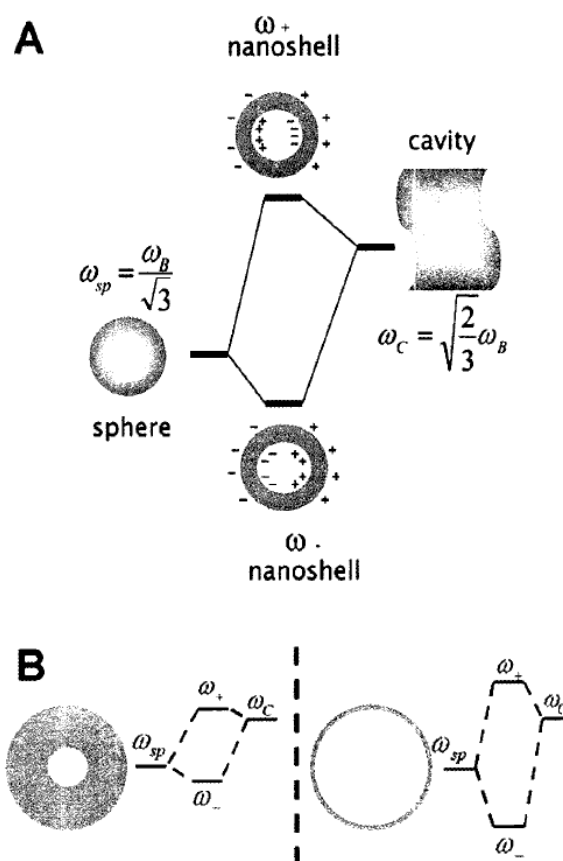


Figure 1.6: (A) Energy level diagram depicting plasmon hybridization in metal nanoshells resulting from interacting sphere and cavity plasmons. the 2 hybridized plasmon modes are an anti-symmetric or "anti-bonding" plasmon (ω_+) and a symmetric or "bonding" plasmon resonance (ω_-). (B) Energy diagram illustrating the dependence of nanoshell plasmon energies on the strength of the interaction between the sphere and the cavity plasmons, determined by the thickness of the metallic shell.

For example, this picture provides a simple and intuitive explanation for why the energy of the optically active plasmon resonance shifts to lower energies with decreasing shell thickness: the decreased shell thickness leads to a stronger coupling between the sphere and cavity plasmons, increasing the

splitting between the bonding and anti-bonding hybridized plasmons. This result is in quantitative agreement with Mie scattering theory which offers no such physical picture for this effect [82] [83]. In the case of metallic gold coating a dielectric core, such as silica, nanoshells resonate at specific wavelength of light ranging from 500 nm to 2 μ m, depending on their core/shell thickness ratio. Indeed, gold shell of 10 encasing a 110 nm silica core resonate in the NIR spectrum (\pm 800 nm); these wavelengths exhibit minimal optical absorption by, and consequently optimum penetration through, overlying tissues, with minimal attendant thermal injury. In the context of specifically absorbing energy in the NIR spectrum, these nanoshells are extremely efficient converting optical energy into heat [84].

1.2 Different therapies

1.2.1 Drug delivery

Many of the pharmacological properties of conventional (“free”) drugs can be improved through the use of drug delivery systems, which include particulate carriers and their associated therapeutics. Drug delivery systems are designed to alter the pharmacokinetics and biodistribution of their associated drugs or to function as drug reservoirs (i.e., as sustained release systems), or both. Figure 1.7 gives example of problems exhibited by free drugs that can be ameliorated by drug delivery systems [85] .

Problem	Implication	Effect of DDS
Poor solubility	A convenient pharmaceutical format is difficult to achieve, as hydrophobic drugs may precipitate in aqueous media. Toxicities are associated with the use of excipients such as Cremphor (the solubilizer for paclitaxel in Taxol).	DDS such as lipid micelles or liposomes provide both hydrophilic and hydrophobic environments, enhancing drug solubility.
Tissue damage on extravasation	Inadvertent extravasation of cytotoxic drugs leads to tissue damage, e.g., tissue necrosis with free doxorubicin.	Regulated drug release from the DDS can reduce or eliminate tissue damage on accidental extravasation.
Rapid breakdown of the drug in vivo	Loss of activity of the drug follows administration, e.g., loss of activity of camptothecins at physiological pH.	DDS protects the drug from premature degradation and functions as a sustained release system. Lower doses of drug are required.
Unfavorable pharmacokinetics	Drug is cleared too rapidly, by the kidney, for example, requiring high doses or continuous infusion.	DDS can substantially alter the PK of the drug and reduce clearance. Rapid renal clearance of small molecules is avoided.
Poor biodistribution	Drugs that have widespread distribution in the body can affect normal tissues, resulting in dose-limiting side effects, such as the cardiac toxicity of doxorubicin.	The particulate nature of DDS lowers the volume of distribution and helps to reduce side effects in sensitive, nontarget tissues.
Lack of selectivity for target tissues	Distribution of the drug to normal tissues leads to side effects that restrict the amount of drug that can be administered. Low concentrations of drugs in target tissues will result in suboptimal therapeutic effects.	DDS can increase drug concentrations in diseased tissues such as tumors by the EPR effect. Ligand-mediated targeting of the DDS can further improve drug specificity.

Figure 1.7: Non-ideal properties of drugs and their therapeutic implications

One solution, to improve drug efficiency, is to covalently link it to a polymer such as poly (ethylene glycol) (PEG). This strategy is used to increase the lifetime of proteins such as interferons, in this way they can stay in the bloodstream up to one week [86][87]. Another method consists in chemically linking the drug and a polymer soluble in water, non-immunogenic and biocompatible that can be degraded and eliminated by the body. When the system reaches the target (for example the ill cell), the specific links are destroyed and the drug is released. The drug biodistribution is modified by the dimension of the vector. The administration of antitumoral drugs is based on this principle: having a low molecular weight, these drugs can easily and quickly cross cellular membranes when administrated intravenously.

Colloidal systems tend to be quickly eliminated from the bloodstream and to accumulate in the reticuloendothelial system (RES) (liver, spleen, lungs and bone marrow). This phenomenon is called passive targeting. In other words, these systems accumulate in the liver because they are captured by the Kupffer cells while endothelial cells as well as parenchyma cells demonstrate a reduced uptake. The organs of the RES are responsible for this elimination; as a matter of fact their cells show a phagocytic activity and present, on their surface, specific receptors for plasmatic proteins which are able to fix themselves on the surface of colloidal systems in the bloodstream. This process is called opsonization and the proteins, opsonins. After interacting with macrophages receptors, the vectors are internalized via endocytosis and end up in lysosomes in which they will be degraded by lysosomal enzymes [88]. The preferential uptake of the vectors by the liver and the spleen can be used as passive targeting either for curing tumors located in these specific organs or intracellular infections regarding macrophages. In this case the vectors are called first generation vectors. One characteristic of these vectors is their specific accumulation in the liver; however this can represent an obstacle for reaching the target site. Therefore, the aim of the second generation vectors is to remain longer in the vascular system (without accumulating in the liver as the first generation vector). Analyzing the vectors uptake it has been demonstrated that the captation process depends substantially on the

nanoparticles superficial properties and diameter [89]. Liposomes and nanoparticles with a diameter lower than 80 nm are captured by the liver, when the diameter is higher than 400 nm the vectors are captured by the spleen and, finally when the diameter is in between the vectors are captured by the liver and the spleen in an increasing proportion depending on their diameter [90]. The captation by the RES organs is highly modified by the vectors surface properties for example it increases with the hydrophobic behavior of the vectors. Therefore, to avoid this issue, surfaces are often modified by coating with macromolecules and hydrophilic polymers. In this way it is possible to create a hydrophilic layer on the surface which inhibit the adsorption of the opsonins by hydrophobic interaction and steric repulsion [91] [92][93].

There are a variety of nanoparticles systems currently being explored for cancer therapeutics [94]. The material properties of each nanoparticle system have been developed to enhance delivery to the tumor. For example, hydrophilic surfaces can be used to provide the nanoparticles with stealth properties for longer circulation times and positively charged surfaces can enhance endocytosis. The types of nanoparticles currently used in research for cancer therapeutic applications include dendrimers [95], liposomes [96], polymeric nanoparticles [97], micelles [98], protein nanoparticles [99], ceramic nanoparticles [100], viral nanoparticles [101], metallic nanoparticles [102], and carbon nanotubes [103]. Some of these systems are reported in Figure 1.8.

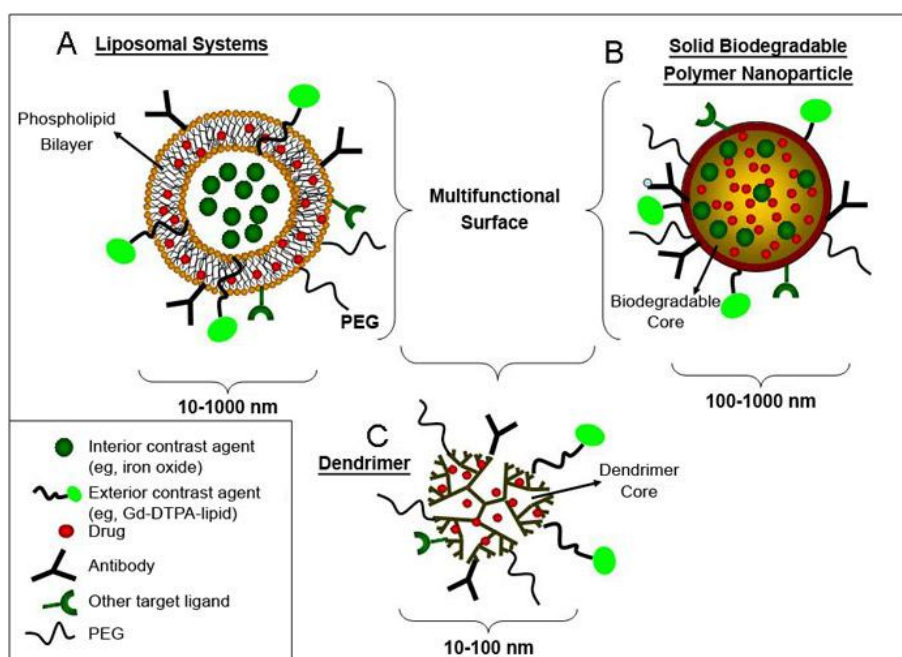


Figure 1.8: Examples of nanoparticulate systems for drug delivery

Functionalization of nanoparticles to create a stealth surface from opsonization, the adherence of serum proteins to the nanoparticle surface, is necessary to increase circulation times through avoidance of removal by the reticuloendothelial systems (RES) [104][105]. Short circulation times decrease the efficiency of the delivery of the nanoparticles to the tumor site. Incorporation of a hydrophilic polymer, such as poly(ethylene glycol) (PEG), to the surface of the nanoparticles allows for a reduction in opsonization, which reduces removal by the RES [106][107].

Despite extensive research on nanoparticles systems for cancer therapeutics, there are only a few nanoparticles drug delivery systems approved by the U.S. Federal Drug Administration and European Medicines Agency to treat cancer. Specifically, the systems that have been approved include liposomal doxorubicin (MyocetTM, Elan Pharmaceuticals), PEGylated liposomal doxorubicin (Doxil[®], Ortho Biotech, and Caelyx[®], Schering Plough), PEGylated liposomal daunorubicin (DaunoXome[®], Diatos), and the recently approved albumin-bound paclitaxel-loaded nanoparticles (Abraxane[®], Abraxis Bioscience) [94].

1.2.2 Hyperthermia

Magnetic fluid hyperthermia (MFH), i.e. the heating of tissue [108] using magnetic nanoparticles (MNPs), is a promising tool in the therapy of various cancers because tumor cells are more sensitive to temperatures in the range of 42-45°C than normal tissues cells [109]. As a matter of fact, there are several benefits to using hyperthermia, this process not only enhances the effectiveness of other cancer treatments, but it also kills tumor cells that are resistant to other forms of cancer treatment.

Several methods of hyperthermia are employed in cancer therapy: whole body hyperthermia, radiofrequency hyperthermia, inductive hyperthermia using a microwave antenna, implantable needles, and nanosized magnetic nanoparticles [110].

At least four different mechanisms exist by which magnetic materials can generate heat in an alternating field [111]:

- Generation of eddy currents in magnetic particles with size $> 1 \mu\text{m}$,
- Hysteresis losses in magnetic particles $> 1 \mu\text{m}$ and multidomain magnetic particles,
- Relaxation losses in superparamagnetic single-domain magnetic particles,
- Frictional losses in viscous suspension.

Relaxation losses in single-domain magnetic nanoparticles fall into two modes: rotational (Brownian) mode and Néel mode.

Majority of hyperthermia treatments don't achieve uniform heating of tumor region to the desired temperature without damaging normal tissue. Therefore, researchers have proposed intracellular hyperthermia by using nanosized magnetic particles [110]. MFH allows the heating to be restricted to the tumor area [112]. This method, which incorporates injecting the magnetic fluids directly into the tumor body, relies on the theory that any metallic objects when placed in an alternating magnetic field will have induced currents flowing within them [113]. As this occurs, the magnetic nanoparticles produce heat, as a product of resisting the current flow. With the application of an external

alternated magnetic field [114], the particles in turn heat the malignant cells when they come into contact, thus increasing the cells sensitivity to other treatments such as chemotherapy or radiation.

It was discovered that magnetic nanoparticles concentrated by an external constant magnetic field in tumor vasculature may lead to embolic lesions and necrosis of a tumor body and further the heat produced for thermal activation of a drug enhances the effect of chemotherapy by local hyperthermic treatment of neoplastic cells [115].

Using magnetite particles, Ohno et al strategy was based on the heat radiation associated with the physical process of hysteresis loss of magnetic substance in the alternative magnetic field [116]. Instead, though, they made a thin stick-type mingled with carboxymethylcellulose to obtain a higher heating effect [116]. The benefit of this product was that one could much more easily direct the magnetic nanoparticles to their desired location. What was found was that, by using carboxymethylcellulose, the particles did not invade the surrounding normal tissue. In addition, the tumor sized decreased, thus obtaining satisfactory results.

The response of the tumor to hyperthermia depends on the size of the tumor, its composition, physical location within the host tissue, and its vascularization [117]. During hyperthermia, the tumor bed does not vasodilate therefore, blood flow can't increase and heat is retained in the tumor tissue at temperatures that would have caused normal capillary beds to vasodilate [117]. The growth of solid tumors is associated with the incorporation of fluid within the tumor mass as a result of nutrient deprivation, which can constitute up to 60% of the tumor volume. This fluid however, is void of oxygen and glucose, and may contain excessive amounts of carbon dioxide and lactic acid. Under conditions of extreme nutrient deprivation, cell death occurs rapidly at 37°C and even quicker at higher temperatures. An increase in the temperature of this fluid may lead to an increase in the hydrostatic pressure due to the increase in molecular motion [117].

Cell death occurs in two modes, apoptosis and necrosis, which are biochemically and morphologically different [118]. Apoptosis is a genetically

programmed and biochemically active mode of death in which the cell actively participates in its own elimination. It is required for cell life span and normal development [119]. Apoptosis aids in self-deletion of injured cells, terminal differentiation of epithelial cells, and organ and tissue shaping [118]. Abnormalities of this process are implicated on several human diseases, including cancer. This process can be recognized by cell shrinking, condensation of the chromatin, and eventually DNA fragmentation. In addition, actin is considered to play a role in several main morphological events of apoptosis, including formation of blebs, cell rounding, detachment, and final cell disintegration into apoptotic bodies [119]. Cells inducing apoptosis retain much of their membrane function and do not elicit an inflammatory response. This process can be triggered by radiation, transduced signals, DNA damage, and hyperthermia. Furthermore, hyperthermia with a temperature range of 41-45 °C induces apoptosis to varying degrees in many cell lines. The mechanism behind hyperthermia-induced apoptosis, however, isn't well understood. Some postulate that the primary targets are heat liable and newly synthesized proteins. These denatured proteins and unfolded nascent peptides can be cytotoxic and lead to cell death as illustrated in Figure 1.9 [118].

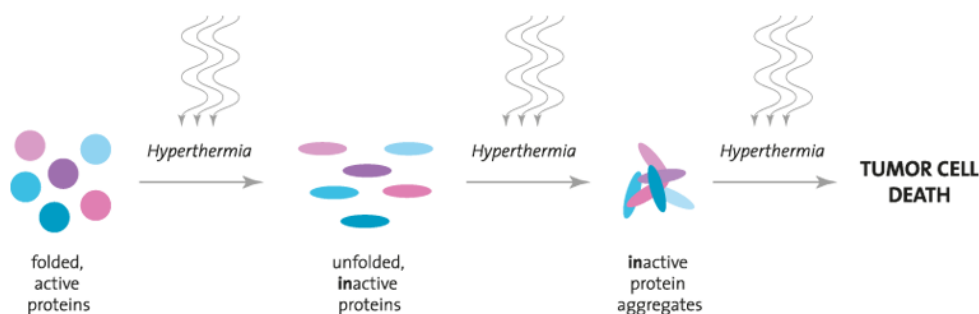


Figure 1.9: Illustration of the protein denaturation process by hyperthermia

In addition, heat shock proteins act by preventing the aggregation of the denatured proteins through interactions with the ATP pathway. Targeted proteins must go through the ATP pathway before they can be recognized as substrate for proteolysis. Therefore when hyperthermia is induced on the cells, the proteins denature before the heat shock protein response can occur. It is logical to assume then, that by administering hyperthermia, the cell can

accumulate high dose of heat shock proteins. Some hypothesize that by inhibiting the synthesis of the heat shock proteins the cell is unable to build a pool of protective stress proteins and the cell loses its capability to survive [118].

Necrosis concerns cells subject to toxic attack [120]. In this case, metabolic functions stop, which therefore causes a lack of osmotic regulation, thereby inflicting cellular swelling. In addition, necrosis causes a sharp decline in ATP production, mitochondrial swelling, and eventually cytolysis and the release of pro-inflammatory agents as illustrated in Figure 1.10 [118].

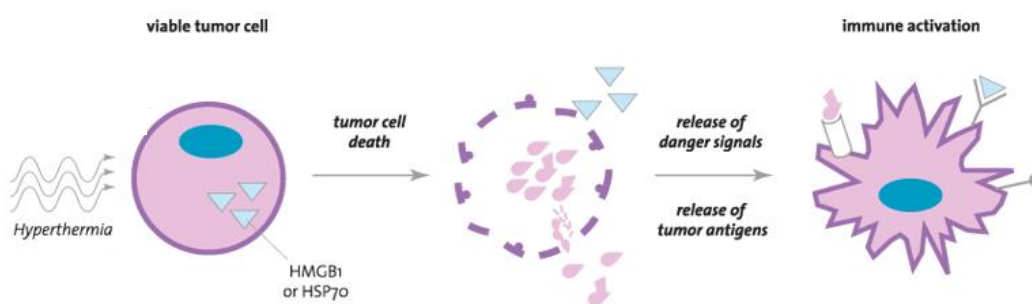


Figure 1.10: illustration of the necrosis phenomenon caused by hyperthermia

Unlike apoptosis, these reactions occur as a natural result of loss of cell function. Although it has been widely accepted that hyperthermia always caused necrosis, it is now clear that it isn't the case [121]. Rather, hyperthermia induces apoptosis in neoplastic cells and tissues[122].

1.2.3 Photothermal therapy

Over the past decade, it has become increasingly apparent that by precisely controlling the dimensions of metallic nanostructures of certain specific shapes, one can control the wavelength at which they interact with the incident light in a highly precise manner [123][124][125][126][127]. The optical resonance frequency of metal is function of not only the type of metal, but also, especially on the nanometer scale, of the shape of the particle. For solid metallic nanospheres, the optical resonance is essentially an almost fixed frequency resonance. Solid Au nanoparticles which are ~ 30 nm in diameter are well known to absorb green light at ~ 520 nm, and give rise to a deep red color

when dispersed in colloidal solutions. Michael Faraday was the first person to observe this spectacular phenomenon around 1850. Actually, the optical resonant frequency of solid metallic nanoparticles varies only weakly with particle size, slightly shifting to longer wavelengths as the particles become larger. One nanoparticle geometry that gives rise to much broader optical tunability is that of metallic nanorods [128]. As the aspect ratio of the nanorods is tuned, the wavelength at which optical resonance of the structure occurs can be systematically tuned over a broad spectral range from visible to near infrared regions. Such optical tunability of metallic nanorods is evident based on the dramatic color change of the colloidal nanorods solutions as the aspect ratio varies.

The fascinating optical resonant behaviors of metal nanoparticles are essentially determined by the collective oscillations of free electrons in the metals with respect to the positive ion background, known as plasmons. The plasmon resonances can be optically excited when a photon is absorbed at a metal-dielectric interface and transfers energy into the collective electron oscillations, which are coupled in-phase with the incident light at a certain resonant frequency. In nanoparticles systems, the plasmon resonance frequencies are dependent on the size and shape of the metallic nanoparticles as the oscillations of free electrons are confined by the particle boundaries [125].

Another type of surface plasmons is called localized surface plasmons (LSPs), which corresponds to collective excitations of free electrons confined to a finite volume. Under the irradiation of incident light, the free electrons in a metallic nanostructure are driven by the electric field to collectively oscillate at a resonant frequency relative to the lattice of positive ions [129]. At this resonant frequency, the incident light is absorbed by the nanostructure. Some of these photons will be released with the same frequency in all directions and this process is known as scattering. Meanwhile, some of these photons will be converted into phonons or vibrations of the lattice and this process is referred to as absorption [130].

For spherical Au and Ag particles of relatively small size (with dimensions much smaller than the wavelength of incident light, with diameters in the range

of 5-50 nm), only dipole plasmon resonance is involved. The colloidal suspensions of these small Au and Ag nanoparticles display a strong LSP peak around 520 nm and 400 nm, respectively. Strong optical scattering absorption of light by solid Au and Ag nanoparticles in visible spectral region due to localized surface plasmon resonance (LSPR) are a classical effect in which the light's electromagnetic field drives the collective oscillations of the free electrons into resonance. This effect was theoretically described by Mie in 1908 by solving Maxwell's equations for a metal sphere surrounded by a dielectric medium using the dielectric function of the bulk metal [131].

It is very important to create highly tunable LSPRs of nanoparticles over a broader spectral region. Indeed, expanding the plasmonic tunability of metallic nanoparticles from the visible into the near infrared regions opens a whole set of new opportunities for spectroscopic sensing and biomedical applications. For example, metallic nanoparticles with plasmon resonances in the near infrared can be used for high-contrast bioimaging and photothermal cancer therapy [132][133]. It has been discovered that by changing nanospheres into either nanorods or nanoshells, one can tune the plasmon resonances of the nanoparticles from the visible region to the near infrared "water window" where tissues and blood are transparent. These near infrared resonant nanoparticles can be properly functionalized with antibodies to target specific types of tumors. Because tissue is relatively transparent in the near infrared, the nanoparticles can be illuminated from outside the body to locally heat and thus, selectively destroy the tumors *in vivo*.

As a matter of fact, local application of heat is a well-known concept in therapeutic medicine [134]; as such photothermal therapy based on metal nanomaterials has been actively explored for treating cancer with encouraging success [135]. Photothermal therapy relies on heat generated from light for destroying cancer cells, and it affords potential advantages of active targeting at specific cancer sites, low toxicity, minimal side effects and high efficacy [136]. In order to realize the full therapeutic potential of photothermal therapy it is essential to optimize its photothermal conversion efficiency, decreasing the energy dose of laser light and minimizing potential damage to surrounding

normal tissue; that is why ideal material for photothermal therapy should have strong and tunable SPR, especially in the Near Infra Red (NIR: 700 - 900 nm) thereby providing an opportunity for therapeutic effects in deep tissues while limiting the heat generated to the region of the target tissue. The process is illustrated Figure 1.11.

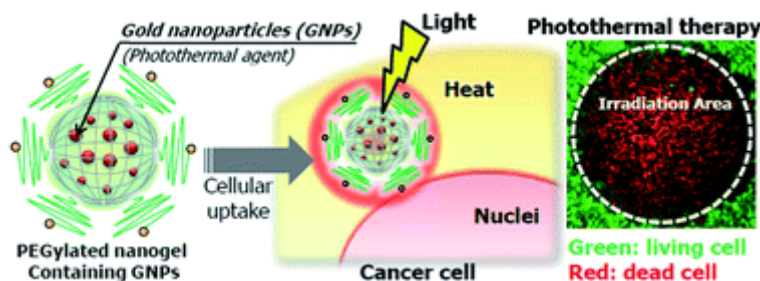


Figure 1.11: Illustration of the photothermal therapy process

In general, photothermal ablation (PTA) can operate in three basic modes, (i) light without sensitizers, (ii) light with molecular sensitizer for photothermal conversion [136], and (iii) light with metal nanostructure for photothermal conversion. Because of the high photothermal conversion efficiency of metal, the third approach is the most effective in terms of heat generation. However, PTA based on metal nanostructures does involve issues such as delivery to target cancer sites and potential toxicity and side effects. Using strategies such as antibody-antigen or ligand-receptor interaction, one can actively target and deliver the metal nanostructure to specific cancer tissues [137][138]. Metals such as gold and silver are considered as biocompatible and low in toxicity and thus exhibit good potential for PTA applications.

For example, laser-induced local heating of cellular structures through PTA using either pulsed or continuous laser radiation and mediated by light-absorbing nanoparticles and microparticles provides precisely localized damage limited to even single cells [139][140][141][142][143]. Accumulation of light-absorbing nanoparticles in relatively transparent cells can enhance their optical absorption up to several orders of magnitude. Thus, metal nanoparticles act as localized sources for photothermal generation to result in cell damage.

The mechanism for heat-induced cell death in PTA is not yet well understood. Possible explanations include heat shock of proteins, inactivation of membrane

proteins and mitochondria, depolymerization of cytoskeleton filaments, membrane blebbing, and plasma membrane disruption due to a cavitation effect [144][145][146][147][148]. The cavitation effect was also suggested to be responsible of bubble formation [149][150][151]. One interesting related question is the local temperature on the metal nanostructure surface that is likely much higher than the average temperature of the surroundings. Molecules with temperature-dependent luminescence or Raman scattering based on the ratio of Stokes and anti-Stokes scattering may provide some possible means for determining the local temperature. The distance between the metal nanostructure and the cancer cell is expected to be an important parameter for PTA. Likewise, the location of the nanostructure in the cancer cell will also be crucial, for example, on the surface, in the membrane, or near the cell nuclei.

References

- [1] T. Schroder, A. Quintilla, J. Setzier, E. Birtaian, W. Wenzel, S. Brase, *WSEAS Trans. Biol. Biomed.*, **2007**, 4, 10.
- [2] B. Panchapakesan, *Oncology*, **2005**, 20.
- [3] P. Ruchitbhai, S. Krutika, *Nanotechnology*, **2009**.
- [4] H. Pinto-Alphandary, A. Andreumont, P. Couvreur, *Int. J. Antimicrob. Agents*, **2000**, 13,155–168 .
- [5] A. Gabizon, *Cancer Res.*, **1992**, 52, 891–896.
- [6] C. Verdun, F. Brasseur, H. Vranckx, P. Couvreur, M. Roland, *Cancer Chemother. Pharmacol.*, **1990**, 26, 13–18.
- [7] T. Daemen, J. Regts, M. Meesters, M.T. Ten Kate, I. A. J. M. Bakker-Woudenberg, G. Scherphof, *J. Control. Release*, **1997**, 44, 1–9 .
- [8] R. Fernandez-Urrusuno, E. Fattal, J.M.Jr Rodrigues, J. Féger, P. Bedossa, P. Couvreur, *J. Biomed. Mater. Res.*, **1996**, 31, 401–408.
- [9] F. Fawaz, F. Bonini, M. Guyot, A.M. Lagueny, H. Fessi, J.P. Devissaguet, *Pharm. Res.*, **1993**, 10, 750–766.
- [10] S. Gibaud, J.P. Andreux, C. Weingarten, M. Renard, P. Couvreur, *Eur. J. Cancer*, **1994**, 30A, 820–826.

- [11] S. Gibaud, C. Rousseau, C. Weingarten, R. Favier, L. Douay, J.P. Andreux, *J. Control. Release*, **1998**, 52, 131–139.
- [12] N. Chiannikulchai, Z. Driouich, J.P. Benoit, A.L. Parodi, P. Couvreur, *Select. Cancer Ther.*, **1989**, 5, 1–11.
- [13] N. Chiannikulchai, N. Ammoury, B. Caillou, J.P. Devissaguet, P. Couvreur, *Cancer Chemother. Pharmacol.*, **1990**, 26, 122–126.
- [14] R. Massart, *IEEE Trans. Magn.*, **1981**, 17, 1247–1248.
- [15] N. Fauconnier, A. Bée, J. Roger, *J. Mol. Liq.*, **1999**, 83, 233–42.
- [16] J.P. Muller, J. Gähde, H. Mehner, *Surf. Coat. Tech.*, **1999**, 116, 367–369.
- [17] P. Lottichi, C. Barato, D. Bersani, *Opt. Mater.*, **1998**, 9, 368–372.
- [18] I. Chourpa, L. Douziech-Eyrolles, L. Ngaboni-Okassa, *Analyst*, **2005**, 130, 1395–1403.
- [19] C. Alexiou, R. Jurgons, R. Schmid, *J. Magn. Magn. Mater.*, **2005**, 293, 389–393.
- [20] D. Bazile, C. Prud'homme, M.T. Bassoullet, *J. Pharm. Sci.*, **1995**, 84, 493–498.
- [21] G. Storm, S.O. Belliot, T. Daemen, *Adv. Drug. Deliver. Rev.*, **1995**, 17, 31–48.
- [22] Z. Xu, Q. Liu, J.A. Finch, *Surf. Sci. Series.*, **1999**, 78, 31–50.
- [23] A.K. Gupta, M. Gupta, *Biomaterials*, **2005**, 26, 3995–4021.
- [24] S.I. Jeon, J.D. Andrade, *J. Colloid. Interf. Sci.*, **1991**, 142, 159–166.
- [25] G. Storm, S.O. Belliot, T. Daemen, *Adv. Drug. Deliver. Rev.*, **1995**, 17, 31–48.
- [26] Y. Zhang, N. Kohler, M. Zhang, **2002**, *Biomaterials*, 23, 1553–1561.
- [27] M.D. Butterworth, L. Illum, S.S. Davis, *Colloid Surface A*, **2001**, 179, 93–102.
- [28] N. Kohler, G.E. Fryxell, M. Zhang, *J. Am. Chem. Soc.*, **2004**, 126, 7206–11.
- [29] A.K. Gupta, A.S.G. Curtis, *J. Mater. Sci: materials in medicine*, **2004**, 15, 493–6.

- [30] H.Y. Acar, R.S. Garaas, F. Syud, *J. Magn. Magn. Mater.*, **2005**, 293,1–7.
- [31] R.S. Molday, D. Mackenzie, *J. Immunol. Methods*, **1982**, 52, 353–67.
- [32] H. Pardoe, W. Chua-anusorn, T.G. St Pierre, *J. Magn. Magn. Mater.*, **2001**, 225, 41–6.
- [33] M.C. Bautista, O. Bomati-Miguel, M. del Puerto Morales, *J. Magn. Magn. Mater.*, **2005**, 293, 20–7.
- [34] X.Q. Xu, H. Shen, J.R. Xu, *Appl. Surf. Sci.*, **2005**, 252, 494–500.
- [35] L.M. Lacava, V.A.P. Garcia, S. Kückelhaus, *J. Magn. Magn. Mater.*, **2004**, 272, 2434–2435.
- [36] G. Nedelcu, *Dig. J. Nanomat. Biostruct.*, **2008**, 3, 103-107.
- [37] T. Neuberger, B. Schöpf, H. Hofmann, M. Hofmann, B. Von Rechenberg, *J. Magn. Magn. Mater.*, **2005**, 293, 483-496.
- [38] G. Frens, *Nat Phys Sci*. **1973**, 241, 20–2.
- [39] J. Turkevich, P. C. Stevenson, J. Hillier, *Disc Farad Soc.* **1951**, 11, 55–75.
- [40] J. Turkevich, G. Garton, P. C. Stevenson, *J Colloid Sci.* **1954**, 9, 26–35.
- [41] M. C. Daniel, D. Astruc, *Chem. Rev.* **2004**, 104, 293–346.
- [42] V. Biju, T. Itoh, A. Anas, A. Sujith, M. Ishikawa, *Anal. Bioanal. Chem.* **2008**, 391, 2469–2495.
- [43] C. M. Niemeyer, *Angew. Chem. Int. Ed.*, **2001**, 40, 4128–4158.
- [44] M. Hu, J. Y. Chen, Z. Y. Li, L. Au, G. V. Hartland, X. D. Li, M. Marquez, Y. N. Xia, *Chem. Soc. Rev.* **2006**, 35, 1084–1094.
- [45] C. J. Murphy, T. K. San, A. M. Gole, C. J. Orendorff, J. X. Gao, L. Gou, S. E. Hunyadi, T. Li, *J. Phys. Chem. B*, **2005**, 109, 13857–13870.
- [46] C. J. Murphy, T. K. Sau, A. Gole, C. J. Orendorff, *MRS Bull*, **2005**, 30, 349–355.
- [47] J. Chen, F. Saeki, B. J. Wiley, H. Cang, M. J. Cobb, Z. Y. Li, L. Au, H. Zhang, M. B. Kimmey, X. D. Li, Y. Xia, *Nano Lett*, **2005**, 5, 473–477.
- [48] C. Wang, Y. Hu, C. M. Lieber, S. Sun, *J. Am. Chem. Soc.*, **2008**, 130,

- 8902–8903.
- [49] S. Link, M. A. El-Sayed, *J. Phys. Chem. B*, **1999**, 103, 4212–4217.
- [50] C. J. Murphy, T. K. Sau, A. M. Gole, C. J. Orendorff, J. Gao, L. Gou, S. E. Hunyadi, T. Li, *J. Phys. Chem. B*, **2005**, 109, 13857–13870.
- [51] Y. Xia, N. J. Halas, *MRS Bull.*, **2005**, 30, 338–343.
- [52] Y. Y. Yu, S. S. Chang, C. L. Lee, C. R. C. Wang, *J. Phys. Chem. B*, **1997**, 34, 6661–6664.
- [53] B. Nikoobakht, M. A. El-Sayed, *Chem. Mater.*, **2003**, 10, 1957–1962.
- [54] C. J. Murphy, T. K. Sau, A. M. Gole, C. J. Orendorff, J. Gao, L. Gou, *J. Phys. Chem. B*, **2005**, 29, 13857–13870.
- [55] S. J. Oldenburg, R. D. Averitt, S. L. Westcott, N. J. Halas, *Chem. Phys. Lett.*, **1998**, 2–4, 243–247.
- [56] Y. Sun, B. T. Mayers, Y. Xia, *Nano Lett.*, **2002**, 5, 481–485.
- [57] L. R. Hirsch, R. J. Stafford, J. A. Bankson, S. R. Sershen, B. Rivera, R. E. Price, *Proc. Natl. Acad. Sci. USA*, **2003**, 23, 13549–13554.
- [58] X. Huang, I. H. El-Sayed, W. Qian, M. A. El-Sayed, *J. Am. Chem. Soc.*, **2006**, 6, 2115–2120.
- [59] J. Chen, D. Wang, J. Xi, L. Au, A. Siekkinen, A. Warsen, *Nano Lett.*, **2007**, 5, 1318–1322.
- [60] K. Sokolov, M. Follen, J. Aaron, I. Pavlova, A. Malpica, R. Lotan, *Cancer Res.*, **2003**, 9, 1999–2004.
- [61] K. Sokolov, J. Aaron, B. Hsu, D. Nida, A. Gillenwater, M. Follen, *Technol. Cancer Res. Treat.*, **2003**, 6, 491–504.
- [62] K. S. Lee, M. A. El-Sayed, *J. Phys. Chem. B*, **2005**, 43, 20331–20338.
- [63] X. Huang, M. A. El-Sayed. *Journal of Advanced Research*, **2010**, 1, 13-28.
- [64] R. Gans, *Ann. Phys.*, **1915**, 47, 270–284.
- [65] B. Nikoobakht, M. A. El-Sayed, *Chem. Mater.*, **2003**, 10, 1957–1962.
- [66] C. J. Murphy, T. K. Sau, A. M. Gole, C.J. Orendorff, J. Gao, L. Gou, *J. Phys. Chem. B109*, **2005**, 29, 13857–13870.
- [67] M. Liu, P. Guyot-Sionnest, *J. Phys. Chem. B* 109, **2005**, 47, 22192–22200.

- [68] Y. Sun, B. T. Mayers, Y. Xia, *Nano Lett.*, **2002**, 5, 481–485.
- [69] J. Chen, F. Saeki, B. J. Wiley, H. Cang, M. J. Cobb, Z. Y. Li, *Nano Lett.*, **2005**, 3, 473–477.
- [70] J. Chen, B. Wiley, Z. Y. Li, D. Campbell, F. Saeki, H. Cang, *Adv. Mater.*, **2005**, 18, 2255–2261.
- [71] C. Loo, A. Lin, L. Hirsch, M. H. Lee, J. Barton, N. Halas, *Technol. Cancer Res. Treat.*, **2004**, 1, 33–40.
- [72] S. E. Skrabalak, J. Chen, Y. Sun, X. Lu, L. Au, C. M. Cobley, *Acc. Chem. Res.*, **2008**, 12, 1587–1595.
- [73] A. M. Schwartzberg, T. Y. Olson, C. E. Talley, J. Z. Zhang, *J. Phys. Chem. B*, **2006**, 110, 19935–19944.
- [74] H. P. Liang, L. J. Wan, C. L. Bai, L. Jiang, *J. Phys. Chem. B*, **2005**, 109, 7795–7800.
- [75] J.Z. Zhang, *J. Phys. Chem. Lett.*, **2010**, 1, 686.
- [76] B.D. Chithrani, A.A. Ghazani, W.C.W. Chan, *Nano Lett.*, **2006**, 6, 662–668.
- [77] M.P. Melancon, W. Lu, Z. Yang, R. Zhang, Z. Cheng, A. M. Elliot, J. Stafford, T. Olson, J. Z. Zhang, C. Li, *Mol. Cancer Ther.*, **2008**, 7, 1730–1739.
- [78] W. Lu, C. Y. Xiong, G. D. Zhang, Q. Huang, R. Zhang, J. Z. Zhang, C. Li, *Clin. Cancer Res.*, **2009**, 15, 876–886.
- [79] S. J. Oldenburg, R. D. Averitt, S. L. Westcott, N. J. Halas, *Chem. Phys. Lett.*, **1998**, 2–4, 243–247.
- [80] A.L. Aden, M. Kerker, *J. Appl. Phys.*, **1951**, 22, 1242–1246.
- [81] A.E. Neeves, M.H., *J. Opt. Soc. Am.*, **1989**, 6, 787.
- [82] H. Wang, *Tunable Plasmonic Nanostructures: from Fundamental Nanoscale Optics to Surface-enhanced Spectroscopies (thesis)*, **2007**.
- [83] X. Zhou, H. Li, S. Xie, S. Fu, H. Xu, Z. Liu, *Solid State Commun.*, **2011**, 151, 1049.
- [84] P. Fortina, L.J. Kricka, D.J. Graves, J. Park, T. Hyslop, F. Tam, N. Halas, S. Surrey, S.A Waldman, *TRENDS in Biotechnol.*, **2007**, 25, 145.
- [85] T.M. Allen, P.R. Cullis, *Science*, **2004**, 303, 1818–1822.

- [86] B. Chertok, A.E. David, B.A. Moffat, V.C. Yang, *Biomaterials*, **2009**, 30, 6780–6787.
- [87] M.M. Yallapu, S.P. Foy, T.K. Jain, V. Labhassetwar, *Pharm. Res.*, **2010**, 27, 2283–2295.
- [88] B. Chertok, A.E. David, V.C. Yang, *Biomaterials*, **2010**, 31, 6317–6324.
- [89] J.W. Yoo, E. Chambers, S. Mitragotri, *Curr. Pharm. Des.*, **2010**, 16, 2298–2307.
- [90] A.K. Gupta, S. Wells, *IEEE Trans. NanoBiosci.*, **2004**, 3, 66–73.
- [91] H. Lee, M.K. Yu, S. Park, S. Moon, J.J. Min, Y.Y. Jeong, H.W. Kang S. Jon, *J. Am. Chem. Soc.*, **2007**, 129, 12739–12745.
- [92] C. Sun, K. Du, C. Fang, N. Bhattarai, O. Veiseh, F. Kievit, Z. Stephen, D. Lee, R.G. Ellenbogen, B. Ratner, M. Zhang, *ACSNano*, **2009**, 4, 2402–2410.
- [93] M. Kumagai, T.K. Sarma, H. Cabral, S. Kaida, M. Sekino, N. Herlambang, K. Osaka, M.R. Kano, N. Nishiyama, K. Kataoka, *Macromol. Rapid. Commun.*, **2010**, 31, 1521–1528.
- [94] B. Haley, E. Frenkel, *Urol. Oncol.*, **2008**, 26, 57–64.
- [95] J.F. Kukowska-Latallo, K.A. Candido, Z. Cao, S.S. Nigavekar, I.J. Majoros, T.P. Thomas, L.P. Balogh, M.K. Khan, J.R. Baker Jr., *Cancer Res.*, **2005**, 65, 5317–5324.
- [96] N.C. Bellocq, S.H. Pun, G.S. Jensen, M.E. Davis, *Bioconjug. Chem.*, **2003**, 14, 1122–1132.
- [97] T. Betancourt, B. Brown, L. Brannon-Peppas, *Nanomed.*, **2007**, 2, 219–232.
- [98] D. Sutton, N. Nasongkla, E. Blanco, J. Gao, *Pharm. Res.*, **2007**, 24, 1029–1046.
- [99] F.M. Veronese, G. Pasut, *Drug Discov. Today*, **2005**, 10, 1451–1458.
- [100] X. Montet, K. Montet-Abou, F. Reynolds, R. Weissleder, L. Josephson, *Neoplasia*, **2006**, 8, 214–222.
- [101] M.L. Flenniken, L.O. Liepold, B.E. Crowley, D.A. Willits, M.J. Young, T. Douglas, *Chem. Commun.*, **2005**, 4, 447–449.

- [102] A.R. Lowery, A.M. Gobin, E.S. Day, N.J. Halas, J.L. West, *Int. J. Nanomed.*, **2006**, 1, 149–154.
- [103] N.W. Kam, M. O'Connell, J.A. Wisdom, H. Dai, *Proc. Natl. Acad. Sci. USA*, **2005**, 102, 11600–11605.
- [104] D. Bhadra, S. Bhadra, S. Jain, N.K. Jain, *Int. J. Pharm.*, **2003**, 257, 111–124.
- [105] F. Fawaz, F. Bonini, M. Guyot, A.M. Lagueny, H. Fessi, J.P. Devissaguet, *Pharm. Res.*, **1993**, 10, 750–756.
- [106] R. Gref, M. Luck, P. Quellec, M. Marchand, E. Dellacherie, S. Harnisch, T. Blunk, R.H. Muller, *Colloids Surf. B Biointerfaces*, **2000**, 18, 301–313.
- [107] H. Otsuka, Y. Nagasaki, K. Kataoka, *Adv. Drug Deliv. Rev.*, **2003**, 55, 403–419.
- [108] Y. Hori, R. Nagai, N. Urabe, T. Yoshikawa, M. Otsuka, *Bioorganic & Medicinal Chemistry*, **2002**, 10, 111.
- [109] M. Shinkai, B. Le, H. Honda, K. Yoshikawa, K. Shimizu, S. Saga, T. Wakabayashi, J. Yoshida, T. Kobayashi, *Japan Journal of Cancer Research*, **2001**, 92, 1138.
- [110] M. Yanase, M. Shinkai, H. Honda, T. Wakabayashi, J. Yoshida, T. Kobayashi, *Japan Journal of Cancer Research*, **1998**, 89, 775.
- [111] W. Andra, *Magnetism in Medicine*, Berlin: Wiley–VCH, **1998**.
- [112] P. Tartaj, M. Morales, S. Veintemillas-Verdaguer, T. González-Carreño, C. Serna, *J. Phys. D: App. Phys.*, **2003**, 36, 182.
- [113] C. Berry, A. Curtis, *J. Phys. D: App. Phys.*, **2003**, 36, 198.
- [114] I. Šafařík, M. Šafaříková, *Chemical Monthly*, **2002**, 133, 737.
- [115] M. Babincová, D. Leszczynska, P. Sourivong, P. Babinec, J. Leszczynski, *Medical Hypotheses*, **2004**, 62, 375.
- [116] T. Ohno, T. Wakabayashi, A. Takemura, J. Yoshida, A. Ito, M. Shinkai, H. Honda, T. Kobayashi, *Journal of Neuro-Oncology*, **2002**, 56, 233.
- [117] R. Vertrees, A. Leeth, M. Girouard, J. Roach, J. Zwischenberger, *Perfusion*, **2002**, 17, 279.

- [118] B. Poe, K. O'Neill, *Apoptosis*, **1997**, 2, 510.
- [119] F. Luchetti, F. Mannello, B. Canonico, M. Battistelli, S. Burattini, E. Falcieri, S. Papa, *Apoptosis*, **2004**, 9, 635.
- [120] L. Huschtscha, T. Jeitner, C. Andersson, W. Bartier, M. Tattersall, *Exp. Cell Res.*, **1994**, 212, 161.
- [121] Y. Rong, P. Mack, *International Journal of Hyperthermia*, **2000**, 16, 19.
- [122] Q. A. Pankhurst, J. Connolly, S.K. Jones, J. Dobson, *J. Phys. D. Appl. Phys.*, **2003**, 36, 167.
- [123] S. Link, M.A. El-Sayed, *Ann. Rev. Phys. Chem.*, **2003**, 54, 331-366.
- [124] S. Link, M.A. El-Sayed, *Inter. Rev. Phys. Chem.*, **2000**, 19, 409-453.
- [125] M.A. El-Sayed, *Acc. Chem. Res.*, **2001**, 34, 257-264.
- [126] C. Burda, X.B. Chen, R. Narayanan, M.A. El-Sayed, *Chem. Rev.*, **2005**, 105, 1025-1102.
- [127] Y. Xia, N. Halas, *MRS Bulletin*, **2005**, 30, 338-344.
- [128] S. Link, M.A. El-Sayed, *J. Phys. Chem. B*, **1999**, 103, 8410-8426.
- [129] U. Kreibig, M. Vollmer, *Optical Properties of Metal Clusters*, Springer-Verlag: Berlin, Germany, **1995**.
- [130] C. F. Bohren, D.R. Huffman, *Absorption and Scattering of Light by Small Particles*, John Wiley & Sons: New York, **1998**.
- [131] G. Mie, *Ann. Phys.*, **1908**, 25, 377-452.
- [132] L.R. Hirsh, R.J. Stafford, J.A. Bankson, S.R. Sershen, B. Rivera, R.E. Price, J.D. Hazle, N.J. Halas, J.L. West, *Proc. Natl. Acad. Sci. USA*, **2003**, 100, 13549-13554.
- [133] X.H. Huang, I.H. El-Sayed, W. Qian, M.A. El-Sayed, *J. Am. Chem. Soc.*, **2006**, 128, 2115-2120.
- [134] D. Pissuwan, S. M. Valenzuela, M.B. Cortie, *Biotechnology*, **2006**, 24, 62.
- [135] J.Z. Zhang, *J. Phys. Chem. Lett.*, **2010**, 1, 686.
- [136] J. Myhill, M. Borrelli, M. Kokoska, L. Buckmiller, W. Baumler, G. Shafirstein, *Lasers Surg. Med.*, **2008**, 335.
- [137] P. Chakravarty, R. Marches, N.S. Zimmerman, A.D.E. Swafford, P.

- Bajaj, I.H. Musselman, P. Pantano, R.K. Draper, E.S. Vitetta, *Proc. Natl. Acad. Sci. USA*, **2008**, 105, 8697–8702.
- [138] M.S. Arayne, N. Sultana, *Pak. J. Pharm. Sci.*, **2006**, 19, 258–268.
- [139] D.O. Lapotko, E. Lukianova, A.A. Oraevsky, *Lasers Surg. Med.*, **2006**, 38, 631–642.
- [140] M.C. Ambrogi, G. Fontanini, R. Cioni, P. Faviana, O. Fanucchi, A. Mussi, *J. Thorac. Cardiovasc. Surg.*, **2006**, 131, 1002–1006.
- [141] J.M. Stern, J. Stanfield, W. Kabbani, J.T. Hsieh, J.R.A. Cadeddu, *J. Urol.*, **2008**, 179, 748–753.
- [142] T.L. Boaz, J.S. Lewin, Y.C. Chung, J.L. Duerk, M.E. Clampitt, J.R. Haaga, *J. Magn. Reson. Imaging*, **1998**, 8, 64–69.
- [143] C.T. Nguyen, S.C. Campbell, *Expert Rev. Anticancer Ther.*, **2008**, 8, 1899–1905.
- [144] K. Bowler, H. Laudien, I. Laudien, *J. Therm. Biol.*, **1983**, 8, 426–430.
- [145] H. Bass, W.T. Coakley, J.L. Moore, D. Tilley, *J. Therm. Biol.*, **1982**, 7, 231.
- [146] P. Wust, B. Hildebrandt, G. Sreenivasa, B. Rau, J. Gellermann, H. Riess, R. Felix, P.M. Schlag, *Lancet Oncol.*, **2002**, 3, 487–497.
- [147] G. Paltauf, P.E. Dyer, *Chem. Rev.*, **2003**, 103, 487–518.
- [148] P.K. Jain, X.H. Huang, I.H. El-Sayed, M.A. El-Sayed, *Acc. Chem. Res.*, **2008**, 41, 1578–1586.
- [149] L. Tong, Y. Zhao, T.B. Huff, M.N. Hansen, A. Wei, J.X. Cheng, *Adv. Mater.*, **2007**, 19, 3136.
- [150] V. Kotaidis, A. Plech, *Appl. Phys. Lett.*, **2005**, 87.
- [151] V.P. Zharov, E.N. Galitovskaya, C. Johnson, T. Kelly, *Lasers Surg. Med.*, **2005**, 37, 219–226.

2. Nanoparticles properties for biomedical applications

Nanoparticles (NPs) are attracting considerable interest as viable biomedical devices due to their unique physical and chemical properties. Biomedical applications of NPs include drug carriers, labeling and tracking agents, vectors for gene therapy, hyperthermia treatments, photothermal therapy, and magnetic resonance imaging (MRI) contrast agents. In order for the NPs to be useful in biomedicine, they must satisfy certain criteria. For *in vitro* applications such as fluorescent staining of proteins and TEM imaging, NPs must have minimal cytotoxicity. *In vivo*, NPs have to avoid non-specific interactions with plasma-proteins (biocompatibility) and either evade (stealthiness) or allow uptake by the reticuloendothelial system (RES) depending on the application, to reach their intended target efficiently (targeting).

2.1 Biocompatibility

Biocompatibility is, by definition, a measurement of how compatible a device is with a biological system. The purpose of performing biocompatibility testing is to determine the fitness of a device for human use, and to see whether use of the device can have any potentially harmful physiological effects [1].

A biomaterial implanted into the body induces a foreign body reaction [2][3]. The degree of this reaction depends on the properties of the device, such as shape, size, surface chemistry and roughness, design, morphology and porosity, composition, sterility issue, contact duration, and degradation [2][4][5][6][7]. In the case of a coated device, following injection, a polymer-blood interface is immediately created and nonspecific absorption of blood and tissue fluid proteins onto the surface of the device is induced [8]. In fact, the extent of nonspecific protein absorption can be used to evaluate the degree of biocompatibility of the device.

It is generally accepted that the term biocompatibility is defined not only by the lack of cytotoxicity of a biomaterial, but also by the biofunctionality of the

material, which enables it to support cell-biomaterial interactions according to the local and organ-specific situation where the biomaterial is applied [9]. Biocompatibility studies on a biomedical device for intravenous injection require complex experiments both *in vitro* and *in vivo* in order to test the local and systemic effects of the material on culture cells, tissue sections and the whole body. *In vitro* cell culture tests are often used to screen the biocompatibility of implantable devices. Such tests are sensitive, reliable, convenient and reproducible screening methods [16] [10][11]. Permanent cell lines are generally employed for such *in vitro* testing. For instance, a rat primary culture of osteoblasts is a well-established model used to investigate biocompatibility by evaluating cellular viability [12][13][14][15].

Nanoparticles for such medical applications are frequently given via intravenous administration, as with any foreign material, the body mounts a biological response to administered nanoparticles. This response is the result of a complex interplay of factors, not just the intrinsic characteristics of the nanoparticles. In particular, most materials, upon contact with biological matrices, are immediately coated by proteins, leading to a protein corona [17][18][19]. Protein coronas are complex and variable. The complete plasma proteome is expected to contain as many as 3700 proteins [20][21], of which approximately 50 have been identified in association with various nanoparticles [22][23][24][25].

Certain components of the nanoparticle corona, called opsonins, may enhance uptake of the coated material by cells of the reticuloendothelial system (RES) [26][27]. The presence of opsonins on the particle surface creates a “molecular signature” which is recognized by immune cells and determines the route of particle internalization [28][29]. The route of internalization, then, may affect the eventual fate of the nanoparticle in the body (i.e. its rate of clearance from the bloodstream, volume of distribution, organ disposition, and route of clearance from the body) [30][31].

The effect of this protein corona may have special significance for nanoparticles, due to the increased importance of surface effects for particles of this size. Several studies have shown that biological responses to nanoparticles

tend to scale with surface areas rather than mass [32][33][34][35][36]. As things become smaller, their surface areas shrink much more slowly than their volumes, causing nanoscale materials to have far greater surface-to-volume ratios than larger particles. A larger surface-to-volume ratio also implies more proteins will bind a nanoparticle (relative to its mass) than a particle of larger size. Even for larger particles, protein binding is established as one of the most important factors influencing biodistribution [37][38][39][40]. In current preclinical testing of pharmaceutical molecules, evaluation of plasma protein binding is recognized as an important element in an assessment of drug efficacy, safety and disposition [41][42]. It has been shown to be important for understanding pharmacokinetics and pharmacodynamics of the drug inside the body [41][43][44][45]. It is also used to extrapolate preclinical data to models that predicts potential drug efficacy and/or toxicity in humans [41]. For biomaterials used as medical implants, it has long been understood that the nature of the deposited protein layer onto these medical devices is responsible for the early immunological response in patients. In fact, even late stage biological responses are influenced and dictated by the surface composition of the material and how this surface interacts with surrounding tissue.

Of course, other factors play a role in determining how nanoparticles distribute within the body. These include particle properties such as size, shape, surface charge (zeta potential), solubility, surface modifications (including targeting), and route of administration.

Poly (ethylene glycol) (PEG) is a biocompatible linear synthetic polyether that can be prepared with a wide range of sizes and terminal function groups [46]. For decades variations of this polymer have been used clinically as excipients in FDA approved pharmaceutical formulations [47]. They are neutral, hydrophilic molecules in biological fluids, which help to improve the dispersity and blood circulation time of the devices they are bound to [48][49][50][51]. PEG-coated NPs are commonly regarded as stealth because they are not readily recognized by the RES [52]. This limit their use in imaging macrophages or other RES-related cells [53], but the same characteristic made them ideally suited for use in target specific cell labeling after modification targeting ligands

[54][55][56]. Among the polymeric nanoparticles for biomedical applications, biodegradable and biocompatible poly(D,L-lactic acid)/ poly(D,L-lactic/glycolic acid) (PLA/PLGA)-based nanoparticles have been investigated as carriers for therapeutic bioactive molecules [57][58][59], since PLA/PLGA have been studied for many years and are approved by the US Food and Drug Administration for human therapy [60][61][62].

2.2 *Stealthiness*

Intrinsic to the body's defense system are a series of "biological barriers" that serve to protect the body against foreign entities, including injected therapeutics and contrast agents, keeping them from reaching their intended destinations. These barriers can restrict NPs function by blocking their movement, causing physical changes to them, or by inducing a negative host response using biochemical signaling [63].

Upon intravascular injection, NPs immediately encounter blood, a high ionic strength, heterogeneous solution, that can induce NPs agglomeration, altering their properties and inducing particles sequestration. Additionally, NPs can, non-specifically, interact with plasma proteins (which can trigger the adaptive immune system), extracellular matrices, and non-targeted cell surfaces while in the blood stream. In each case, the NP is in danger of prematurely binding to or being taken by cells before reaching its target tissue.

In addition to coping with the vascular environment, NPs must overcome various anatomical size restrictions which limit their access to target tissue (e.g. extravasation of lymph-targeting NPs from the blood vessels). These size limitations are especially strict when targeting certain organs like the brain and kidney [64]. Biological barriers are not unique to extracellular spaces; in fact intracellular barriers are a critical reason why many drugs and drug delivery systems fail. Once a cell-specific NP has bound to the membrane of its target, it is typically taken up by the cell through receptor-mediated endocytosis, where it is trafficked intracellularly via endosomal compartments for processing and destruction through acidification of the endosome [65]. Most of these endosomes are then translocated into lysosomes where hydrolytic and

enzymatic reactions completely metabolize macromolecules.

Moreover, NPs biodistribution appears to be significantly influenced by its physicochemical properties [66]. Hydrodynamic size, for instance, helps govern the NPs concentration profile in the blood vessel, as well as it affects the mechanism of NPs clearance, and dictates the permeability of NPs out of the vasculature [67]. For instance, in the case of NPs clearance, it has been reported that small NPs (< 20 nm) are excreted through kidneys, while medium sized NPs (30-150 nm) have accumulated in the bone marrow, heart, kidney and stomach, and large NPs (150-300 nm) are found in the spleen and in the liver. While these size ranges provide general clearance mechanisms, other physical parameters simultaneously affect NPs mobility.

As previously discussed, NPs size affects their ability to extravasate from the vasculature. While most endothelial barriers allow NPs < 150 nm in diameter to pass, more stringent barriers, such as the blood brain barrier (BBB) are far more restrictive. The BBB allows passive diffusion of only small (< 500 Da MW), neutrally charged lipid soluble molecules, prohibiting > 98% of all potential neurotherapeutics and contrast agent from passing through.

NPs charge and hydrophobicity can affect their biodistribution as well, by limiting or enhancing their interactions with the adaptive immune system, plasma proteins, extracellular matrices and non-targeted cells [68]. Specifically, hydrophobic and charged NPs have short circulation times due to adsorption of plasma proteins (opsonization) which can lead to recognition by the reticuloendothelial system (RES), followed by removal from circulation [69]. Positively charged NPs can also bind with non-targeted cells (typically negatively charged) leading to non-specific internalization. In addition, hydrophobic groups on the surface can induce agglomeration of the NPs upon injection, leading to rapid removal by the RES.

To limit NPs-host interactions, surface engineering has led to the development of stealth NPs. Surface modification with molecules like the hydrophilic PEG have been shown to reduce the potential for opsonization through steric repulsion, prolonging NPs circulation time [70]. PEG has been introduced at the surface in two ways, either by adsorption of surfactants [71] or by using

block or branched copolymers, usually with poly(lactide) (PLA) [72][73]. As far as the adsorption of hydrophilic surfactants onto the particle surface is concerned, Illum et al. [71] studied the use of surfactants with polyoxyethylene blocks, such as the poloxamer and poloxamine series, onto polystyrene latex surfaces. In particular, they found that coating with poloxamer 407 reduced uptake by Kupffer cells but promoted uptake by the bone marrow [74]. Moghimi and co-workers [75] found that poloxamine 908 reduced liver uptake of polystyrene particles, which they interpreted as being due to reduced absorption of opsonins and increased adsorption of dysopsonins. This surfactant, even when not associated with particles, also activated phagocytic cells so that a second dose some days later was cleared rapidly by the liver. However, with the more hydrophilic biodegradable polymeric surfaces such as poly(lactide-co-glycolide) (PLGA), reversible adsorption was observed *in vivo* [76]. On the other hand, biodegradable nanospheres prepared from PLGA coated with PLA-PEG diblock copolymers showed a significant increase in blood circulation time and reduced liver uptake in a rat model, compared with naked PLGA nanoparticles [77]. Although interesting results have been obtained with adsorbed surfactants (e.g. concentration of phtalocyanines in tumors using nanocapsules coated with poloxamer 407 [78]), covalently linked copolymers would seem to be a better choice since they are less easily desorbed from the surface.

The surface characteristics (length and density of PEG chains) of nanospheres prepared from PLA-PEG copolymers have been optimized to reduce their interactions with plasma proteins and to increase their circulating half-life [72][73]. The average distance between two terminally attached chains had to be 2,2 nm or less for protein repulsion [72] and although PEG of 5kDa was more effective than PEG of 2kDa, increasing the chain length further did not confer any additional advantage at optimal surface density. Lipophilic drugs, such as lidocaine and cyclosporine A, and proteins, have been encapsulated and are released in a controlled manner [79]. PEG chains have also been attached covalently to poly(alkylcyanoacrylate) polymers by two different chemical strategies, and both types of particle have shown long-circulating properties *in*

vivo [80]. This type of particle has been loaded with tamoxifen, with a view to its use in the treatment of hormone-dependent tumors [81].

2.3 Targeting

Passive targeting uses the predetermined physicochemical properties of given NPs to specifically migrate to a given tissue region. For example, targeting of solid tumors tissue can be achieved through passive mechanism called enhanced permeation and retention (EPR) [82]. This phenomenon is based on the principle that tumor cells, in an effort to grow rapidly, stimulate production of new blood vessels (the neovasculature) that are poorly organized and have leaky fenestrations. This enables extravasation of small macromolecules and NPs out of the vasculature, into the tumor tissue [83]. Due to inefficient lymphatic drainage, there is poor clearance of these agents, leading to their selective accumulation [84]. However, EPR is limited to specific metastatic solid tumors, and successful implementation depends on a number of factors including degree of capillary disorder, blood flow, and lymphatic drainage rate making effective management difficult.

Because passive targeting is available for only certain *in vivo* applications and does not necessarily guarantee internalization of NPs by targeted cells, NPs can be additionally modified with targeting ligands to employ active cell targeting [85][86]. The devices can be decorated with targeting molecules, complementary to unique receptors on target cells, to actively target only diseased tissues; these targeting ligands can be small organic molecules [85][87][88], peptides [89][90][91][92], proteins [93], antibodies [94][95][96], and aptamers [97][98]. In addition to the type of ligand used, active targeting is affected by targeting molecules density and by the size and shape of the NPs.

Recent studies indicated that the density and molecular organization of bound ligands significantly influence NPs binding to target cells due to the multivalency phenomenon [90][99]. Multivalency is the enhanced binding avidity phenomenon observed when multiple ligands simultaneously bind with multiple receptors between two surfaces [100][101]. In addition, multivalency is also affected by NPs size [102]. In a notable study NPs of size ranging from

2 to 100 nm were decorated with targeting antibodies and evaluated for ability to bind and be internalized by targeted cells [102]. Through a series of experiments it was revealed that NPs smaller than 25 nm lack the ability to present multiple ligands to a cell unlike larger variants, limiting any potential multivalency binding effects. At the same time, larger NPs are not as readily endocytosed by cells, limiting their functionality for certain applications. Notably, NPs of 25-50 nm were revealed to be most suitable for multivalent binding and endocytosis.

For the treatment of leukemia, effective targeting of sterically stabilized liposomes containing doxorubicin and bearing anti-CD19 to malignant B cells has been observed *in vitro* and *in vivo* in mice [103]. The same liposome system has also been used to target circulating myeloma cells, in order to prevent relapse after bone marrow transplant [104]. Another cell-surface receptor which has been targeted by such “immunoliposomes” is the her2 (ErbB2) antigen [105]. In this case, a phospholipid bearing a PEG chain terminated by an anti-her2 antibody fragment was inserted into preformed commercially available doxorubicin-loaded liposomes (DoxilTM). Binding to this receptor is followed by internalization and this way the drug concentrations can be dramatically increased in her2-overexpressing tumor cells.

However, antibody-targeted systems do not always show an advantage over simple sterically stabilized liposomes in solid tumors, as observed by Allen and Moase [106] in a human ovarian tumor growing in nude mice, probably because the larger antibody-decorated particles diffuse less easily within the tumors, where the hydrostatic pressure is increased due to lack of lymphatic drainage [107]. Furthermore, such immunoliposomes can, in some cases, be opsonized and cleared rapidly from the circulation [108] and may even give rise to immunological and pseudoallergic reactions [109][110]. An approach which avoids coupling a large protein to the carrier surface is a two or three-step procedure using bispecific antibodies, which combine two immunological recognition functions in the same molecules. The antibody can therefore act as a bridge between the target cell and a carrier bearing a low-molecular-weight

ligand. For example, in the protocol described by Cao and Suresh [111], a bispecific antibody was engineered to recognize a tumor-specific antigen and biotin. This was given intravenously and after allowing time for distribution, conventional, multilamellar liposomes bearing biotin were given. This was given intravenously and after allowing time for distribution, conventional, multilamellar liposomes bearing biotin were given. These bound excess antibody in the circulation and carried it to the liver, but could not reach antibody already bound to tumor cells. A few hours later, small liposomes bearing PEG chains and biotin were administered; these could circulate, extravasate and bind to the antibody present on the surface of the tumor cells. This approach can concentrate the carrier within the tumor, but will not necessarily promote internalization, since for the procedure to function, the bispecific antibody must remain at the cell surface. However, this may be sufficient in many cases, for example, if the carrier is loaded with a radioisotope to provide local irradiation.

Another receptor which is overexpressed on many tumor cells is the folate receptor. Folic acid has some advantages over transferring or antibodies as a ligand for long-circulating carriers because it is a much smaller molecule which is unlikely to interact with opsonins and can be coupled easily to a PEG chain without loss of receptor-binding activity. This targeting strategy has been applied to long-circulating nanoparticles prepared from a cyanoacrylate-based polymer. Conjugation of folic acid to the distal end of the PEG chain does not affect its ability to bind to its receptor, as determined by surface plasmon resonance [111].

In addition to engineering NPs for tissue targeting, some researchers have used external magnetic systems to help direct magnetic NPs (MNPs) localization in a strategy called magnetic targeting [112][113]. This involves focusing high field, high gradient, or rare earth magnets on the target site, inducing accumulation of the highly magnetically susceptible MNPs. Recently this technique was successfully implemented in a clinical trial to deliver the chemotherapeutic, doxorubicin, to hepatocarcinoma cells [114]. While successful, the efficiency of magnetic targeting is limited to target tissue close

to the body's surface, due to loss of magnetic field strength further away from the magnetic source.

References

- [1] ISO 10993-1:2009.
- [2] E. Fournier, C. Passirani, C.N. Montero-Menei, J.P. Benoit, *Biomaterials*, **2003**, 24(19), 3311-31.
- [3] J.M. Anderson, A. Rodriguez, D.T. Chang, *Semin. Immunol.*, **2008**, 20(2), 86-100.
- [4] C.T. Laurencin, H. Elgendy, *New York: John Wiley & Sons*, **1994**, 27-46.
- [5] A.L. Sieminski, K.J. Gooch, *Biomaterials*, **2000**, 21(22), 2232-41.
- [6] B. Rihova, *Adv. Drug. Deliv. Rev.*, **2000**, 42, 65-80.
- [7] A.G. Mikos, L.V. McIntire, J.M. Anderson, J.E. Babensee, *Adv. Drug. Deliv. Rev.*, **1998**, 33,111-139.
- [8] D.F. Williams, *J. Mater. Sci.*, **1987**, 22, 3421-45.
- [9] D. Rickert, A. Lendlein, I. Peters, M.A. Moses, R.P. Franke, *Eur. Arch. Otorhinolaryngol.*, **2006**, 263(3), 215-22.
- [10] M.H. Santos, P. Valerio, A.M. Goes, M.F. Leite, L.G. Heneine, H.S. Mansur, *Biomed. Mater.*, **2007**, 2(2), 135-41.
- [11] C.J. Kirkpatrick, F. Bittinger, M. Wagner, H. Köhler, T.G. van Kooten, C.L. Klein, M. Otto, *Proc. Inst. Mech. Eng. [H].*, **1998**, 212(2), 75-84.
- [12] A. Ito, H. Kawamura, M. Otsuka, M. Ikeuchi, H. Ohgushi, K. Ishikawa, K. Onuma, N. Kanzaki, Y. Sogo, N. Ichinose, *Mater. Sci. Eng. C.*, **2002**, 22, 21-25.
- [13] T.J. Webster, E.A. Massa-Schlueter, J.L. Smith, E.B. Slamovich, *Biomaterials.*, **2004**, 25(11), 2111-2121.
- [14] P. Valerio, M.M. Pereira, A.M. Goes, M.F. Leite, *Biomaterials*, **2004**, 25(15), 2941-2948.
- [15] B.V. Sampaio, G. Goller, F.N. Oktar, P. Valerio, A.M. Goes, M.F. Leite, *Key Eng. Mater.*, **2005**, 284-286, 639-42.
- [16] S.C. Mendes, R.L. Reis, Y.P. Bovell, A.M. Cunha, C.A. van

- Blitterswijk, J.D. de Bruijn, *Biomaterials.*, **2001**, 22(14), 2057-2064.
- [17] T. Cedervall, I. Lynch, S. Lindman, T. Berggard, E. Thulin, H. Nilsson, K.A. Dawson, S. Linse, *Proc. Natl. Acad. Sci. USA*, **2007**, 104, 2050–2055.
- [18] B. Sahoo, M. Goswami, S. Nag, S. Maiti, *Chem. Phys. Lett.*, **2007**, 445, 217–220.
- [19] I. Lynch, K.A. Dawson, *NanoToday*, **2008**, 3, 40–47.
- [20] T. Cedervall, I. Lynch, M. Foy, T. Berggard, S.C. Donnelly, G. Cagney, S. Linse, K.A. Dawson, *Angew. Chem., Int. Ed. Engl.*, **2007**, 46, 5754–5756.
- [21] I. Lynch, T. Cedervall, M. Lundqvist, C. Cabaleiro-Lago, S. Linse, K.A. Dawson, *Adv. Colloid Interface Sci.*, **2007**, 134, 167–174.
- [22] M.A. Dobrovolskaia, A.K. Patri, J. Zheng, J.D. Clogston, N. Ayub, P. Aggarwal, B.W. Neun, J.B. Hall, S.E. Mcneil, *Nanomedicine*, **2009**, 5(2), 106-117.
- [23] T.M. Goppert, R.H. Muller, *Eur. J. Pharm. Biopharm.*, **2005**, 60, 361–372.
- [24] H.R. Kim, K. Andrieux, C. Delomenie, H. Chacun, M. Appel, D. Desmaele, F. Taran, D. Georgin, P. Couvreur, M. Taverna, *Electrophoresis*, **2007**, 28, 2252–2261.
- [25] K. Thode, M. Luck, W. Semmler, R.H. Muller, M. Kresse, *Pharm. Res.*, **1997**, 14, 905–910.
- [26] H.M. Patel, *Crit. Rev. Ther. Drug Carr. Syst.*, **1992**, 9, 39–90.
- [27] A. Chonn, S.C. Semple., P.R. Cullis, *J. Biol. Chem.*, **1992**, 267, 18759–18765.
- [28] H. Kiwada, T. Miyajima, Y. Kato, *Chem. Pharm. Bull.*, **1987**, 35, 1189–1195.
- [29] D.A. Tyrrell, V.J. Richardson, B.E. Ryman, *Biochim. Biophys. Acta*, **1977**, 497, 469–480.
- [30] T.M. Goppert, R.H. Muller, *J. Drug Target.*, **2005**, 13, 179–187.
- [31] R.H. Muller, S. Heinemann, Surface modelling of microparticles as parenteral systems with high tissue affinity, in: R. Gurny, H.E.

- Junginger (Eds.), Bioadhesion- Possibilities and Future Trends, Wissenschaftliche Verlagsgesellschaft, Stuttgart, **1989**, 202–213.
- [32] D.M. Brown, M.R. Wilson, W. MacNee, V. Stone, K. Donaldson, *Toxicol. Appl. Pharmacol.*, **2001**, 175, 191–199.
- [33] K. Donaldson, D. Brown, A. Clouter, R. Duffin, W. MacNee, L. Renwick, L. Tran, V. Stone, *J. Aerosol Med.*, **2002**, 15, 213–220.
- [34] K. Donaldson, X.Y. Li, W. Macnee, *J. Aerosol Sci.*, **1998**, 29, 553–560.
- [35] G. Oberdorster, J. Ferin, R. Gelein, S.C. Soderholm, J. Finkelstein, *Environ. Health Perspect.*, **1992**, 97, 193–199.
- [36] C.L. Tran, D. Buchanan, R.T. Cullen, A. Searl, A.D. Jones, K. Donaldson, *Inhal. Toxicol.*, **2000**, 12, 1113–1126.
- [37] D. Dutta, S.K. Sundaram, J.G. Teeguarden, B.J. Riley, L.S. Fifield, J.M. Jacobs, S.R. Addleman, G.A. Kaysen, B.M. Moudgil, T.J. Weber, *Toxicol. Sci.*, **2007**, 100, 303–315.
- [38] A. Gessner, A. Lieske, B. Paulke, R. Muller, *Eur. J. Pharm. Biopharm.*, **2002**, 54, 165–170.
- [39] T.M. Goppert, R.H. Muller, *Int. J. Pharm.*, **2005**, 302, 172–186.
- [40] M. Luck, B.R. Paulke, W. Schroder, T. Blunk, R.H. Muller, *J. Biomed. Mater. Res.*, **1998**, 39, 478–485.
- [41] F.M. Musteata, J. Pawliszyn, M.G. Qian, J.T. Wu, G.T. Miwa, *J. Pharm. Sci.*, **2006**, 95, 1712–1722.
- [42] R.E. Olson, D.D. Christ, *Annu. Rep. Med. Chem.*, **1996**, 31, 327–336.
- [43] M.J. Banker, T.H. Clark, J.A. Williams, *J. Pharm. Sci.*, **2003**, 92, 967–974.
- [44] I. Kariv, H. Cao, K.R. Oldenburg, *J. Pharm. Sci.*, **2001**, 90, 580–587.
- [45] S. Sarre, K. Van Belle, I. Smolders, G. Krieken, Y. Michotte, *J. Pharm. Biomed. Anal.*, **1992**, 10, 735–739.
- [46] R.I. Mahato, *CRC Press*, **2005**.
- [47] F. Fuertges, A. Abuchowski, *J. Controlled Release*, **1990**, 11, 139–148.
- [48] S.M. Moghimi, A.C. Hunter, J.C. Murray, *Pharmacol. Rev.*, **2001**, 53, 283–318.

- [49] Y. Zhang, N. Kohler, M.Q. Zhang, *Biomaterials*, **2002**, 23, 1553-1561.
- [50] J. Xie, C. Xu, N. Kohler, Y. Hou, S. Sun, *Adv. Mat.*, **2007**, 19, 3163-3166.
- [51] L.X. Tiefenauer, A. Tschirky, G. Kuhne, R.Y. Andres, *Magn. Res. Imaging*, **1996**, 14, 391-402.
- [52] J.M. Harris, R.B. Chess, *Nature Rev. Drug Disc.*, **2003**, 2, 214-221.
- [53] M.I. Papisov, A. Bogdanov, B. Schaffer, N. Nossiff, T. Shen, R. Weissleder, T.J. Brady, *J. Magn. Magn. Mat.*, **1993**, 122, 383-386.
- [54] C. Sun, C. Fang, Z. Stephen, O. Veiseh, S. Hansen, D. Lee, R.G. Ellenbogen, J. Olson, M.Q. Zhang, *Nanomedicine*, **2008**, 3, 495-505.
- [55] C. Sun, O. Veiseh, J. Gunn, C. Fang, S. Hansen, D. Lee, R. Sze, R.G. Ellenbogen, J. Olson, M. Zhang, *Small*, **2008**, 4, 372-379.
- [56] X. Chen, W. Zhang, J. Laird, S.L. Hazen, R.G. Salomon, *J. of Lipid Res.*, **2008**, 49, 832-846.
- [57] M.T. Peracchia, *Pharma. Sci.*, **2003**, 13, 155-161.
- [58] K. Avgoustakis, *Curr. Drug Deliv.*, **2004**, 1, 321-333.
- [59] A. Beletsi, Z. Panagi, K. Avgoustakis, *Int. J. Pharm.*, **2005**, 298, 233-241.
- [60] H. Okada, H. Toguchi, *Crit. Rev. Ther. Drug Carrier Syst.*, **1995**, 12, 1-99.
- [61] J.M. Anderson, M.S. Shive, *Adv. Drug Deliv. Rev.*, **1997**, 28, 5-24.
- [62] C.E. Astete, C.M. Sabliov, *J. Biomater. Sci. Polym. Ed.*, **2006**, 17, 247-289.
- [63] A. Solanki, J.D. Kim, K.B. Lee, *Nanomedicine*, **2008**, 3, 567-578.
- [64] M. Longmire, P.L. Choyke, H. Kobayashi, *Nanomedicine*, **2008**, 3, 703-717.
- [65] L.A. Bareford, P.W. Swaan, *Adv. Drug Deliv. Rev.*, **2007**, 59, 748-758.
- [66] T. Reschel, C. Konak, D. Oupicky, L.W. Seymour, K. Ulbrich, *J. Control. Rel.*, **2002**, 81, 201-217.
- [67] M.D. Chavanpatil, A. Khair, J. Panyam, *J. of Nanoscience and Nanotechnology*, **2006**, 6, 2651-2663.
- [68] M.E. Davis, *Curr. Opin. In Biotech.*, **2002**, 13, 128-131.

- [69] C. Chouly, D. Pouliquen, I. Lucet, J.J. Jeune, P. Jallet, *J. of Microencapsulation*, **1996**, 13, 245-255.
- [70] J.M. Harris, R.B. Chess, *Nature Rev. Drug Disc.*, **2003**, 2, 214-221.
- [71] L. Illum, L.O. Jacobsen, R.H. Müller, R. Mak, S.S. Davis, *Biomaterials*, **1987**, 8, 113-117.
- [72] R. Gref, A. Domb, P. Quellec, T. Blunk, R.H. Müller, J.M. Verbavatz, *Adv. Drug Deliv. Rev.*, **1995**, 16, 215-233.
- [73] D. Bazile, C. Prud'Homme, M.T. Bassoulet, M. Marlard, G. Spenlehauer, M. Veillard, *J. Pharm. Sci.*, **1995**, 84, 493-498.
- [74] M.E. Norman, P. Williams, L. Illum, *Biomaterials*, **1993**, 14, 193-202.
- [75] S.M. Moghimi, I. Muir, L. Illum, S. Davis, V. Kolb-Bachofen, *Biochim. Biophys. Acta*, **1993**, 1179, 157-165
- [76] S.E. Dunn, A.G.A. Coombes, M.C. Garnett, S.S. Davis, M.C. Davies, L. Illum, *J. Control. Release*, **1997**, 44, 65-76.
- [77] S. Stolnik, S.E. Dunn, M.C. Garnett, M.C. Davies, A.G.A. Coombes, D.C. Taylor, *Pharm. Res.*, **1994**, 11, 1800-1808
- [78] V. Lenaerts, A. Labib, F. Chouinard, J. Rousseau, H. Ali, J. van Lier, *Eur. J. Pharm. Biopharm.*, **1995**, 41, 38-43.
- [79] P. Quellec, P. Gref, L. Pervun, E. Dellacherie, F. Sommer, Y.M. Verbavatz, *J. Biomed. Mater. Res.*, **1998**, 42, 45-54.
- [80] M.T. Peracchia, D. Desmaële, C. Vauthier, D. Labarre, E. Fattal et al., *Targeting of Drugs*, **1998**, 222-239, Gregoriadis G. and McCormack B. (eds), Plenum, New York.
- [81] I. Brigger, P. Chaminade, V. Marsaud, M. Appel, M. Besnard, R. Gurny, *Int. J. Pharm.*, **2001**, 214, 37-42.
- [82] H. Maeda, J. Wu, T. Sawa, Y. Matsumura, K. Hori, *J. of Control. Release*, **2000**, 65, 271-284.
- [83] R.K. Jain, *Annual Rev. of Biomed. Eng.*, **1999**, 1, 241-263.
- [84] S.E. Mnneil, *J. of Leukocyte Bio.*, **2005**, 78, 585-594.
- [85] Y. Zhang, N. Kohler, M.Q. Zhang, *Biomaterials*, **2002**, 23, 1553-1561.
- [86] R. Sinha, G.J. Kim, S.M. Nie, D.M. Shin, *Molecular Cancer Therapeutics*, **2006**, 5, 1909-1917.

- [87] N. Kohler, C. Sun, J. Wang, M.Q. Zhang, *Langmuir*, **2005**, 21, 8858-8864.
- [88] C.Sun, R. Sze, M.Q. Zhang, *J. of Biomed. Mar. Res. Part A*, **2006**, 78A, 550-557.
- [89] O. Veiseh, C. Sun, J. Gunn, N. Kohler, P. Gabikian, D. Lee, N. Bhattarai, R. Ellenbogen, R. Sze, A. Hallahan, J. Olson, M.Q. Zhang, *Nano Letters*, **2005**, 5, 1003-1008.
- [90] X. Montet, K. Montet-Abou, F. Reynolds, R. Weissleder, L. Josephson, *Neoplasia*, **2006**, 8, 214-222.
- [91] X. Montet, R. Weissleder, L. Josephson, *Bioconj. Chem.*, **2006**, 17, 905-911.
- [92] S. Boutry, S. Laurent, L. Vander Elst, R.N. Muller, *Contrast Media & Molecular Imaging*, **2006**, 1, 15-22.
- [93] J. Gunn, H. Wallen, O. Veiseh, C. Sun, C. Fang, J.H. Cao, C. Yee, M.Q. Zhang, *Small*, **2008**, 4, 712-715.
- [94] D. Artemov, N. Mori, B. Okollie, Z.M. Bhujwala, *Magn. Res. in Medicine*, 2003, 49, 403-408.
- [95] F.Q. Hu, L. Wei, Z. Zhou, Y.L. Ran, Z. Li, M.Y. Gao, *Adv. Mat.*, **2006**, 18, 2553-2556.
- [96] Y.M. Huh, Y.W. Jun, H.T. Song, S. Kim, J.S. Choi, J.H. Lee, S. Yoon, K.S. Kim, J.S. Shin, J.S. Suh, J. Cheon, *J. of Am. Chem. Soc.*, **2005**, 127, 12387-12391.
- [97] M.V. Yigit, D. Mazumdar, H.K. Kim, J.H. Lee, B. Dintsov, Y. Lu, *ChemBioChem*, **2007**, 8, 1675-1678.
- [98] M.V. Yigit, D. Mazumdar, Y. Lu, *Bioconj. Chem.*, **2008**, 19, 412-417.
- [99] S. Hong, P.R. Leroueil, I.J. Majoros, B.G. Orr, J.R. Baker, M.M.B. Holl, *Chemistry & Biology*, **2007**, 14, 105-113.
- [100] D. Wright, L. Usher, *Curr. Org. Chem.*, **2001**, 5, 1107-1131.
- [101] P.J. Munson, D. Rodbard, *Endocrinology*, **1979**, 105, 1377-1381.
- [102] W. Jiang, B.Y.S. Kim, J.T. Rutka, W.C.W. Chan, *Nature Nanotechnology*, **2008**, 3, 145-150.
- [103] D. Lopes de Menezes, L. Pilarski, T.M. Allen, *Cancer Res.*, **1998**,

- 58, 3320–3330.
- [104] D.E. Lopes de Menezes, L.M. Pilarski, A.R. Belch, T.M. Allen, *Biochim. Biophys. Acta*, **2000**, 1466, 205–220.
- [105] J.W. Park, D.B. Kirpotin, K. Hong, R. Shalaby, Y. Shao, U.B. Nielsen, *J. Control. Release*, **2001**, 74, 95–113.
- [106] T.M. Allen, E.H. Moase, *Adv. Drug Deliv. Rev.*, **1996**, 21, 117–133.
- [107] R.K. Jain, *Cancer Metastasis Rev.*, **1987**, 6, 559–593.
- [108] J. Barbet, *Liposomes: New Systems and New Trends in Their Applications*, **1995**, pp. 159–191, Puisieux F., Couvreur P., Delattre J. and Devissaguet J.-P. (eds), Editions de Santé, Paris.
- [109] N.C. Phillips, L. Gagné, C. Tsoukas, J. Dahman, *J. Immunol.*, **1994**, 152, 3168–3174.
- [110] J. Szebeni, *Crit. Rev. Ther. Drug Carrier Syst.*, **2001**, 18, 567–606.
- [111] Y. Cao, M.R. Suresh, *J. Drug Target.*, **2000**, 8, 257–266.
- [112] J. Dobson, *Drug Dev. Res.*, **2006**, 67, 55-60.
- [113] S.C. McBain, U. Griesenbach, S. Xenariou, A. Keramane, C.D. Batich, E. Alton, J. Dobson, *Nanotechnology*, **2008**, 19.
- [114] M.W. Wilson, R.K. Kerlan, N.A. Fidelman, A.P. Venook, J.M. LaBerge, J. Koda, R.L. Gordon, *Radiology*, **2004**, 230, 287-293.

3. Nanoparticles preparation strategies for biomedical applications

As explained previously nanoparticles for biomedical applications must be biocompatible and stealth, to this end so have to be reagents and solvents used during the preparation. Moreover, the synthesis byproducts must be limited and controlled, and the material obtained must be stable for a long time under peculiar conditions (pH, temperature, ...). For these reasons only some preparation methods are compatible to this kind of application.

3.1 Photopolymerization

Except for specific references, this chapter has been written according the following books:

C.G Roffey, Photopolymerization of Surface Coatings, John Wiley & Sons, Chichester, 1982.

J.P. Fouassier, J.F. Rakek, Radiation curing in Polymer Science and Technology, Elsevier London, 1993.

S. P. Pappas, Radiation curing science and technology, Plenum Press, New York, 1992.

S. Penczek, P. Kubisa, .Ring opening polymerization, P. J. Brunelle, Hanser, Munich 1993

Photopolymerization is a technique that through the reaction of monomer or oligomer activated by a light induced initiation leads to the formation of polymer (if monomer or oligomers are monofunctional) or, usually, 3D cross-linked polymers (starting from multifunctional monomers). The general idea beyond all the photopolymerization processes involves reaction and solidification of the liquid precursor into a stable polymeric structure with tailored physical, chemical and mechanical properties using light, usually in UV range but, in some case, also in the visible region.

In a typical UV curing process multifunctional monomers, or oligomers, are converted into a cross-linked polymer by means of a chain reaction initiated by

reactive species (free radical or ions), which are generated by UV irradiation. Considering that a photochemical process (like photopolymerization) can occur only if the radiation absorbed by the medium induce a chemical reaction, and that most monomers are not able to produce initiating species when exposed to UV light, in order to activate the process it is necessary to introduce a photoinitiator in the initial photocurable mixture. The whole process is schematically reported in Figure 3.1.

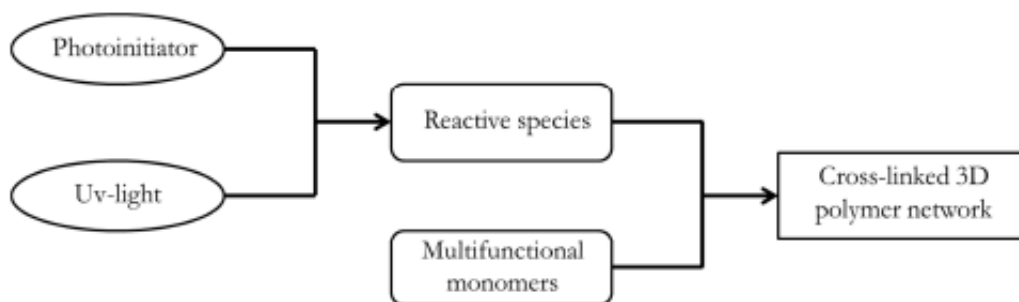


Figure 3.1: General representation of a photocuring process

In general, a photocurable formulation contains:

- Photoinitiator: the chemical species that, by absorbing the light, generate the reactive species. Generated species, depending on the functionalities of the monomer to cure, could be either radicals or cation or anion.
- A reactive diluent to adjust the viscosity of the formulation for its application. Usually it is also involved into the polymerization mechanism.
- Monomers or oligomers that usually possess multifunctionalities in order to generate a cross-linked network. Chemical structure of the backbone confers to the cured polymer the physical and mechanical properties.

While the monomers have a predominant role on the physical-chemical properties of the cured material, photoinitiator rules on the curing rate and production. First of all, molecular absorption coefficient of the photoinitiator determines the amount of light absorbed, i.e. energy utilized in the reaction. Moreover if the efficiency of the photoinitiator is high, its concentration could

be reduced in the formulation reducing the price and, at the same time, reducing problems involved with high concentration of photoinitiator (e.g. yellowing of the cured polymers).

There are two major classes of photocurable resins that differ for the polymerization mechanism:

- Photoinitiated free radicals polymerization, for the polymerization of acrylate, methacrylates and unsaturated polyesters resins.
- Photoinitiated cationic polymerization, for the epoxy, vinyl ethers and propenylethers resins.

Radical photopolymerization is defined as a polymerization initiated by the light in which both initiating species and growing chain ends are radicals. With this process, as far as for the classical thermal activated, it's possible to obtain high molecular weight chains or crosslinked. First of all, it is important to point out that in all the photopolymerization mechanisms absorption of the incident light, by any photoactive component of the pristine mixture able to generate, in some way, an initiating species it's a determinant prerequisite. In radical photopolymerization, radiation energy could be directly absorbed by a photosensitive species that could undergo to homolytic break of the covalent bond and generate a radical which may initiate the photopolymerization. This compound could be a monomer but, in the greatest part of the cases, it's another molecule called photoinitiator. However in some case, the species that absorb the photons energy are not able to create a radical. These compounds, called sensitizers, transfer their electronic excitation to other reactive constituents in the curable mixture that are able to generate the radicals and so, under the right conditions, start the polymerization reaction.

Free radical photopolymerization mechanism consists in four steps, as reported in Figure 3.2:

- Photoinitiation. In this step the light is directly absorbed by the photoinitiator, or an excited sensitizer transfers its energy to another species. In both cases, with different mechanisms, creation of a radical that reacts with a monomeric unit occurs.

- Propagation. In this step a consecutive addition of monomer takes place. This reaction leads to the formation of the polymer backbone through the radical chain growth mechanism.
- Chain transfer. Growing chains could terminate by a hydrogen abstraction that could occur in many ways (e.g. reactions with other monomers, other growing chains, photoinitiator). At the same time new radical are generated and they could start another chain addition.
- Termination. The growing chains are terminated by disproportion or recombination with other growing chains or monomers or primary radicals produced in the photoinitiation step.

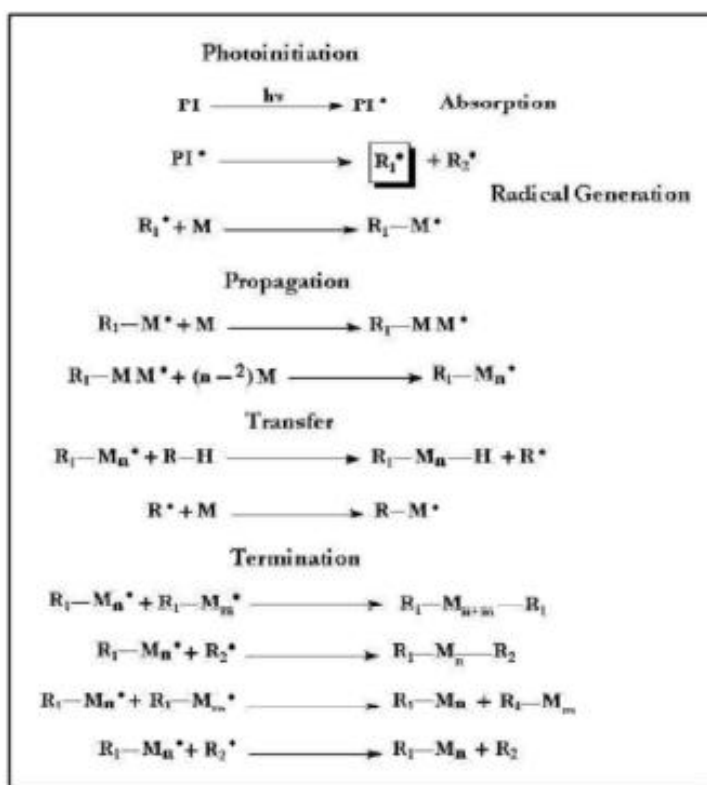


Figure 3.2: Photoinitiated free radical polymerization mechanism. PI is the photoinitiator, R is the radicals generated and M the monomers.

It is important to underline that light plays a role only in the first step of the photopolymerization, the photoinitiation, because light absorption is necessary in order to generate active species. All the other steps could occur even in the

dark because they are purely thermal controlled process (propagation and termination rate are both temperature dependent).

Regarding the photoinitiators it is possible to divide them in two categories according with the pathway to generate the reactive species:

- By photocleavage, if, once absorbed the light, the photoinitiator generates radicals by intramolecular scission (Norrish type I), Figure 3.3.
- By hydrogen abstraction, generating the radicals by abstraction of a hydrogen atom from a donor molecule (Norrish type II), Figure 3.3.

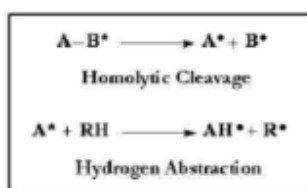


Figure 3.3: Norrish I and Norrish II type mechanisms

The most diffused Norrish I type photoinitiators are aromatic carbonyl compounds, e.g. benzoin ether derivatives and benzilketals, that undergo to homolytic scission of the C-C bond after UV exposure, generating two radicals fragments (Figure 3.4).

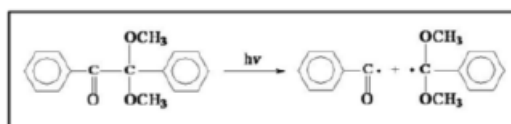


Figure 3.4: Radical formation in 2,2-Dimethoxy-2-phenylacetophenone

Norrish II type photoinitiators includes aromatic ketons, e.g. benzophenone, thioxanthone and camphorquinone. Under UV light there isn't any cleavage of a covalent bond but an abstraction of a hydrogen atom from a H-donor molecule (usually H is abstracted from a monomer). In this way a ketyl radical and a donor radical are generated, according to Figure 3.5.

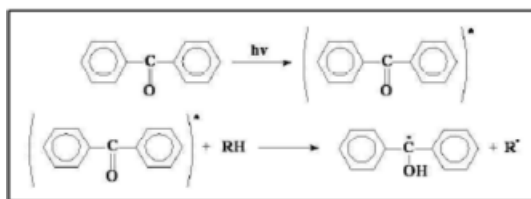


Figure 3.5: Radicals formation mechanism from benzophenone

Light-induced free radical polymerization is the most used technique for industrial applications even because for the large source of monomer available and the possibility to have waterborne resins. In the market curing of coatings on wood, metal and paper, adhesives, printing inks and photoresists applications are practically based on photoinitiated radical polymerization. On the other side this method presents several drawbacks such as volatility of many photocurable compounds, unpleasant odor (most of all by acrylic and methacrylic resins), toxicity of unreacted groups and monomers, and large shrinkage. Moreover the process has the disadvantage that it must be carried out in inert atmosphere (e.g. nitrogen, argon, carbon dioxide or vacuum) because it suffers from oxygen inhibition. Free radicals generated by the photolysis of the initiator are rapidly scavenged by O_2 molecules to yield peroxy radicals [1]. These are not reactive towards the double bonds present in the photocurable compounds and can therefore not initiate the polymerization reaction. They usually abstract hydrogen atoms from the polymer backbone to generate hydroperoxides (See Figure 3.6). This modification of curing reaction also influences strongly the properties of the cured materials [2]. An additional amount of photoinitiator (and of UV energy) is therefore needed to consume the oxygen dissolved in the resin, reducing the rate of photopolymerization.

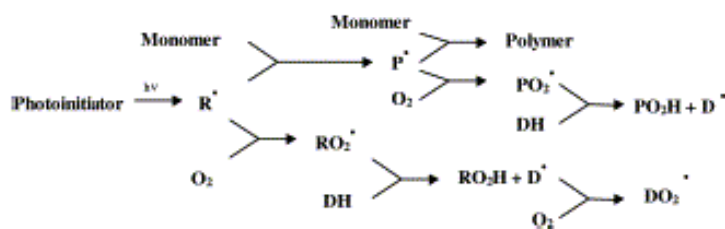


Figure 3.6: Oxygen inhibition mechanisms in free radical photopolymerization

Initiation reaction is a multistep process that first involves the absorbing of the radiation and thus the excitation of the onium salts. The generated excited singlet state could then decay with both heterolytic and homolytic cleavages. The resulting free radicals, cation and cationradical fragments are very reactive with monomers. Hence a Brønsted Acid is formed and, actually, this species initiates the polymerization reaction. The Brønsted acid could also be indicated as HMtXn where MtXn^- is the anionic part. It must have non-nucleophile behavior because otherwise any cationic species generated during the photolysis or during chain growth mechanism would give termination reaction by combination with this anion. According with their nucleophilicity, the most used counterions are PF_6^- , AsF_6^- , SbF_6^- and BF_4^- .

Of course the type of anion also determines the strength of the Brønsted acid produced in the photolysis reaction. The more stable are the anions the higher is the strength of the superacid generated. The order of reactivity is $\text{SbF}_6^- > \text{AsF}_6^- > \text{PF}_6^- > \text{BF}_4^-$.

Epoxides and Vinyl ethers are the most employed cationic photocurable compounds. While the polymerization of Vinyl ethers occurs by addition of a carbocation on the double bond, epoxy polymerization occurs by ring opening polymerization. This mechanism involves opening and polymerizing cyclic functionalities and lead to the production of a linear polymer. Bifunctional or multifunctional monomers lead to the formation of 3D cross-linked network [3].

3.2 Click chemistry

“Click chemistry” is a relatively new approach of direct conjugation, developed by Sharpless et al almost a decade ago. Specifically “click reactions” are fast, efficient, require mild reaction conditions (aqueous environment, relatively neutral pH), and create water-soluble and biocompatible linkages (electron configuration similar to amide bonds)[4]. Compared to other direct conjugation strategies, this method of attachment offers several unique features.

The “Click chemistry” focuses on the extraordinary power of a very few

reactions which form desired bonds under diverse reaction conditions, with highly diverse building blocks, in high yields and with no byproducts [5]. Recent studies demonstrated that “click” chemistry meets the criteria of being applicable under aqueous conditions, efficient, orthogonal to thiol and amine containing targeting motifs, and stable in the complex *in vivo* environments of the blood and tumor milieu [6].

3.2.2 Thiol-ene addition

Thiol-ene is a free-radical reaction that proceeds by a step-growth mechanism, involving two main steps, a free-radical addition followed by a chain transfer reaction [7][8]; this reaction is well known for occurring in absence of any radical photoinitiator [9].

With this technique it is possible to form a three dimensional crosslinked polymer when either the thiol and the ene monomers has a functionality greater than two, whereas a linear polymer is produced upon reaction of difunctional thiol with difunctional ene. Therefore, to obtain highly uniform crosslinked networks, thiol-ene systems are based on a mixture of a poly-ene and multifunctional thiols that polymerize by a free radical reaction. Typical examples of a multifunctional thiol and a multifunctional ene are reported in Figure 3.7.

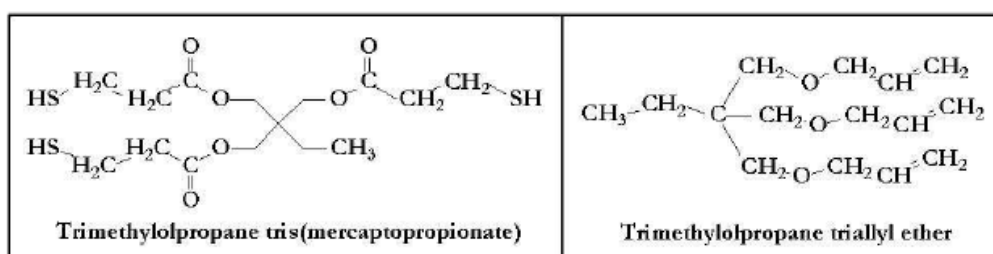


Figure 3.7: Typical multifunctional thiol and ene.

Thiol-ene addition reaction was discovered as early as 1905 by Posner and since then the reaction mechanism, polymerization kinetics and monomers reactivity were extensively explored [10]. As explained before, the polymerization proceeds by a step-growth mechanism, involving a free radical

addition followed by a chain-transfer reaction [11], as illustrated in Figure 3.8.

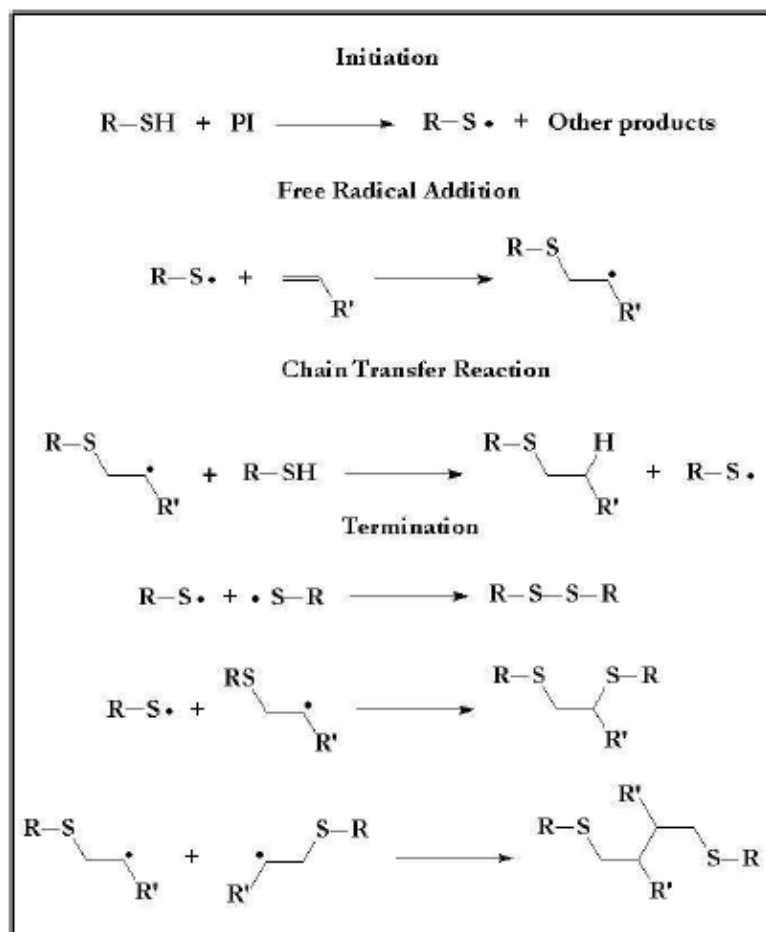


Figure 3.8: Thiol-ene free radical step growth mechanism.

The free radical chain mechanism involves two different steps: an initial addition of a thiyl radical to the carbon of an ene functionality and a subsequent hydrogen abstraction of a thiol group by a carbon-centered radical to form a thiyl radical. Termination occurs through a bimolecular recombination of a couple of radicals [11]. The two steps process, as shown in Figure 3.9, results in the addition of a thiol group across an ene double bond.

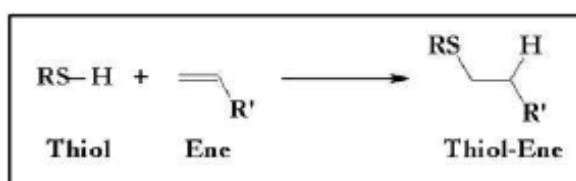


Figure 3.9: Addition of a thiol group across an ene double bond.

The step growth nature of the polymerization produces a homogeneous uniform crosslinked network with high conversion rates, resulting in reduced overall shrinkage and excellent adhesion.

As any free radical polymerization process, there are a number of ways of initiating thiol-ene polymerization, including: the excitation of a diarylketone followed by hydrogen transfer, the excitation of an aryl aliphatic ketone followed by α -bond cleavage and the direct excitation of the thiol followed by a lysis of the sulfur-hydrogen bond. A diarylketone, such as benzophenone (BP), can be excited to its singlet state upon irradiation with UV light of sufficient energy and this can be followed by an efficient intersystem crossing to the triplet state [12][13]. In the presence of thiols, there is an efficient hydrogen transfer from the thiol to the excited triplet state of the diarylketone resulting in the formation of a thiyl radical and a semipinacol radical. Once formed, the thiyl radical initiates the polymerization process by inserting into the carbon-carbon double bond of the ene to give a carbon-centered radical, thus initiating the two steps chain process, as can be observed in Figure 3.10.

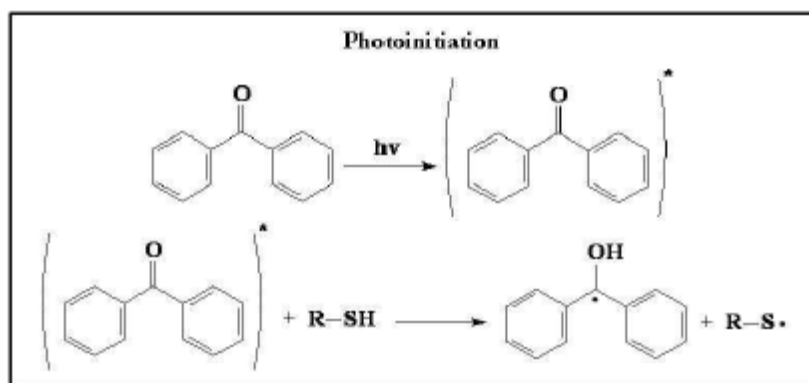


Figure 3.10: Photoinitiation of thiol-ene free radical polymerization with a photoinitiator.

This process of initiation, although quite inefficient because of the inability of the semipinacol radical either to insert into the carbon-carbon double bond or to abstract hydrogen atoms efficiently, does result in reasonable polymerization rates because of the rapid propagation rates for thiol-ene photopolymerizations. Unfortunately, if BP or some other diarylketone is used to initiate thiol-ene

process, most of the diarylketone remains unconsumed at the end of the reaction and remains in the final material as a plasticizer and photoreactive species [14]. In order to overcome this drawback, it should be possible to severely hinder the long term stability of the thiol-ene materials exposed to sunlight, or even certain types of room light, using a N-substituted maleimides, as excited species, which are able to abstract a hydrogen atom from the labile thiol group [15][16][17][18]. Because maleimides are quite reactive in free radical processes they are consumed by the radical chain process that they initiate and hence do not remain in the final material after exposure. Although this eliminates the problem of residual photoinitiator in the thiol-ene material, maleimides are toxic and this limits their use. Thiol-ene polymerization can also be initiated by the excitation of cleavage photoinitiators, such as a dimethoxyphenyl acetophenone (DMPA), which give a benzoyl radical and a tertiary carbon radical upon the absorption of a photon of light. A rearrangement of the tertiary carbon radical occurs, yielding a methyl radical and methyl benzoate. The methyl and benzoyl radicals may insert into a carbon-carbon bond directly or abstract a hydrogen from a thiol group. In either case, the two-step process characteristic of the thiol-ene free-radical chain reaction illustrated in Figure 3.8 is initiated [10]. Although not being as efficient as initiation by either hydrogen-abstraction or α -cleavage processes, it is still possible to excite directly the thiol and induce the cleavage of the labile sulfurhydrogen bond, as shown in the reaction of Figure 3.11.

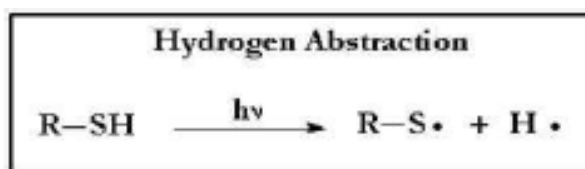


Figure 3.11: Photoinitiation by direct excitation of a thiol.

One of the most attractive feature of thiol-ene polymerization is that any type of ene and thiol molecule can be incorporated into the thiol-ene network. Most authors today use the term “thiol-ene” to describe the reaction of thiols with a wide variety of unsaturated functional groups such as acrylates, vinyl ethers,

allyl ethers, alkenes and norbornenes, in addition to inactivated carbon–carbon double bonds [19]. Moreover, different kind of multifunctional thiols can be used such as alkyl thiols, thiol glycolate esters and thiol propionate esters.

Because the choice of enes to copolymerize with different thiols is essentially endless, it should be possible to tailor the molecular composition and so the final properties of the new materials. The thiol-ene reaction has all the desirable features of a “click” reaction being highly efficient, simple to execute with no side products and proceeding rapidly to high yield [20]. Furthermore, the thiol-ene polymerization is most frequently photoinitiated, particularly for polymerizations resulting in highly uniform polymer networks, promoting unique capabilities related to spatial and temporal control of the click reaction.

Photopolymerization is an efficient, environmentally friendly and economically favorable method to produce materials, which can display a wide range of properties depending on the identity of the reactive species and additives employed [21]. Thiol-ene photopolymerizations have an extensive list of significant advantages in regards to the other polymerization processes and the resulting polymer properties. The thiol-ene crosslinking reactions proceeds very rapidly in air but will not reach the gel point until relatively high functional group conversions in contrast to the traditional free-radical formulations which are normally inhibited by oxygen [22][23][24][25][26][27][28][29][30].

In addition, thiol-ene systems are characterized by low polymerization shrinkage, insensitivity of oxygen inhibition effect, relatively high conversion, high refractive index, photoinitiator free polymerization and also homogeneous polymer structures and, as so, allow to obtain high performance photocured polymers.

As mentioned earlier, in thiol-ene polymerizations a broad spectrum of physical properties is achieved because of the great number of monomers that can take place in the free radical step grow mechanism. One of the most important aspects of the thiol-ene photoinitiated radical polymerization is its relative insensitivity to oxygen inhibition, a problem that generally plagues the free radical processes [10]. The presence of oxygen in traditional formulations

often causes the inhibition effect of polymerization and leads to low curing rate, low conversion of monomers and successive flaws of cured products. The oxygen in polymerization system will consume the highly reactive free radicals and form peroxide radicals that have quite low reactivity toward radical polyaddition reaction. However, for thiol-ene photopolymerizations, which proceed through a step-growth mechanism, the thiol groups can react with the peroxide radicals and generate highly reactive thiyl radicals after hydrogen abstraction by the peroxide radicals, as can be observed in Figure 3.12. Thus, the thiol-ene photopolymerization can achieve high photopolymerization rate and high conversion [14][28][29].

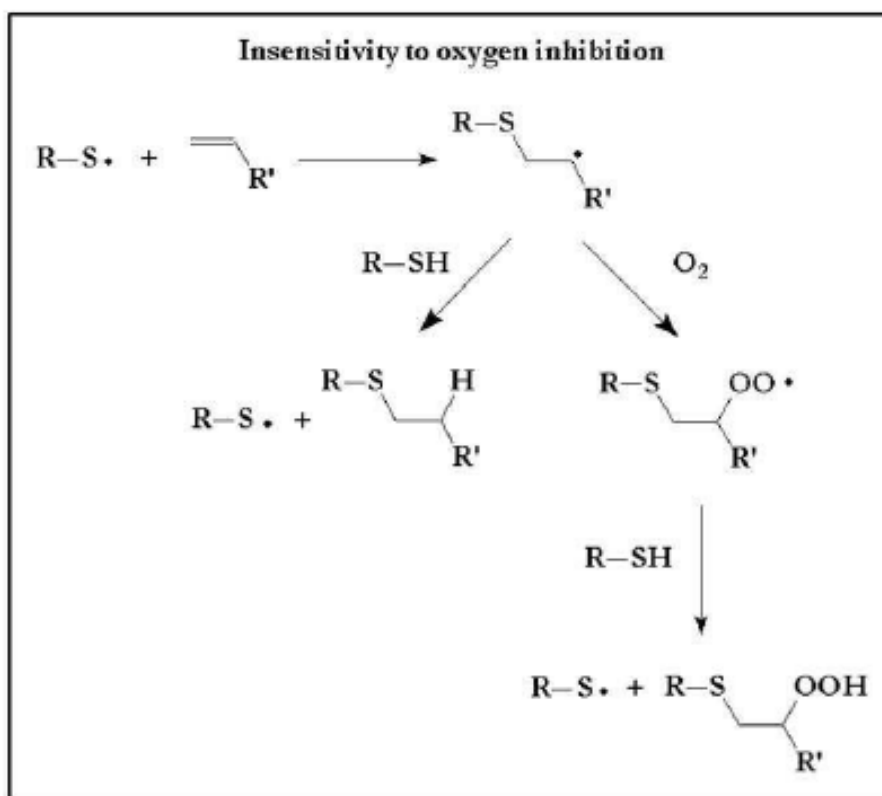


Figure 3.12: Oxygen scavenging mechanism for thiol-ene free radical polymerization.

Another unique advantage of thiol-ene systems is that the polymerization proceeds steadily with the addition of much less amount of photoinitiator than traditional photocuring systems. It is even polymerizable in absence of photoinitiator. In order to counteract the oxygen inhibition effect and raise the curing speed and conversion, the addition of excessive amount of photoinitiator

is a routine solution in non-thiol photopolymerization systems. However, the relatively high content of photoinitiator with small molecular weight not only increases the product cost but also results in some problems of cured materials. The presence of non-reacted photoinitiator will lead to yellowing effect of the photocured materials under daylight exposure. This problem can be effectively solved in thiol-ene photopolymerization systems. Thus, during long-term use of the photocured products the migration of fragments of photoinitiators may cause some problems such as irritant volatile, contact stimulative and potential harm for health. However, in the photocurable thiol-ene systems, whereas thiols completely get crosslinked with multifunctional ene monomers, small molecule of photoinitiator is fixed in the polymer network without migration from the UV-cured products [10]. Furthermore, because of the thioether linkage structure formed by thiol-ene free radical addition in polymerization, the thiol-ene based cured products show some unique physical, chemical and mechanical properties. It was reported that due to the presence of the highly flexible thioether linkages, the thiol-ene photocured materials show a significant ability to adhere to a variety of surfaces, including metals; for this reason they can be largely used in many application fields, including coatings for optical fibers, microelectronics, graphic arts and adhesives [13][14][15][31].

3.2.3 Huisgen 1,3-dipolar cycloaddition

Representing a set of Cu-catalyzed azide-alkyne “click chemistry”, Huisgen 1,3-dipolar cycloaddition was developed to make conjugations between bioactive surfaces easier and less harsh to biomolecules ligands [32][33]. Firstly, azide and alkyne reactive groups are highly specific for one another, and unreactive with most functional groups, ensuring specific conjugation at the desired location(s) on the reactive moiety. Secondly, the formed bonds are highly stable. This is in contrast to amide bonds, which can be cleaved by hydrolysis reactions, and disulfide linkages that are susceptible to cleavage under reducing environments. Thirdly the formed linkages are extremely rigid, which helps to maintain conformation of reacted moieties at the NPs surface

and prevents their cross interactions. Combined, these features enable the production of highly oriented linkages engineered to ensure optimal reaction activity and efficiency. This technique appears to be specially suited for attachment of targeting moieties where orientation and stability of linkages are particularly important. As such this chemistry has been implemented and proved to be effective at binding targeting biomolecules to the NPs surface with >90% efficiency under mild reaction conditions and reaction times of 5-8 hours [34][35][36].

The basic process of the Huisgen 1,3-dipolar cycloaddition [37][38][39] is depicted in Figure 3.13, generating 1,4- and 1,5-triazoles, respectively.

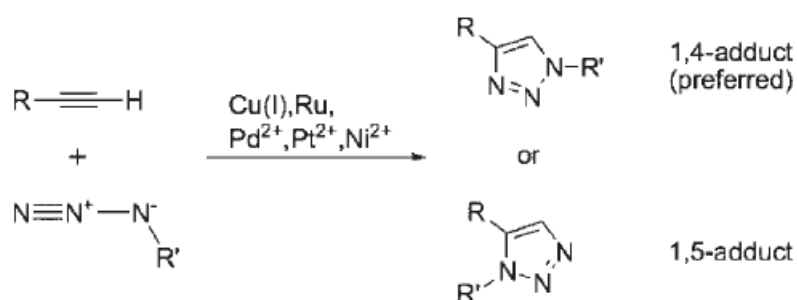


Figure 3.13: Schematic representation of the Huisgen 1,3-dipolar cycloaddition

Nearly all functional groups are compatible with this process, except those that are (i) self reactive, or (ii) able to yield stable complexes with the Cu^I metal under catalyst deactivation.

Double bonds are tolerated to a certain extent given that they are neither electronically activated (i.e., by electron withdrawing substituents) nor embedded into substrates of appropriate ring strain [37]. Thus the reactivity of phenylacetylene with phenylazide (reaction rate $k = 0.29 \times 10^7 \text{ dm}^3 \cdot \text{M}^{-1} \cdot \text{s}^{-1}$) is comparable to that of hept-1-ene, styrene, and isoprene. Other alkenes display faster reactions with phenylazide (e.g., norbornene: $k = 188 \times 10^7 \text{ dm}^3 \cdot \text{M}^{-1} \cdot \text{s}^{-1}$, *N*-phenyl maleimide: $k = 27.60 \times 10^7 \text{ dm}^3 \cdot \text{M}^{-1} \cdot \text{s}^{-1}$, and acetylene carbonic acid dimethyl ester: $k = 25.4 \times 10^7 \text{ dm}^3 \cdot \text{M}^{-1} \cdot \text{s}^{-1}$). Therefore, the reaction with strained and electronically activated alkenes represents an important competitive reaction partner in the thermal process. Similar reasoning is also applicable for the rate-accelerating effect of electron withdrawing substituents

on the azido-molecules as determined by Hammett correlations [40].

A variety of catalytic systems have been used to effect the 1,3-dipolar cycloaddition process. In case of the azide/ acetylene process, mostly Cu^I catalysts have been used and require about 0.25-2 mol.% of the catalysts. Most methods use Cu^I salts directly, other methods generate the copper(I) species by reduction of Cu^{II} salts using sodium ascorbate or metallic copper. Recently, the use of copper clusters of Cu/Cu oxide nanoparticles, sized 7-10 nm [41], as well as copper clusters of diameter around 2 nm, with a specific surface area of 168 m².g⁻¹ [42] have been described, although with contradicting explanations for their catalytic activity. Whereas in the former case the presence of Cu^I/Cu^{II} species in a ration of 1:3 was made responsible for the strong catalytic activity of the Cu⁰ species. Both publications claim a positive influence of the alkylamine ligand present on the nanoparticle surface as an additional factor for activity enhancement. Besides the copper catalyst, 1-5 equivalents of base are added, mechanistically for promoting the formation of the copper(I)-acetylide.

Most of the known solvents can be used for this reaction, in addition, biphasic reaction systems (water/ alcohol or water/ toluene) can be applied with excellent results.

The bases used are mostly triethylamine, 2,6-lutidine, and *N,N*-diisopropylethylamine (DIPEA), as well as *N,N,N', N',N''*-pentamethylethylenetetramine (PMDETA) or 2,2'-bipyridine. Besides the copper catalyst and the base, triazoles have been shown to accelerate the reaction [43]. Some of the ligands are indicative of a complexation of the copper(I), which leads to a stabilization of the copper(I) oxidation state, thus prevents coupling reactions such as the Ulman [44], and Cadiot-Chodkiewicz couplings [45]. Moreover, tris-triazolyl ligands inhibit the Cu^{II}-catalyzed oxidative coupling reactions of terminal alkynes to diynes under otherwise standard conditions [46]. Other systems use tris(carboxyethyl)phosphine (TCPE) as a ligand.

Strong effects of alternative synthetic methodologies have been observed within the click reaction. Thus, Fokin and co-workers [47] and others [48] have

investigated the reaction under action of microwave irradiation. They used a combination of nucleophilic displacements starting from benzylic halides and sodium azide directly linking the present phenylacetylene in a single step. The reaction was strongly enhanced by the action of microwave irradiation, and furnished the corresponding triazoles in yields between 86-93 %. Similar observations have been described with click reactions on polymers and dendrimers. Another approach [49] starts from the initial observation that ammonium salts can act as co-catalysts for the 1,3-dipolar cycloaddition process when using solely metallic copper as the catalyst. Thus, ammonium salts directly promote the formation of Cu^{I} species, which enable an efficient reaction and enhance the cycloaddition products to > 95% yields.

A mechanistic picture of the copper catalyzed reaction was first proposed by Medal and co-workers [50] and Sharpless and co-workers [51] and has later been verified by computational methods [52][53]. However, the proposed catalytic mechanism (calculated [52] by density functional theory (DTF) calculations) that relied on the initial formation of a Cu acetylide between the Cu^{I} species and the terminal alkyne which subsequently proceeded by an initial π -complex formation between the Cu^{I} and the alkyne [54][55], to lead to a lowering of the $\text{p}K_a$ of the terminal acetylene by up to 9.8 units, thus enabling the attack onto the C-H bond, especially in aqueous systems, has been recently revised [56] in favor of a binuclear mechanism as shown in Figure 3.14.

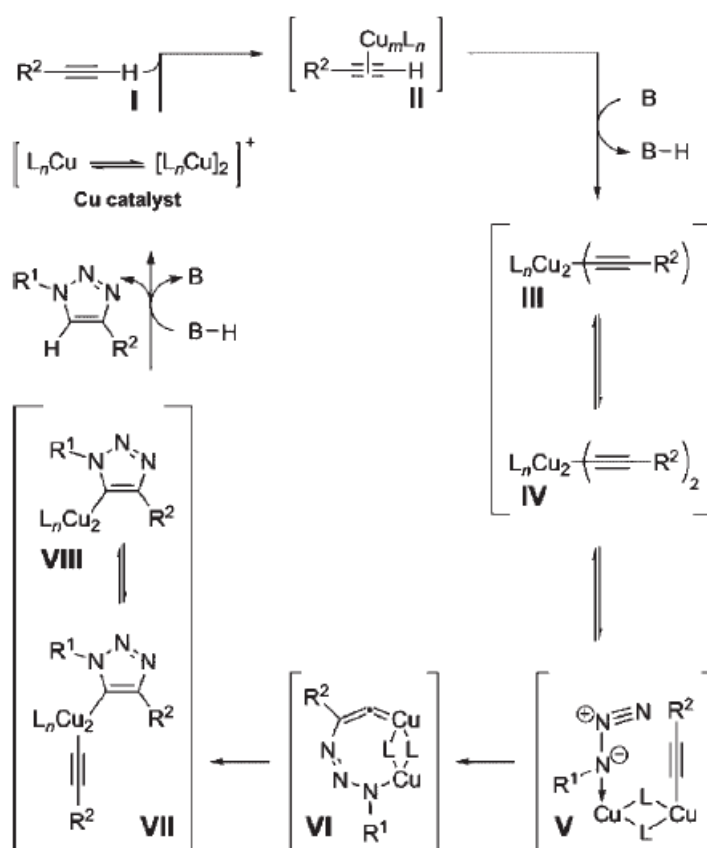


Figure 3.14: schematic representation of the copper catalyzed reaction

Support for this hypothesis, which is similar to the monometallic mechanism proposed by Sharpless and co-workers [52][53] by calculation, is based on the observation that the rate of catalysis is second order with respect to copper, but with increasing concentration of copper, less reactive species are observed [57]. Thus, both the high regioselectivity and the rate acceleration are accounted for by this mechanism. Similar results are obtained when calculating the Cu^I -catalyzed cycloaddition reaction of azides to nitrile-oxides, for which a similar rate enhancement of the copper catalyzed reaction, in confrontation to the purely thermal reaction, was observed.

Since many known polymerization reactions in macro-molecular chemistry require the absence of specific functional groups, there is considerable interest in the fixation of ligands onto polymers and gels after a successful polymerization reaction has been conducted. This is most important when living polymerization mechanisms are used, since especially the highly

sophisticated chemical mechanisms and equilibria of (quasi-) living polymerization reactions are often highly substrate specific and, therefore, strongly affected by even small amounts of functional groups, or the respective coupling agents required for affixation. Another issue concerns the binding of large numbers of ligands onto polymers (i.e., sidechain modified polymers) or dendrimers, which require highly efficient coupling reactions to this purpose as well. Further interest is directed towards the heterogeneous functionalization of polymers in solvent mixtures. Because of the limited solubility of many polymers reactants, post-functionalization reactions cannot always be applied in homogeneous solution with the derivatized polymer. In these cases, highly efficient reactions acting in heterogeneous reaction media are desired. Thus, the Huisgen 1,3-dipolar cycloaddition has been brought into the limelight recently because of its efficiency, often reaching yields of > 99% irrespective of the ligand structure, even in inhomogeneous reaction systems.

This click reaction is also particularly adapted for the ligation of artificial ligands to biomolecules since this reaction work under conditions in which the structural integrity of peptides, proteins, carbohydrates, and assemblies derived from these is preserved. Thus, besides conventional linking methods (e.g., disulfide exchange, amide linkage, reductive aminations, Staudinger-type ligation) [58], this method definitely is an important contribution for biological labeling.

One of the first example to demonstrate the practicability of the azide/alkyne click reaction was provided by Meldal and co-workers [60] who used the click reaction on peptides during solid-phase synthesis. Based upon this knowledge, Ghadiri and co-workers [61] used the click reaction to generate cyclic peptides. An impressive example of the completeness and versatility of the azide/alkyne click reaction has been presented by Finn and co-workers [62] upon modifying all sixty positions of the tobacco mosaic virus. After the generation of a virus-derivative displaying sixty azido, or acetylenic bonds, the final coupling with a rhodamine B dye yields the attachment of sixty moieties onto the surface of the labeled virus. The catalyst system used was based on $\text{Cu}^{\text{II}}\text{SO}_4/\text{tris}(\text{carboxyethyl})\text{ phosphine (TCEP)}/\text{catalyst}/\text{Cu}^0$. Both systems

yielded an attachment efficiency of 100% in a solvent system based on phosphate buffer (plus 5% *t*-butyl alcohol) at a pH of 8.0.

The biolabeling in living systems was demonstrated by Tirell and co-workers [63] by incorporating the unnatural amino-acids azido-alanine, azidohomoalanine, azidovaline, and azidonorleucine into living cells. Reporting and quantification of the incorporation was subsequently done by “clicking” an acetylene-modified biotin ligand onto the surface of E-coli bacteria, which displayed the azido moieties. Ultrapure Cu^IBr (purity 99,999%) was found to be superior in catalyzing the click reaction. A related approach to the use of activity based protein profiling (ABPP) has been reported by Cravat and co-workers [64], which relied on ABPP as a chemical proteomic method, which employs active site-directed probes to simultaneously visualize the changes in activity of proteins in a cellular environment [65].

To summarize, the combination of azide/alkyne click chemistry demonstrates a new approach to the profiling of enzymatic active sites as well as the search for new binding structures onto active protein sites. Clearly, an absolutely randomized approach (without knowledge of the enzyme’s active site) as well as an, at least partially directed, approach is viable, to screen dynamic combinatorial libraries. Therefore this method points to the future for studying associative phenomena, possibly also in supramolecular chemistry and material sciences.

3.3 Emulsion polymerization

Emulsion polymerization is a unique chemical process widely used to produce waterborne resins with various colloidal and physicochemical properties. This heterogeneous free radical polymerization process involves emulsification of the relatively hydrophobic monomer in water by an oil-in-water emulsifier, followed by the initiation reaction with either a water-insoluble initiator (e.g., sodium persulfate (NaPS)) or an oil-soluble initiator (e.g., 2-2'-azobisisobutyronitrile (AIBN)) [66][67][68][69][70][71]. Typical monomers used in emulsion polymerization include butadiene, styrene, acrylonitrile, acrylate ester monomers, vinyl acetate, and vinyl chloride. An extremely large

oil-water interfacial area is generated as the particles nuclei form and grow in size with the progress of the polymerization. Thus, an effective stabilizer such as ionic and non-ionic surfactants and protective colloid (e.g., hydroxyethyl cellulose and polyvinyl alcohol) which can be physically adsorbed or chemically incorporated onto the particle surface, is required to prevent the interactive latex particles from coagulation. Under the circumstances, satisfactory colloidal stability can be achieved via the electrostatic stabilization mechanism [72], the steric stabilization mechanism [73][74], or both. The environmentally friendly latex product comprise a large population of polymer particles ($\sim 10^1$ - 10^3 nm in diameter) dispersed in the continuous aqueous phase. These emulsion polymers find a wide range of applications such as synthetic rubbers, thermoplastics, coatings, adhesives, binders, rheological modifiers, plastic pigments, standards for the calibration of instruments, immunodiagnosis tests, polymeric supports for the purification of proteins and drug delivery system, etc.

Emulsion polymerization is a rather complex process because nucleation, growth and stabilization of polymer particles are controlled by the free radical polymerization mechanisms in combination with various colloidal phenomena. Perhaps, the most striking feature of emulsion polymerization is the segregation of free radicals among the discrete monomer-swollen polymer particles. This will greatly reduce the probability of bimolecular termination of free radicals and, thereby, result in a faster polymerization rate and polymer with a higher molecular weight. This advantageous characteristic of emulsion polymerization cannot be achieved simultaneously in bulk or solution polymerization. Although the nucleation period is quite short, generation of particle nuclei during the early stage of the polymerization plays a crucial role in determining the final latex particle size and particle distribution and it has also a significant influence on the quality of latex products. The way to effectively control the particle nucleation process represents a very challenging task. Transport of monomer, free radicals and surfactant to the growing particles and partition of these reagents among the continuous aqueous phase, emulsified monomer droplets (monomer reservoir), monomer swollen polymer

particles (primary reaction loci) and oil-water interface are the key factors that govern the particle growth stage. The colloidal properties of latex products are of great importance from both academic and industrial point of view. Some representative properties include the particle size and particle size distribution, particle surface charge density (or zeta potential), particle surface area covered by one stabilizer molecule, conformation of the hydrophilic polymer physically adsorbed or chemically coupled onto the particle surface, type and concentration of functional groups on the particle surface, particle morphology, optical and rheological properties and colloidal stability.

A typical emulsion polymerization formulation comprises monomer, water, surfactant and a water-soluble initiator. The reaction system is characterized by the emulsified monomer droplets ($\sim 1\text{-}10\ \mu\text{m}$ in diameter, $10^{12}\text{-}10^{14}\ \text{dm}^{-3}$) dispersed in the continuous aqueous phase with the help of an oil-in-water surfactant at the very beginning of polymerization. Monomer-swollen micelles ($\sim 5\text{-}10\ \text{nm}$ in diameter, $10^9\text{-}10^{21}\ \text{dm}^{-3}$ in number) may also exist in the reaction system, provided that the concentration of surfactant in the aqueous phase is above its critical micelle concentration (CMC). Only a small fraction of the relatively hydrophobic monomer is present in the micelles (if present) or dissolved in the aqueous phase. Most of the monomer molecules dwell in the giant monomer reservoirs (i.e., monomer droplets). The polymerization is initiated by the addition of initiator. According to the micelle nucleation model proposed by Harkins [75][76][77] and Smith and Ewart [78][79][80] and modified by Gardon [81][82], submicron latex particles ($\sim 0.05\text{-}1\ \mu\text{m}$ in diameter, $10^{16}\text{-}10^{18}\ \text{dm}^{-3}$ in number) are generated via the capture of free radicals by micelles, which exhibit an extremely large oil-water interfacial area. In general, monomer droplets are not effective in competing with micelles in capturing free radicals generated in the aqueous phase due to their relatively small surface area. However, monomer droplets may become the predominant particle nucleation loci if the droplet size is reduced to submicron range. This technique is called miniemulsion polymerization [83][84][85][86][87] and innovative miniemulsion polymerization technology is still being investigated

[86].

Waterborne free radicals first polymerize with monomer molecules dissolved in the continuous aqueous phase. This would result in the increased hydrophobicity of oligomeric radicals. When a critical chain length is achieved, these oligomeric radicals become so hydrophobic that they show a strong tendency to enter the monomer-swollen micelles and then continue to propagate by reacting with those monomer molecules therein, as illustrated in Figure 3.15.

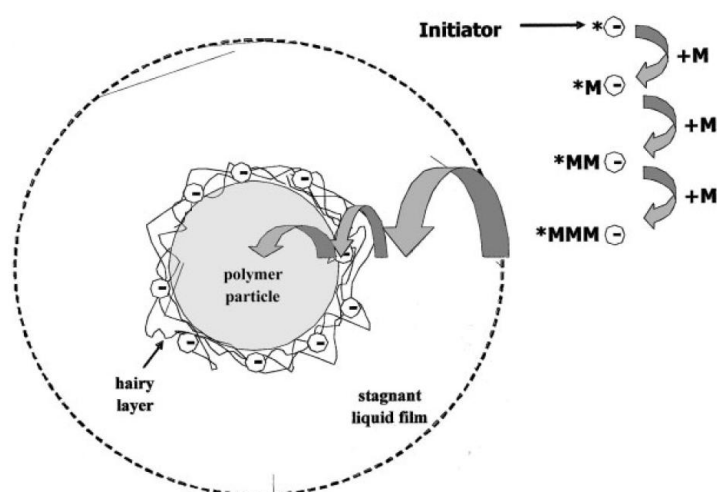


Figure 3.15: mechanism for radical entry [88]

As a consequence, monomer-swollen micelles are successfully transformed into particle nuclei. These precursor particles continue to grow by acquiring the reactant species from monomer droplets and monomer-swollen micelles. In order to maintain adequate colloidal stability of the growing particle nuclei, micelles that do not contribute to particle nucleation disband to supply the increasing demand for surfactant. In addition, the surfactant molecules adsorbed on monomer droplets may also desorb out of the droplet surface, diffuse across the continuous aqueous phase and then adsorb on the expanding particle surface. The particle nucleation stage ends immediately after the exhaustion of micelles. About one of every 10^2 - 10^3 micelles can be successfully converted into latex particles.

The Smith-Ewart theory predicts that the number of latex particles nucleated per unit volume of water (N_p) is proportional to the surfactant concentration

and initiator concentration to the 0.6 and 0.4 powers respectively. This relationship shows that the most important parameter that controls the particle nucleation process is the surfactant concentration. Although the particle nucleation period is relatively short (up to about 10-20% monomer conversion), it controls the particle size and particle size distribution of latex products. The application properties of emulsion polymers such as rheology and film formation are strongly dependent on the particle size and particle size distribution. By rule of thumb, latex products with a large particle size can be produced by using a relatively low surfactant concentration in the particle nucleation stage. In addition, a narrow particle size distribution will be achieved. This is simply because the shorter the particle nucleation period (i.e., the lower the surfactant concentration), the narrower the resultant particle size distribution. It should be noted that flocculation of particle nuclei arising from inadequate stabilization of the colloidal system may also take place during polymerization. This will make the task of controlling the particle size and particle size distribution of latex products more difficult. In addition, it is much easier to prepare latex products with high total solid contents when a small population of particles with a large particle size is produced at the end of polymerization. This is closely related to the relatively mean free path length (H/r) between two interactive particles as a function of the total solid content [89]. H and r represent the average interparticle distance and particle radius respectively. The value of H/r decreases with increasing total solid content. Thus, the higher the total solid content, the more crowded the colloidal system (i.e. the greater the interaction between two approaching particles). Furthermore, larger particles exhibit larger value of H for the stationary particle packing. Thus, at constant total solid content, the colloid system comprising larger particles should be less crowded. In this manner, high solid latex products with satisfactory rheological properties are achieved. This is a very important consideration in many industrial applications.

After the particle nucleation process is completed, the number of latex particles (i.e. reaction loci) per unit volume of water remains relatively constant toward the end of polymerization. The propagation reaction of free radicals with

monomer molecules takes place primarily in monomer-swollen particles. Monomer droplets only serve as reservoirs to supply the growing particles with monomer and surfactant species. The majority of monomer is consumed in this particle growth stage ranging from ~10-20 to 60% monomer conversion. The particle growth stage ends when monomer droplets disappear in the polymerization system. Smith-Ewart case 2 kinetics has been widely used to calculate the rate of polymerization (R_p)

$$R_p = k_p[M]_p(nN_p/N_A)$$

where k_p is the propagation constant, $[M]_p$ the concentration of monomer in the particles, n the average number of free radicals per particle, and N_A the Avogadro number. This kinetic model was developed based on the following assumptions:

1. Nucleation and coagulation of particles do not occur and the number of particle per unit volume of water remains constant during polymerization
2. The particle size distribution is relatively monodisperse.
3. Desorption of free radicals out of the particles does not take place
4. Bimolecular termination of the polymeric radical inside the particle upon the entry of an oligomeric radical from the aqueous phase is instantaneous.

These assumptions then lead to a scenario that, at any moment, monomer-swollen particles contain either only one free radical (active) or zero free radical (idle). Under the circumstances, a value of n equal to 0.5 is achieved for the polymerization systems that follow Smith-Ewart case 2 kinetics. In addition, the concentration of monomer in the particles does not vary to any extent with the progress of polymerization in the presence of monomer droplets. As a result, a steady polymerization rate is attained during the second phase. Furthermore, the polymerization kinetics is strictly controlled by the population of particles available for consuming monomer. Smith-Ewart case 2 kinetics has been successfully applied to emulsion polymerizations of relatively water-insoluble monomers such as styrene and butadiene.

Emulsion polymerization proceeds from the second phase to the third phase

when all the monomer droplets disappear. In phase III, latex particles become monomer starved and the concentration of monomer in the reaction loci continues to decrease toward the end of polymerization. Thus, the steady polymerization rate observed in phase II cannot be maintained anymore and the polymerization rate decreases during phase III. On the other hand, the polymerization rate may increase rapidly with increasing monomer conversion. This is attributed to the greatly reduced bimolecular termination reaction between two polymeric radicals within the very viscous particle; hence, polymerization is carried out at a temperature below the glass transition of the monomer-starved polymer solution. This phenomenon is called the gel effect [90][91]. To minimize residual monomer in latex products is essential for the successful product development because of the potential hazard to end-users. The rate of polymerization as a function of monomer conversion and schematic representation of the micelle nucleation model are shown in Figure 3.16 and Figure 3.17 [92].

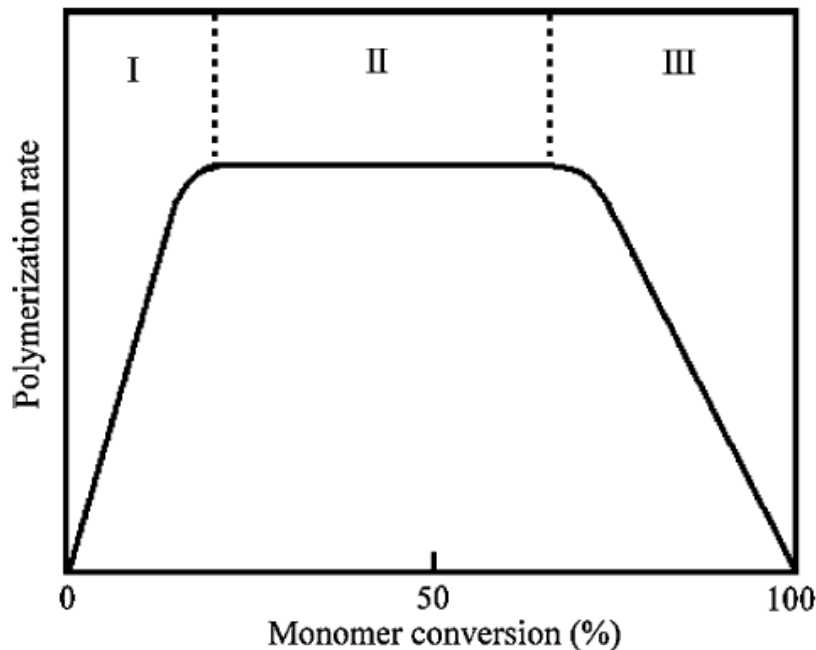
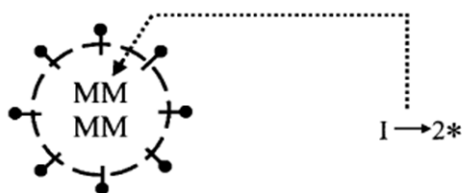
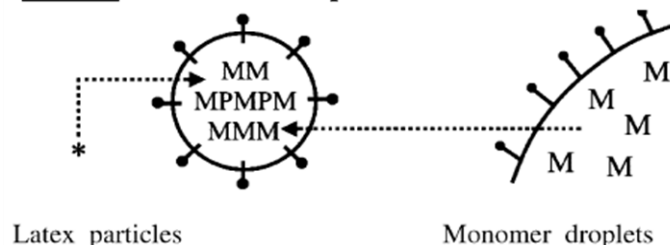


Figure 3.16: rate of polymerization as a function of monomer conversion

Phase I: Nucleation of monomer-swollen micelles



Phase II: Growth of latex particles



Phase III: Consumption of residual monomer

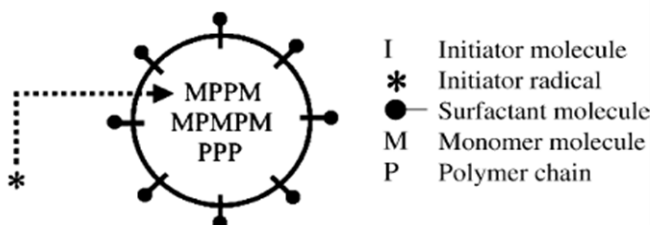


Figure 3.17: schematic representation of the micelle nucleation model

References

- [1] C. Decker, *Handbook of Polymer Science and Technology*, **1989**, 3, 541-608.
- [2] K. Studer, C. Decker, E. Beck, R. Schwalm, *Progr. Org. Coat.*, **2003**, 48, 92-100.
- [3] I. Roppolo, *UV-cured photoluminescent coatings: acrylic and epoxy systems*, PhD Thesis, **2012**.
- [4] W.H. Binder, R. Sachsenhofer, *Macromol. Rapid. Commun.*, **2007**, 28, 15-24.
- [5] J.A. Johnson, M.G. Finn, J.T. Koberstein, N.J. Turro, *Macromol. Rapid Commun.*, **2008**, 29, 1052-1072.

- [6] G. von Maltzahn, Y. Ren, J.H. Park, D.H. Min, V.R. Kotamraju, J. Jayakumar, V. Fogal, M.J. Sailor, E. Ruoslahti, S.N. Bhatia, *Bioconjugate Chem.*, **2008**, 19, 1570-1578.
- [7] C. Hoyle, T.Y. Lee, T. Roper, *J. Polym. Sci. Part A: Polym Chem*, **2004**, 42, 5301-5338.
- [8] N.B. Cramer, C.N. Bowman, *J. Polym. Sci. Polym. Chem.*, **2001**, 39, 3311-3319.
- [9] J.A. Carioscia, H. Lu, J.W. Stansbury, C.N. Bowman, *Dental Materials*, **2005**, 21, 1137-1143.
- [10] T. Posner, *Chem Ber*, **1905**, 38, 646-657.
- [11] C. Hoyle, T.Y. Lee, T. Roper, *J. Polym. Sci. Part A: Polym Chem*, **2004**, 42, 5301-5338.
- [12] N.B. Cramer, J.P. Scott, C.N. Bowman, *Macromolecules*, **2002**, 35, 5361-5365.
- [13] A.F. Jacobine, *In Radiation Curing in Polymer Science and Technology III: Polymerization Mechanisms*, J.D. Fouassier, J.F. Rabek, Eds. Elsevier: London, **1993**, 219-268.
- [14] J.G. Woods, *Radiation Curable Adhesives in Radiation Curing: Science and Technology*, S.P. Pappas, Ed. Plenum Press, New York, 333 (**1992**).
- [15] C. Hoyle, T. Clark, T.Y. Lee, T. Roper, B. Pan, H. Wei, H. Zhou, J. Lichtenhan, *RadTech Eur Tech Conf Proc* **2005**.
- [16] T.M. Roper, T. Kwee, T.Y. Lee, C.A. Guymon, C.E. Hoyle, *Polymer*, **2004**, 45, 2921-2929.
- [17] S.K. Reddy, N.B. Cramer, T. Cross, R. Raj, C.N. Bowman, *Chem. Mater.*, **2003**, 15 (22), 4257-4261.
- [18] J.D. Fouassier, J.F. Rabek, , *Eds. Elsevier Applied Science: London*, **1993**, 3, 219.
- [19] M.J. Kade, D.J. Burke, C.J. Hawker, *Polym. Chem.*, **2010**, 48, 743-750.
- [20] C.E. Hoyle, C.N. Bowman, *Angew. Chem. Int. Ed.*, **2010**, 49, 1540-1573.

- [21] N.B. Cramer, C.L. Couch, K.M. Schreck, J.A. Carioscia, J.E. Boulden, J.W. Stansbury, C.N. Bowman, *Dental Materials*, **2010**, 26, 21-28.
- [22] Q. Li, H. Zhou, C. Hoyle, *Polymer*, **2009**, 50, 2237-2245.
- [23] C. Decker, T. Nguyen T. Viet, *Polymer*, **2000**, 41, 3905-3912.
- [24] H. Lu, J.A. Carioscia, J.W. Stansbury, C.N. Bowman, *Dental Materials*, **2005**, 21, 1129-1136.
- [25] J.A. Carioscia, H. Lu, J.W. Stansbury, C.N. Bowman, *Dental Materials*, **2005**, 21, 1137-1143.
- [26] V.S. Khire, D.S. W. Benoit, K.S. Anseth, C.N. Bowman, *J. Polym. Sci. Part A: Polym. Chem.*, **2006**, 44, 7027-7039.
- [27] A.J. Guenther, D.M. Hess, J.J. Cash, *Polymer*, **2008**, 49, 5533-5540.
- [28] L. Lecamp, F. Houllier, B. Youssef, C. Bunel, *Polymer*, **2001**, 42, 2727-2736.
- [29] C.N. Bowman, *RadTech Eur Tech Conf Proc*, **2005**.
- [30] N. Arsu, I. Reetz, Y. Yagci, M.K. Mishra, *Handbook of Vinyl Polymers: Radical Polymerization and Technology*, **2007**, 8, 141-204.
- [31] G. Colucci, *Hybrid Thiol-Ene Photocured Nanostructures Materials*, PhD Thesis, **2011**.
- [32] J.F. Lutz, Z. Zarafshani, *Advanced Drug Delivery Reviews*, **2008**, 60, 958-970.
- [33] C.D. Hein, X.M. Liu, D. Wang, *Pharmaceutical Research*, **2008**, 25, 2216-2230.
- [34] G. von Maltzahn, Y. Ren, J.H. Park, D.H. Min, V.R. Kotamraju, J. Jayakumar, V. Fogal, M.J. Sailor, E. Ruoslahti, S.N. Bhatia, *Bioconjugate Chemistry*, **2008**, 19, 1570-1578.
- [35] E.Y. Sun, L. Josephson, R. Weissleder, *Molecular Imaging*, **2006**, 5, 122-128.
- [36] O. Veisoh, J. Gunn, M. Zhang, *Adv. Drug. Deliv. Rev.*, **2010**, 62, 284-304.
- [37] R. Huisgen, G. Szeimies, L. Möbius, *Chem. Ber.*, **1967**, 100, 2494-2507.

- [38] R. Huisgen, *Pure Appl. Chem.*, **1989**, 61, 613-662.
- [39] K.V. Gothelf, K. A. Jorgensen, *Chem. Rev.*, **1998**, 98, 863-909.
- [40] P. Scheiner, J.H. Schomaker, S. Deming, W.J. Libbey, G.P. Nowack, *J. Am. Chem. Soc.*, **1965**, 87, 306-311.
- [41] G. Molteni, C.L. Bianchi, G. Marinoni, N. Santo, A. Ponti, *New. J. Chem.*, **2006**, 30, 1137-1139.
- [42] L.D. Pachon, J.H. van Maarseveen, G. Rothenberg, *Adv. Synth. Catal.*, **2005**, 347, 811-815.
- [43] T.R. Chan, R. Hilgraf, K.B. Sharpless, V.V. Fokin, *Org. Lett.*, **2004**, 6, 2853-2855.
- [44] F. Ullman, *Liebigs Ann. Chem.*, **1904**, 332, 38.
- [45] P. Cadiot, W. Chodkiewicz, *Chemistry of Acetylenes*, H.G. Viehe, Ed., Dekker, New York: **1969**, 597-647.
- [46] I.D. Campbell, G. Eglinton, *Org. Synth.*, **1965**, 45, 39.
- [47] P. Appakkuttan, W. Dehaen, V.V. Fokin, E. van der Eyken, *Org. Lett.*, **2004**, 6, 4223.
- [48] P. Lidström, J. Tierny, B. Wathey, J. Westman, *Tetrahedron*, **2001**, 57, 9225-9283.
- [49] H.A. Orgueira, D. Fokas, Y. Isome, P. Chan, C. M. Baldino, *Tetrahedron*, **2005**, 46, 2911-2914.
- [50] C.W. Tornøe, C. Christensen, M. Meldal, *J. Org. Chem.*, **2002**, 67, 3057-3064.
- [51] V.V. Rostovtsev, L.G. Green, V. Fokin, K.B. Sharpless, *Angew. Chem. Int. Ed.*, **2002**, 41, 2596-2599.
- [52] F. Himo, T. Lovell, R. Hilgraf, V.V. Rostovtsev, L. Noodleman, K.B. Sharpless, V.V. Fokin, *J. Am. Chem. Soc.*, **2005**, 127, 210-216.
- [53] F. Himo, Z.P. Demko, L. Noodleman, K.B. Sharpless, *J. Am. Chem. Soc.*, **2002**, 124, 12210-12216.
- [54] C. Koradin, K. Polborn, P. Knochel, *Angew. Chem. Int. Ed.*, **2002**, 41, 2535-2538.
- [55] M. Kinugasa, S. Hashimoto, *J. Chem. Soc. Chem. Commun.*, **1972**, 466-467.

- [56] V.D. Bock, H. Heimsha, S.H. van Morsteen, *Eur. J. Org. Chem.*, **2006**, 51-68.
- [57] G. Molteni, A. Ponti, *Chem. Eur. J.*, **2003**, 9, 2770-2774.
- [58] D.S.Y. Yeo, R. Srinivasan, G.J.Y. Chen, S.Q. Yao, *Chem. Eur. J.*, **2004**, 10, 4664-4672.
- [59] V. Ladmiral, G. Mantovani, G.J. Clarkson, S. Cauet, J.L. Irwin, D.M. Haddleton, *J. Am. Chem. Soc.*, **2006**, 4823-4830.
- [60] C.W. Tornøe, C. Christensen, M. Meldal, *J. Org. Chem.*, **2002**, 67, 3057-3064.
- [61] W.S. Horne, M.K. Yadaf, D. Stout, M.R. Ghadiri, *J. Am. Chem. Soc.*, **2004**, 126, 15366-15367.
- [62] Q. Wang, T.R. Chan, R. Hilgraf, V.V. Fokin, K.B. Sharpless, M.G. Finn, *J. Am. Chem. Soc.*, **2003**, 125, 3192-3193.
- [63] A.J. Link, M.K.S. Vink, D.A. Tirrell, *J. Am. Chem. Soc.*, **2004**, 126, 10598-10602.
- [64] A.E. Speers, G.C. Adam, B.F. Cravatt, *J. Am. Chem. Soc.*, **2003**, 125, 4686-4687.
- [65] B.F. Cravatt, E.J. Sorensen, *Curr. Opin. Chem. Biol.*, **2000**, 4, 663-668.
- [66] F.A. Bovey, I.M. Kolthoff, A.I. Medalia, E.J. Meehan, *Emulsion polymerization*. New York: Interscience Publishers, **1965**.
- [67] D.C. Blakely, *Emulsion polymerization. Theory and practice*. London: Applied Science, **1975**.
- [68] V.I. Eliseeva, S.S. Ivanchev, S.I. Kuchanov, A.V. Lebedev, *Emulsion polymerization and its applications in industry*. New York: Consultants Bureau, **1981**.
- [69] J. Barton, I. Capek, *Radical polymerization in disperse systems*. New York: Ellis Horwood, **1994**.
- [70] R.G. Gilbert, *Emulsion polymerization: a mechanistic approach*. London: Academic Press, **1995**.
- [71] R.M. Fitch, *Polymer colloids: a comprehensive introduction*. London: Academic Press, **1997**.

- [72] E.J.W. Verwey, J.T.G. Overbeek, *Theory of the stability of lyophobic colloids*. New York: Elsevier, **1943**.
- [73] T. Sato, R. Ruch, *Stabilization of colloidal dispersions by polymer adsorption*. New York, NY, **1980**.
- [74] D.H. Napper, *Polymeric stabilization of colloidal dispersions*. London: Academic Press, **1983**.
- [75] W.D. Harkins, *J. Chem. Phys.*, **1945**, 13, 381–382.
- [76] W.D. Harkins, *J. Chem. Phys.*, **1946**, 14, 47-48.
- [77] W.D. Harkins, *J. Am. Chem. Soc.*, **1947**, 69, 1428-1444.
- [78] W.V. Smith, R.H. Ewart, *J. Chem. Phys.*, **1948**, 16, 592-599.
- [79] W.V. Smith, *J. Am. Chem. Soc.*, **1948**, 70, 3695-3702.
- [80] W.V. Smith, *J. Am. Chem. Soc.*, **1949**, 71, 4077-4082.
- [81] J.L. Gardon, *J. Polym. Sci. A*, **1968**, 6, 623-641.
- [82] J.L. Gardon, *J. Polym. Sci. A*, **1968**, 6, 643-664.
- [83] M.S. El-Aasser, C.M. Miller, *Preparation of latexes using miniemulsions*. In: Asua JM, editor. *Polymeric dispersions. Principles and applications*. Dordrecht: Kluwer, **1997**, 109-26.
- [84] E.D. Sudol, M.S. El-Aasser, *Miniemulsion polymerization*. In: Lovell PA, El-Aasser MS, editors. *Emulsion polymerization and emulsion polymers*. Chichester: Wiley, **1997**, 699-722.
- [85] I. Capek, C.S. Chern, *Adv. Polym. Sci.*, **2001**, 155, 101-165.
- [86] M. Antonietti, K. Landfester, *Prog. Polym. Sci.*, **2002**, 27, 689-757.
- [87] J.M. Asua, *Prog. Polym. Sci.*, **2002**, 27, 1283-1346.
- [88] J.M. Asua, *J. Polym. Sci. Part A: Polym. Chem.*, **2004**, 42, 1025-1041.
- [89] C.S. Chern, H. Hsu, F.Y. Lin, *J. Appl. Polym. Sci.*, **1996**, 60, 1301-1311.
- [90] N. Friis, A.E. Hamielec, *Gel-effect in emulsion polymerization of vinyl monomers*. In: Piirma I, Gardon JL, editors. *ACS symposium series no. 24*, Washington, DC, **1976**, 82-91.
- [91] G.T. Russell, R.G. Gilbert, D.H. Napper, *Macromolecules*, **1992**, 25, 2459-2469.
- [92] C.S. Chern, *Prog. Polym. Sci.*, **2006**, 31, 443-486.

4. Materials and Methods

4.1 PEG coated magnetite nanoparticles via photopolymerization

In this part we report a new fast and convenient method for preparing magnetic nanoparticles with a Fe_3O_4 core and a Poly(ethylene glycol)-diacrylate shell in water. We used a reduction coprecipitation method to obtain Fe_3O_4 in aqueous solution [1][2] whereas the PEGDA coating was obtained via photochemical reaction at room temperature in an initiator free aqueous system. The fact that this method is solvent free and initiator free makes it ideal for biomedical applications.

4.1.1 Materials

$\text{FeCl}_3 \cdot 6\text{H}_2\text{O}$ (97%, Sigma-Aldrich), Sodium sulfite (Na_2SO_3) ($\geq 98\%$, Sigma-Aldrich), Ammonia (25%, Merck) and Poly(ethylene glycol) diacrylate (PEGDA) ($M_n = 575$, Aldrich) were used as received.

4.1.2 Synthesis of Fe_3O_4 nanoparticles

Magnetite nanoparticles were synthesized by a chemical co-precipitation of Fe^{2+} and Fe^{3+} ions under alkaline conditions, as already reported in literature [3]. As a typical procedure 3,25 g of $\text{FeCl}_3 \cdot 6\text{H}_2\text{O}$ was dissolved into 100 ml of distilled water. The solution was added into a three-necked flask together with 5 ml of Na_2SO_3 solution at 5 wt%. Subsequently 25 ml of concentrated ammonia were diluted into 40 mL of distilled water and then added into the flask under nitrogen inlet; the solution quickly turned black. The solution was stirred for 30 minutes at 70 °C and then cooled down to room temperature. The black precipitate was separated with a magnet and washed several times with distilled water. The Fe_3O_4 nanoparticles were redispersed in distilled water. The concentration of the Fe_3O_4 nanoparticles was determined by means of TGA to be 5,81 mg/ml. The particles diameter was studied via DLS analysis. The water dispersion of Fe_3O_4 nanoparticles showed superparamagnetic property, as reported in Figure 4.1.

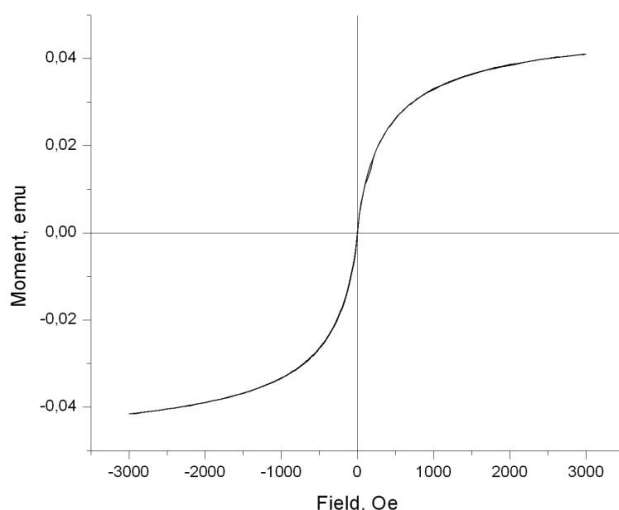


Figure 4.1: Magnetization versus applied magnetic field of synthesized bare Fe₃O₄ particles

4.1.3 Polymeric coating of Fe₃O₄ nanoparticles

The Fe₃O₄ nanoparticles were coated with PEGDA via UV-curing. In a typical procedure 1,72 ml of the aqueous/magnetite dispersion were added to 50 ml of deionized water into a three-necked flask under magnetic stirring and nitrogen inlet. Subsequently 0.168 ml of PEGDA was added dropwise and then the mixture was exposed to UV light for 20 minutes. The polymeric coated magnetite nanoparticles were collected with a magnet, washed with distilled water and redispersed into distilled water.

4.1.4 Characterization techniques

Particle sizes and size distribution of both bare Fe₃O₄ and magnetic nanoparticles were measured by using Dynamic Light Scattering (DLS). The DLS measurements were done on a Zetasizer Nanoseries ZS90 (Malvern). The measurement is based on the fact that particles, emulsions and molecules in suspension undergo Brownian motion. This is the motion induced by the bombardment by solvent molecules that themselves are moving due to their thermal energy. If the particles or molecules are illuminated with a laser, the intensity of the scattered light fluctuates at a rate that is dependent upon the

size of the particles as smaller particles are “kicked” further by the solvent molecules and move more rapidly. Analysis of these intensity fluctuations yields the velocity of the Brownian motion and hence the particle size using the Stokes-Einstein relationship. The morphology and the chemical structure of magnetic nanoparticles were further investigated by X-ray Photoelectron Spectroscopy (XPS), and transmission electron microscopy (TEM). Thermogravimetric analyses (TGA) was performed both on bare and coated magnetite nanoparticles.

The XPS analyses were developed with a XPS *VersaProbe5000* instrument with a monochromatic X-ray beam (Al source). In order to survive the polymer characteristic, during the analyses, a 100 μm diameter spot size, an area of 100 μm X 800 μm was employed. A Physical Electronics patent neutralization system, for reduce charging effect on sample, was also used. This neutralization system consists in an electronic ion gun combined with an Argon ion gun for positive and negative charge neutralization.

Thermogravimetric analysis (TGA) was performed with a Mettler TGA/SDTA 851 instrument between 20 and 700 $^{\circ}\text{C}$ at a heating rate of 10 $^{\circ}\text{C}/\text{min}$ in air.

Samples were observed by TEM by examining in a 300 keV transmission electron microscope (TEM) Philips CM30. TEM micrographs were processed with a slow scan CCD camera and analyzed with the Digital Micrograph program. The TEM observations were always performed using a very low electron flux in order to avoid any structural modification of the sample induced by the electron beam.

The magnetic properties of both bare Fe_3O_4 and magnetic nanoparticles were studied by measuring the hysteresis curves at room temperature using a Vibrating Sample Magnetometer (VSM).

Magnetic hysteresis loops were measured at room temperatures on coated magnetite water dispersion by using an alternating-gradient field magnetometer (AGFM) equipped with a liquid He continuous-flux cryostat and operating in the magnetic field range $-3 \text{ kOe} < H < +3 \text{ kOe}$. The diamagnetic contribution of sample holder and substrates were carefully subtracted from the measured

curves. The magnetic field was applied parallel to the film plane.

4.2 PEG coated magnetite nanoparticles via UV-thiol-ene addition reaction

In this part magnetite nanoparticles were coated following a previous surface functionalization. The Fe_3O_4 nanoparticles were obtained by a reduction coprecipitation method and stabilized with citric acid. Afterwards nanoparticles surface was modified by a silanization reaction with vinyltrimethoxysilane involving magnetite hydroxyl groups. Vinyl functionalized nanoparticles were coated with poly (ethylene-glycol) (PEG) using PEG dithiol (PEG-SH) under UV irradiation. Thiol-ene is a free-radical reaction that proceeds by a step-growth mechanism, involving two main steps, a free-radical addition followed by a chain transfer reaction; this reaction is well known for occurring in absence of any radical photoinitiator which make it particularly appropriate for biomedical applications.

4.2.1 Materials

$\text{FeCl}_3 \cdot 6\text{H}_2\text{O}$ (97%, Sigma-Aldrich), Sodium sulfite (Na_2SO_3) ($\geq 98\%$, Sigma-Aldrich), Ammonia (25%, Merck), Citric acid ($\geq 99,5\%$, Sigma-Aldrich), Vinyltrimethoxysilane (VTMS) (98%, Aldrich), Acetic acid concentrated solution (0.1 M, Fluka), Polyethyleneglycol dithiol (PEG-SH) ($M_n \approx 1500$, Aldrich) were used as received.

4.2.2 Synthesis of Fe_3O_4 nanoparticles

Magnetite nanoparticles were synthesized by a chemical co-precipitation of Fe^{2+} and Fe^{3+} ions under alkaline conditions, as already reported in literature [3]. As a typical procedure 3,25 g of $\text{FeCl}_3 \cdot 6\text{H}_2\text{O}$ was dissolved into 100 ml of distilled water. The solution was added into a three-necked flask together with 5 ml of Na_2SO_3 solution at 5 wt %. Subsequently 20 ml of concentrated ammonia were diluted into 40 mL of distilled water and then added into the flask under nitrogen inlet; the solution quickly turned black. The solution was

stirred for 30 minutes at 70 °C. Successively, the temperature solution was raised up to 95 °C and 1 g of citric acid was dissolved into 2 ml of water and added to the solution. After 90 minutes the solution was cooled down to room temperature. The black precipitate was separated with a magnet and washed several time with distilled water. The Fe₃O₄ nanoparticles were redispersed in distilled water. The concentration of the Fe₃O₄ nanoparticles was determined by means of TGA to be 5,81 mg/ml. The particles diameter was studied via DLS analysis. The water dispersion of Fe₃O₄ nanoparticles showed superparamagnetic property, as reported in Figure 4.2.

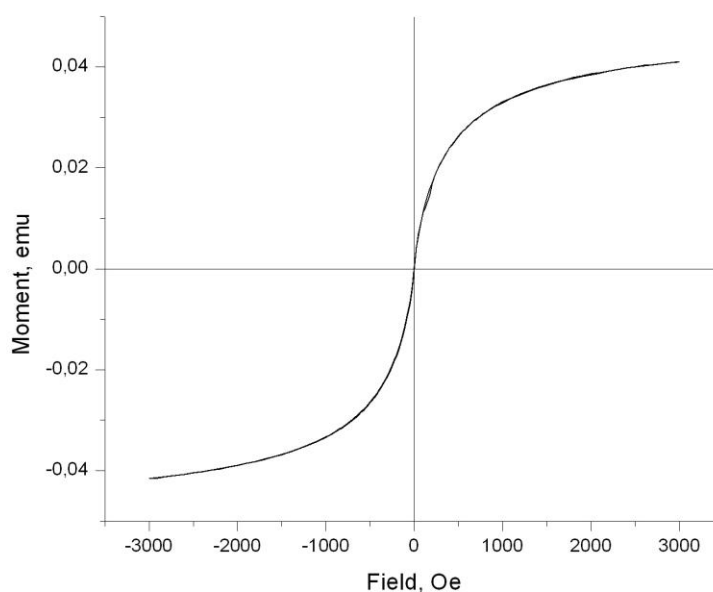


Figure 4.2: Magnetization versus applied magnetic field of synthesized bare Fe₃O₄ particles

4.2.3 Vinyl surface functionalization of magnetite nanoparticles

Vinyl surface functionalization of magnetite nanoparticles was performed by reacting VTMS with the hydroxyl groups present on the Fe₃O₄ surface. Briefly a water/ethanol 1:10 vol/vol solution was put in a flask under magnetic stirring together with 3 ml of acetic acid and 0.478 ml of VTMS, the solution was stirred for 30 minutes at room temperature. The acidic conditions are needed to

hydrolyze the alkoxy-silane groups to silanol groups. Afterwards 5 ml of synthesized Fe_3O_4 aqueous dispersion were added and stirred for 24 hours. A silanol condensation with hydroxyl groups present on the magnetite nanoparticles will allow achieving a vinyl surface functionalization of the magnetite nanoparticles. The magnetite concentration was 14.7 mg/ml, as determined by TGA analyses.

4.2.4 *Polyethyleneglycol coating of vinyl functionalized Fe_3O_4 nanoparticles*

The vinyl functionalized Fe_3O_4 nanoparticles were coated with PEG-SH via UV-curing. In a typical procedure 0,678 ml of the aqueous/vinyl-magnetite dispersion (10 mg of vinyl functionalized magnetite nanoparticles) were added to 60 ml of deionized water into a three-necked flask under magnetic stirring and nitrogen inlet. Subsequently 300 mg of PEG-SH were added dropwise and then the mixture was exposed to UV light for 30 minutes. The polymeric coated magnetite nanoparticles were collected with a magnet, washed with distilled water and redispersed into distilled water.

4.2.5 *Characterization techniques*

Particle sizes and size distribution of both bare and coated Fe_3O_4 nanoparticles were measured using Dynamic Light Scattering (DLS). The DLS measurements were done on a Zetasizer Nanoseries ZS90 (Malvern). The morphology and the chemical structure of magnetic nanoparticles were further investigated by Transmission Electron Microscopy (TEM) in a 300 keV transmission electron microscope (TEM) Philips CM30. TEM micrographs were processed with a slow scan CCD camera and analyzed with the Digital Micrograph program. The TEM observations were always performed using a very low electron flux in order to avoid any structural modification of the sample induced by the electron beam. Thermogravimetric analyses (TGA) was performed both on bare and coated magnetite nanoparticles with a Mettler TGA/SDTA 851 instrument between 20 and 700 °C at a heating rate of 10 °C/min in air. The magnetic properties of both bare Fe_3O_4 and magnetic

nanoparticles were studied by measuring the hysteresis curves at room temperature using a Vibrating Sample Magnetometer (VSM) operating in the magnetic field range $-10 \text{ kOe} < H < +10 \text{ kOe}$. The diamagnetic contribution of sample holder and solvent were significant. A reference measurement was preliminarily done by measuring the magnetic response of the sample holder filled with the same amount of pure solvent (i.e., without the magnetic nanoparticles). The magnetic contribution ascribed to magnetite NPs (before and after functionalization) was obtained from the measured curves by subtracting the reference curve.

4.3 Polymer grafting onto magnetite nanoparticles via click-reaction

In this work we report the use of “click” reactions for preparing magnetic NPs with Fe_3O_4 core and different biocompatible polymeric shells. We used a reduction coprecipitation method to obtain Fe_3O_4 particles in aqueous solution. As a next step, magnetic NPs surface was modified by a silanization reaction with (3-bromopropyl) trimethoxysilane in order to introduce bromine groups on the particles surface. Afterwards the bromine groups were converted to azide groups by the reaction with sodium azide in order to obtain azide groups to take part to click reaction with alkyne-functionalized polymers. For this reason, acetylene functionalized poly(ethylene glycol) (a-PEG) and poly(ϵ -caprolactone) (a-PCL) were synthesized and grafted onto the surface of azide functionalized NPs via “click” reaction to obtain monodisperse magnetic NPs. The peculiar characteristics of this method make it ideal for biomedical applications.

4.3.1 Materials

Ethanol (99,9%, Labochem), Acetic acid ($\geq 99,7\%$, Sigma-Aldrich), (3-bromopropyl)trimethoxysilane ($\geq 97,0\%$, Aldrich), Tin(II) 2-ethylhexanoate (95%, Aldrich), Propargyl alcohol (99%, Aldrich), 4-pentynoic acid (98%, Alfa Aesar), *N,N'*-dicyclohexylcarbodiimide (DCC) (99%, Aldrich), 4-dimethylaminopyridine (DMAP) (99%, Aldrich), Sodium azide (NaN_3) (99%,

Acros), Copper bromide (CuBr) (98%, Acros), *N,N,N',N'',N'''*-pentamethyldiethylenetriamine (PMDETA) (99%, Aldrich), poly(ethylene glycol)monomethylether (PEG) ($M_n=2000$, Fluka), $\text{FeCl}_3 \cdot 6\text{H}_2\text{O}$ (97%, Sigma-Aldrich) were used as received. ϵ -Caprolactone (ϵ -CL) was distilled under vacuum over CaH_2 . *N,N*-Dimethyl formamide (DMF) and dichloromethane (99%, CH_2Cl_2 , J. T. Baker) were previously dried and distilled over phosphorus pentoxide.

4.3.2 Synthesis of Acetylene End-Functionalized PCL

Poly(ϵ -caprolactone) with alkyne end-functionality (a-PCL) was prepared by Ring Opening Polymerization of ϵ -CL (5,0 mL; 0,047 mol) in bulk using tin(II) 2-ethylhexanoate as a catalyst (catalytic amount) and propargyl alcohol (0,102 mL; 1,175 mmol) as an initiator. The monomer, catalyst and initiator were added to a previously flamed Schlenk tube equipped with a magnetic stirring bar in the order mentioned. The tube was degassed with 3 freeze-pump-thaw cycles, left under nitrogen, and placed in a thermostated oil bath at $110\text{ }^\circ\text{C}$ for 18 h. After the polymerization the mixture was diluted with THF and precipitated into an excess amount of methanol. Then it was filtrated (filter pore $n^\circ 4$) and dried overnight at room temperature under vacuum. $[\text{M}]_0/[\text{I}]_0=40$; conversion= 67%; $M_{n,\text{theo}}=3100$; $M_{n,\text{NMR}}=1613$; $M_{n,\text{GPC}}=6000$ (relative to linear polystyrene); $M_w/M_n=1,10$. $^1\text{H NMR}$ (CDCl_3, δ): 4,66 (2H, $\text{CH}\equiv\text{C}-\text{CH}_2\text{O}$), 4,03 (2H, $\text{CH}_2\text{OC}=\text{O}$ of PCL), 3,62 (2H, CH_2OH , end group of PCL), 2,28 (2H, $\text{C}=\text{OCH}_2$ of PCL), 1,20-1,80 (6H, CH_2 of PCL). The schematic synthesis is depicted in Figure 4.3.

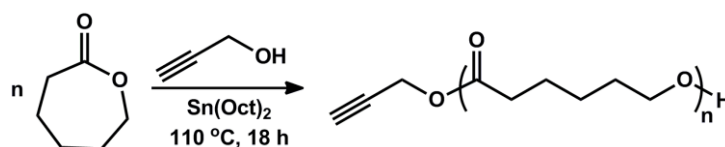


Figure 4.3: synthesis of a-PCL

4.3.3 Synthesis of Acetylene End-Functionalized PEG

Mono hydroxyl functional PEG ($M_n: 2000\text{ g/mol}$, 3,0 g, 1,5 mmol) was

dissolved in 25 mL of dry CH_2Cl_2 , and 4-pentynoic acid (0,22 g, 2,25 mmol) and DMAP (0,18 g, 1,5 mmol) were successively added to the reaction mixture. After stirring 5 min at room temperature, a solution of DCC (0,46 g, 2,25 mmol) in 15 mL of CH_2Cl_2 was added to the reaction mixture and stirred overnight at room temperature. After filtration of the salt, the solution was concentrated and product was purified by column chromatography over silica gel eluting with CH_2Cl_2 /ethyl acetate mixture (1:10) and then with CH_2Cl_2 /MeOH (10:1). Finally, concentrated solution of acetylene end functionalized PEG (a-PEG) was precipitated in diethyl ether and filtered. ^1H NMR (CDCl_3, δ): 4,25 (t, 2H, PEG- $\text{OCH}_2\text{CH}_2\text{-OC=O}$), 3,89-3,54 (m, 8H, PEG- $\text{OCH}_2\text{CH}_2\text{OC=O}$, $-\text{OCH}_2\text{CH}_2-$ of PEG, and $\text{CH}_2\text{CH}_2\text{-O}$), 3,36 (s, 3H, $\text{CH}_3\text{-OCH}_2\text{CH}_2$). 2,56-2,48 (m, 4H, $\text{CH}\equiv\text{CCH}_2\text{CH}_2\text{C=O}$), 1,97 (t, 1H, $\text{CH}\equiv\text{CCH}_2\text{-CH}_2\text{C=O}$). The schematic synthesis is depicted in Figure 4.4.

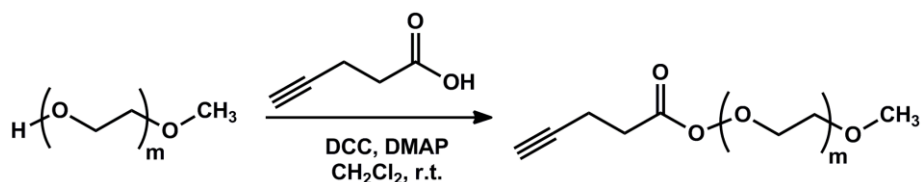


Figure 4.4: Synthesis of a-PEG

4.3.4 Synthesis of Magnetite nanoparticles

See paragraph 4.2.2

4.3.5 Functionalization of Magnetite nanoparticles with (3-Bromopropyl)trimethoxysilane

Acetic acid (3 mL), 3-(bromopropyl)trimethoxysilane (0,239 mL) and magnetic NPs (74 mg) were added to a solution of water and ethanol (1:10 vol/vol). The solution was left under magnetic stirring for 24h at room temperature. The black precipitate was separated with a magnet and washed several time with distilled water. The Fe_3O_4 NPs were redispersed in distilled water. The concentration of bromo functional magnetite NPs ($\text{Fe}_3\text{O}_4\text{-AC-Br}$ NPs) aqueous dispersion was determined by means of TGA to be 6,0 mg/ml

4.3.6 Azidation of Bromine-functionalized Magnetite nanoparticles

Fe₃O₄-AC-Br NPs in aqueous solution (10 mL) were added to a flask containing a large excess of sodium azide (100 mg, ~13 equiv. Br). The solution was left under stirring at room temperature for 48 h. The azidation process was stopped by centrifugation of the solution. The sample was centrifuged 3 times at 5000 rpm for 20 min and washed with water. Successively the pellet containing azido functional magnetite (Fe₃O₄-AC-N₃) nanoparticles was dried at room temperature for 48 h.

4.3.7 Functionalization of Azide-magnetite nanoparticles with *a*-PCL via Click Reaction

a-PCL (55,8 mg, 1 equiv.), CuBr (3,9 mg, 1,5 equiv.), and 2 mL of DMF were added in a Schlenk tube. 10 mg of the magnetic NPs (0,9 equiv. N₃) were dispersed in 3 mL of DMF and added to the tube. Finally, PMDETA (5,8 μL, 1,5 equiv.) was added to the solution. The tube was degassed with 3 freeze-pump-thaw cycles, left under vacuum and put in a thermostated bath at 50 °C for 48 h. In order to stop the reaction, the solution was centrifuged at 5000 rpm for 30 min, then the supernatant was removed and the NPs were washed with toluene. The solution was centrifuged again at 5000 rpm for 30 min. This process was repeated two times with toluene and one time with water in order to remove unreacted polymer and copper catalyst. Successively, the NPs (Fe₃O₄-AC-N₃ NPs) were dried for 48h at room temperature.

4.3.8 Functionalization of the azide-magnetite nanoparticles with alkyne-PEG via Click reaction

Alkyne-PEG (22,5 mg, 1 equiv.) and CuBr (2,6 mg, 1,5 equiv.) were dissolved in 2 mL of DMF in a Schlenck tube. 8,2 mg of Fe₃O₄-AC-N₃ NPs (1,2 equiv. N₃) and PMDETA (3,7 μL, 1,5 equiv.) were added to the solution. The tube was degassed with 3 freeze-pump-thaw cycles, left under vacuum and put in a thermostated bath at 50 °C for 48 h. In order to stop the reaction, the solution was centrifuged at 5000 rpm for 30 min. The pellet dispersed in 0.5

mL of THF and precipitated in 5 mL of cold distilled water, then 2 drops of hydrochloric acid were added to the solution and the solution was put at 4 °C for 4 h. The supernatant solution was removed and the NPs were dried under vacuum at room temperature overnight.

4.3.9 Characterization techniques

¹H NMR spectra of 5–10% (w/w) solutions in CDCl₃ with Si(CH₃)₄ as an internal standard were recorded at room temperature at 250 MHz on a Bruker DPX 250 spectrometer. Gel permeation chromatography (GPC) measurements were obtained from a Viscotek GPC max Autosampler system consisting of a pump, a Viscotek UV detector, and a differential refractive index detector. Tetrahydrofuran (THF) was used as an eluent at flow rate of 1,0 mL·min⁻¹ at 30 °C. Molecular weights of the a-PCL and a-PEG were determined with the aid of polystyrene standards. Fourier transform infrared (FTIR) spectra were recorded on a Perkin-Elmer FTIR Spectrum One B spectrometer. Thermogravimetric analysis (TGA) was performed on a Perkin-Elmer Diamond TA/TGA instrument at a heating rate of 10 °C·min⁻¹ under nitrogen flow.

Magnetic hysteresis loops were measured at room temperatures on coated magnetite water dispersion by using a vibrating sample magnetometer (VSM) operating in the magnetic field range -10 kOe < H < +10 kOe. The diamagnetic contribution of sample holder and solvent were significant. A reference measurement was preliminarily done by measuring the magnetic response of the sample holder filled with the same amount of pure solvent (i.e., without the magnetic NPs). The magnetic contribution ascribed to magnetite NPs (before and after functionalization) was obtained from the measured curves by subtracting the reference curve.

Samples were observed by TEM by examining in a 300 keV transmission electron microscope (TEM) Philips CM30. TEM micrographs were processed with a slow scan CCD camera and analyzed with the Digital Micrograph program. The TEM observations were always performed using a very low electron flux in order to avoid any structural modification of the sample

induced by the electron beam.

4.4 Photochemical synthesis of gold-PEG core-shell nanoparticles

In this part, we report a new, fast and convenient method for preparing gold nanoparticles with a poly(ethylene glycol)-diacrylate (PEGDA) shell in water. It is well known that polymer nanospheres can be prepared by conventional techniques of water-emulsion polymerization. These environmentally friendly products comprise a large population of nanometric size polymer particles dispersed in the continuous aqueous phase. Polyethylene glycol (PEG) was used as hydrophilic monomer in emulsifier-free emulsion polymerization to form polymeric nanoparticles by the UV-induced process. At the same time, gold was generated as the core of the PEG nanosphere by the reduction of HAuCl_4 activated through the radical photogenerated from 2-hydroxy-2-methyl-1-phenyl-1-propanone. This one-step procedure is very easy to implement and fast. Moreover, the fact that this method is performed in water makes it ideal for biomedical applications.

4.4.1 Materials

Poly(ethylene glycol) diacrylate (PEGDA) ($M_n = 575$, Aldrich), hydrogen tetrachloroaurate (III) (HAuCl_4) 30% wt solution in chloridric acid (99,9%, Aldrich), 2-hydroxy-2-methyl-1-phenyl-1-propanone (Darocure 1173, CIBA) were used as received.

4.4.2 Synthesis of gold nanoparticles

The reduced Au was coated with PEGDA via UV-curing. In a typical procedure 10 mg of HAuCl_4 and 80 mg of radical photoinitiator were added to 60 ml of deionized water into a three-necked flask under magnetic stirring and nitrogen inlet. Subsequently 2 g of PEGDA were added dropwise and then the mixture was exposed to UV light for 30 minutes.

4.4.3 Characterization techniques

Particle sizes and size distribution of gold nanoparticles were measured by using DLS. The DLS measurements were done on a Zetasizer Nanoseries ZS90 (Malvern). Acrylic double bond conversion, as a function of irradiation time, was evaluated by means of real-time FT-IR employing a Thermo-Nicolet 5700. The morphology of the water dispersion was evaluated by TEM analysis. Samples were observed by TEM by examining in a 300 keV transmission electron microscope (TEM) Philips CM30. TEM micrographs were processed with a slow scan CCD camera and analyzed with the Digital Micrograph program. The TEM observations were always performed using a very low electron flux in order to avoid any structural modification of the sample induced by the electron beam. Chemical compositions of the dried particles were analyzed both with attenuated total reflectance (ATR) and X-ray Photoelectron Spectroscopy (XPS). ATR analyses were performed on dried samples by using Thermo-Nicolet 5700. Before the XPS analyses, the PEGDA polymer was prepared on a Silicon substrate with a drop, and subsequently put for 12 hours in a dryer. The silicon substrate was chosen because the Silicon peaks do not overlap with the signal of interest in case the drop is not homogeneous. In any case, the drop results very homogeneous because we have not detected the presence of the silicon signal from the sample. XPS was performed using a VersaProbe5000 Physical Electronics X-ray photoelectron spectrometer with a monochromatic Al source and a hemispherical analyzer. An electron flood gun combined with Argon ion gun were employed because the samples were insulating polymers. Survey scans as well as narrow scans were recorded with a 100 μm spot size on an area of 100 μm \times 800 μm spot size. Data acquisition and processing were implemented with the instrument software Summit and MultiPak 8.2.

The surface Plasmon resonance of nanoparticles was studied using UV-Vis spectra. The UV-Vis spectra were recorded by means of a double beam UNICAM UV2 (ATI Unicam, Cambridge, UK) spectrophotometer with variable slit width in a spectral range of 190 e 1100 nm, interfaced to a

computer via “Vision 32” software for data elaboration. The range between 300 and 800 nm was monitored with a scan step of 1 nm.

4.5 Hollow-gold nanoparticles coated with Poly(ethylene glycol) methyl ether thiol

In this part we report the synthesis of hollow gold nanoparticles following a method described in literature [5]. In a first time cobalt nanoparticles were prepared by reduction of cobalt salts with sodium borohydride under inert atmosphere. In a second time, gold salts were added to the colloidal suspension of cobalt nanoparticles. These gold salts were reduced to gold atoms as soon as they entered in contact with cobalt forming a gold shell while consuming the cobalt core. By varying the reaction parameters we were able to find a correlation between nanoparticles morphology and the localization of the surface plasmon resonance which has, to our knowledge, never been reported in literature yet. In a third time one specific sample was coated with poly(ethylene glycol) methyl ether thiol exploiting the natural affinity of thiol groups for gold.

4.5.1 Materials

Sodium citrate (analytical grade, Sigma), cobalt chloride (analytical grade, R.P Normapur™ AR), sodium borohydride (99%, Aldrich), hydrogen tetrachloroaurate (III) (HauCl₄) 30% wt solution in chloridric acid (99,9%, Aldrich), Poly(ethylene glycol) methyl ether thiol (MeO-PEG-SH) (Mn = 5000, Aldrich).

4.5.2 Preparation of hollow gold nanoparticles

The synthesis process is based on templating using cobalt (Co) nanoparticles as initial seeds via a galvanic reaction with Au³⁺ ions as explained previously in the literature [5]. This synthesis must be done completely under inert environment, to this aim every solution was degassed with N₂ before use.

The solution was prepared in round-bottomed flask, under N₂ atmosphere, mixing 100 mL of deionized water with sodium citrate aqueous solution (0.1M;

42.82 mg in 1 mL of deionized water), fresh sodium borohydride aqueous solution (1M; 37.83 mg in 1 mL of deionized water) and cobalt chloride aqueous solution (0.5M; 64.92 mg in 1 mL of deionized water). The solution was left under N₂ atmosphere and magnetic stirring for 1h. Successively a certain number of 50 μL injections of hydrogen tetrachloroaurate (III) aqueous solution (0.1M; 105 μL in 5 mL of deionized water) were done, waiting 1 min between every injection. The solution was left under N₂ atmosphere and magnetic stirring for one hour, and then for one night without N₂. The respective volume of every solution was modified in order to obtain different morphologies. All the reaction parameters are reported in Table 4.1.

Table 4.1: different sets of reaction parameters for the synthesis of HGNS

	Sod citrate	NaBH ₄	CoCl ₂	HAuCl ₄
Sample Nber	μL	μL	μL	μL
1	400	100	100	250
2	400	100	100	700
3	190	180	100	700
4	330	250	100	700
5	900	100	100	700
6	190	180	100	450
7	330	250	100	450
8	900	100	100	450

4.5.3 Coating of hollow gold nanoparticles with Poly(ethylene glycol) methyl ether thiol

Another hollow gold nanoparticles sample was prepared (Sample 9) using 900 μL of sodium citrate, 250 μL of sodium borohydride, 100 μL of cobalt chloride and 700 μL of hydrogen tetrachloroaurate solution, as described previously.

These new nanoparticles were coated with Poly(ethylene glycol) methyl ether thiol by using the affinity between the thiol groups and gold. In a typical procedure 400 mg of polymer were solubilized in 10 mL of deionized water, 20mL of Sample 9 were added to the solution and it was left at room temperature, under magnetic stirring for 6h. The coated nanoparticles were purified by dialysis against water (MWCO = 12-14,000 Da) and, then concentrated by ultrafiltration (MWCO = 100,0000 Da).

4.5.4 Characterization techniques

The morphology of the water dispersion was evaluated by TEM analysis. Samples were observed by TEM by examining in a 300 keV transmission electron microscope (TEM) Philips CM30. TEM micrographs were processed with a slow scan CCD camera and analyzed with the Digital Micrograph program. The TEM observations were always performed using a very low electron flux in order to avoid any structural modification of the sample induced by the electron beam.

Particle sizes and size distribution of coated hollow gold nanoparticles were measured by using DLS. The DLS measurements were done on a Zetasizer Nanoseries ZS90 (Malvern).

The surface Plasmon resonance of nanoparticles was studied using UV-vis spectra. The UV-Vis spectra were recorded by means of a double beam UNICAM UV2 (ATI Unicam, Cambridge, UK) spectrophotometer with variable slit width in a spectral range of 190 e 1100 nm, interfaced to a computer via "Vision 32" software for data elaboration. The range between 400 and 800 nm was monitored with a scan step of 1 nm.

4.6 *SiO₂@Au nanoshell coated with Poly(ethylene glycol) methyl ether thiol*

This synthesis is based on different works reported in literature[6][7], however each step of the process was adapted in order to obtain the most suitable device for our aims. In a first time SiO₂ nanoparticles were prepared following the

well known Stöber method [8], then the nanoparticles were functionalized with (3-Aminopropyl) triethoxysilane and gold seeds were grafted onto the surface. Eventually these gold seeds were grown by reduction of gold salts with hydroxylamine hydrochloride to form a uniform gold shell. The amount of gold salts used on the last step was varied in order to study the correlation between shell thickness and the surface plasmon resonance localization. On a second time, the Stöber method was slightly modified to obtain smaller nanoparticles and form smaller nanoshells, never reported in literature to our knowledge. In a third time these nanoshell were coated with poly(ethylene glycol) methyl ether thiol exploiting the natural affinity between thiol groups and gold.

4.6.1 Materials

Ethanol ($\geq 99,8\%$, Fluka), Tetraethyl orthosilicate (TEOS) ($\geq 99,0\%$, Aldrich), NH_4OH (28-30% in H_2O , Sigma-Aldrich), Chloridric acid (37% in H_2O , Sigma-Aldrich), (3-Aminopropyl)triethoxysilane (APTES) ($\geq 98\%$, Sigma-Adrich), Sodium hydroxide (NaOH) ($\geq 98\%$, Sigma-Adrich), Tetrakis (hydroxymethyl) phosphonium chloride (THPC) (80% in H_2O , Aldrich), Hydrogen tetrachloroaurate (III) (HauCl_4) (99,999%, Aldrich), Sodium chloride (NaCl) ($\geq 99,5\%$, Sigma), Potassium carbonate (99,995%, Aldrich), Hydroxylamine hydrochloride ($\text{NH}_2\text{OH}\cdot\text{HCl}$) (99,0%, Sigma-Aldrich), Poly(ethylene glycol) methyl ether thiol (MeO-PEG-SH) ($M_n = 5000$, Aldrich).

4.6.2 Preparation of SiO_2 nanoparticles (Stöber method – 110 nm)

The formation of 110 nm SiO_2 nanoparticles is based on the famous work of Stöber et al. [8]. In a typical procedure, 34 mL of ethanol, 2,8mL of TEOS and 2,8 mL of NH_4OH were added to a round bottom flask. The solution was left under magnetic stirring, at room temperature for 8 h.

The solution was centrifuged for 10' at 10000 rpm and the pellet was washed with ethanol. The process was repeated twice and the nanoparticles were dispersed in ethanol.

4.6.3 *Functionalization of SiO₂ nanoparticles with (3-aminopropyl) triethoxysilane (APTES)*

This step was based on the work of Wu et al. [9], 2 mL of deionized water, 13 mL of ethanol, 20 μ L of chloridric acid and 500 μ L of APTES were added to a round bottom flask. The solution was left under magnetic stirring at room temperature for 30 min.

5 mL of SiO₂ nanoparticles colloidal suspension were added to the solution and the flask was put into a thermostatic bath at 60°C. The solution was left under magnetic stirring, at 60°C for 6h.

The solution was centrifuged for 10' at 10000 rpm and the pellet was washed with ethanol. The process was repeated twice and the nanoparticles were dispersed in ethanol.

4.6.4 *Synthesis of gold nanoparticles (GNPs)*

Following the method reported in literature [10], 45 mL of deionized water, 3 mL of NaOH aqueous solution (0.1 M) and 1 mL of THPC aqueous solution (1.2 mL diluted to 100 mL with water) were added to a round bottom flask in a sonicating bath. The solution was left sonicating at room temperature for 2 min. 2 mL of an aqueous solution of HAuCl₄ (25 mM) were added to the solution. After a few minutes under sonication the color of the solution goes from yellow to orange-brown. The solution was kept at 4°C in a dark glass bottle for 15 days before use.

4.6.5 *Functionalization of SiO₂-APTES nanoparticles with GNPs*

40 mL of GNPs colloidal suspension, 2,5 mL of NaCl aqueous solution (1M) and 100 μ L of SiO₂-APTES colloidal suspension were added to a test tube. The tube was sonicated for 1' and the solution was left still for a night at room temperature.

The solution was centrifuged for 10 min at 10000 rpm and the pellet was washed with deionized water. The process was repeated twice and the nanoparticles were dispersed in water.

4.6.6 *GNPs reduction on SiO₂-APTES nanoparticles surface*

The Kcarb solution was prepared, putting in a flask 24,9 mg of potassium carbonate and 1,74 mL of H₂AuCl₄ aqueous solution (25 mM) diluted to 100 mL with deionized water.

Each sample was prepared by putting in a flask 0,5 mL of SiO₂-GNPs colloidal suspension, the volume indicated in Table 4.2 of Kcarb solution and 25 mL of an NH₂OH•HCl aqueous solution (130 mg/L) dropwise under vigorous magnetic stirring.

The solutions were left under magnetic stirring overnight at room temperature.

Table 4.2: Experimental conditions

	SiO ₂ _GNPs	Kcarb	NH ₂ OH-HCl
	mL	mL	mL
Nanoshell 8	0.5	50	25
Nanoshell 9	0.5	40	25
Nanoshell 10	0.5	30	25
Nanoshell 11	0.5	20	25
Nanoshell 12	0.5	10	25
Nanoshell 13	0.5	5	25

4.6.7 *Preparation of SiO₂ nanoparticles (Stöber method – 25-65 nm)*

Successively the method was slightly modified in order to obtain smaller SiO₂ nanoparticles, 34 mL of ethanol, 2,8mL of tetraethyl orthosilicate (TEOS) and NH₄OH (see Table 4.3) were added to a round bottom flask in a sonicating bath. The solution was left sonicating at room temperature for 6 h.

Table 4.3: Experimental conditions for SiO₂ nanoparticles preparation

	Ethanol	TEOS	NH ₄ OH
	mL	mL	mL
SiO ₂ NPs 5	34	2.8	1.7
SiO ₂ NPs 6			2.0
SiO ₂ NPs 7			2.3
SiO ₂ NPs 8			2.6

The solution was centrifuged for 10 min at 10000 rpm and the pellet was washed with ethanol. The process was repeated twice and the nanoparticles were dispersed in ethanol.

The functionalization of SiO₂ nanoparticles with APTES was realized as described before so as the synthesis of gold nanoparticles.

The functionalization with GNPs was slightly different though: 10 mL of GNPs colloidal suspension, 625 µL of NaCl aqueous solution (1M) and 50 µL of SiO₂-APTES colloidal suspension were added to a test tube. The tube was sonicated for 1min and the solution was left still for a night at room temperature.

The solution was centrifuged for 10 min at 10000 rpm and the pellet was washed with deionized water. The process was repeated twice and the nanoparticles were dispersed in water.

Successively, for GNPs reduction on SiO₂-APTES nanoparticles surface, the Kcarb solution was prepared, putting in a flask 24,9 mg of potassium carbonate and 1.74 mL of HAuCl₄ aqueous solution (25 mM) diluted to 100 mL with deionized water. Each sample was prepared by putting in a flask 0,5 mL of SiO₂-GNPs colloidal suspension, the volume indicated in Table 4.4 of Kcarb solution and 25 mL of an NH₂OH•HCl aqueous solution (130 mg/L) dropwise under vigorous magnetic stirring.

The solutions were left under magnetic stirring overnight at room temperature.

Table 4.4: Kcarb solution volume for each sample preparation

	Kcarb
	mL
1	2.5
2	3.75
3	5

4.6.8 *Coating of Sample with Poly(ethylene glycol) methyl ether thiol*

Sample 3 was coated with poly(ethylene glycol) methyl ether thiol by using the affinity between the thiol groups and gold. In a typical procedure 400 mg of polymer were solubilized in 10 mL of deionized water, 20mL of Sample 3 were added to the solution and it was left at room temperature, under magnetic stirring for 6h. The coated nanoparticles were purified by centrifugation (3800 rpm for 2h) and redispersed in water.

4.6.9 *Characterization techniques*

Gold nanoparticles sizes and size distribution were measured using Dynamic Light Scattering (DLS). The DLS measurements were done on a Zetasizer Nanoseries ZS90 (Malvern).The morphology of the water dispersion was evaluated by TEM analysis. Samples were observed by TEM by examining in a 300 keV transmission electron microscope (TEM) Philips CM30. TEM micrographs were processed with a slow scan CCD camera and analyzed with the Digital Micrograph program. The TEM observations were always performed using a very low electron flux in order to avoid any structural modification of the sample induced by the electron beam.

The surface Plasmon resonance of nanoparticles was studied using UV-vis spectra. The surface Plasmon resonance of nanoparticles was studied using UV-Vis spectra. The UV-Vis spectra were recorded by means of a double beam UNICAM UV2 (ATI Unicam, Cambridge, UK) spectrophotometer with variable slit width in a spectral range of 190 e 1100 nm, interfaced to a

computer via “Vision 32” software for data elaboration. The range between 400 and 1100 nm was monitored with a scan step of 1 nm.

References

- [1] Zhiya M., Huizhou L., *Chin. Partic.*, **2007**, 5, 1-10.
- [2] Gong P., Yu J., Sun H., Hong J., Zhao S., Xu D., *J Appl Polym Sci*, **2006**, 101, 1283-1290.
- [3] Dilnawaz F., Singh A., Mohanty C., Sahoo S. K., *Biomaterials*, **2010**, 31, 3694-3706.
- [4] J. Amici, et. Al., *Euro. Pol. J*, **2011**, 47, 1250-1255.
- [5] J.Z. Zhang, *J. Phys. Chem. Lett.*, **2010**, 1, 686.
- [6] S.J. Oldenburg, R.D. Averitt, S.L. Westcott, N.J. Halas, *Chem. Phys. Lett.*, **1998**, 288, 243-247.
- [7] Y. Wang, W. Qian, Y. Tan, S. Ding, H. Zhang, *Talanta*, **2007**, 72, 1134-1140.
- [8] W. Stöber, A. Fink, E. Bohn, *J. Coll. Int. Sci.*, **1968**, 26, 62-69.
- [9] D.J. Wu, X.J. Liu, L.L. Liu, W.P. Qian, *Appl. Phys.*, **2008**, A 92, 279-282.
- [10] D. G. Duff, A. Baiker, *Langmuir*, **1993**, 9, 2301-2309.

5. Hyperthermia

5.1 PEG coated magnetite nanoparticles via photopolymerization

Magnetite nanoparticles were synthesized by a chemical co-precipitation of Fe^{2+} and Fe^{3+} ions under alkaline conditions, following a previous method reported in literature [1]. The concentration of $\text{Fe}^{2+}/\text{Fe}^{3+}$ was 1:2 and the synthesis was carried out under inert atmosphere to prevent Fe^{2+} oxidation to Fe^{3+} . DLS measurements showed an average size of Fe_3O_4 particles of about 400 nm (see Figure 5.2). The magnetization curves showed superparamagnetic property (i.e. no remanence effect) of the bare particles and relatively high magnetization values (see Figure 5.1).

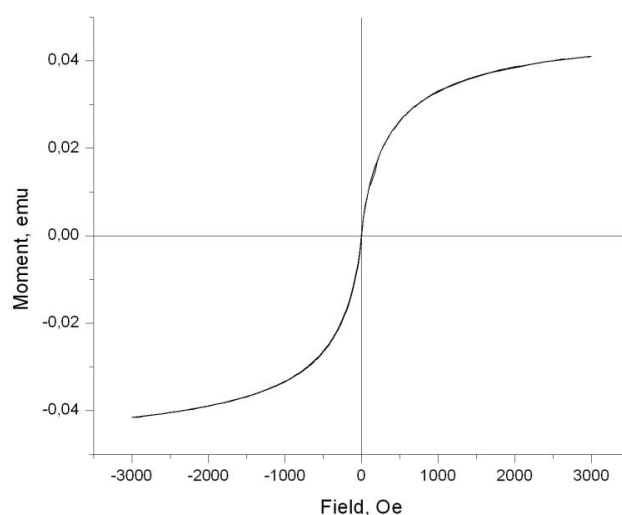


Figure 5.1: Magnetization versus applied magnetic field of synthesized bare Fe_3O_4 particles

The achieved magnetite nanoparticles were coated with PEGDA by UV-activation in water under nitrogen inlet. The Fe_3O_4 particles show photoinitiator activity, as already reported in literature [2] and recently investigated by our group [3]: semiconductor nanoparticles upon photoexcitation can generate radicals which in turn start polymerization chains.

Under UV-light, valence band holes and conduction band electrons can be generated on Fe_3O_4 surface; valence band holes have intense liability to capture electrons and acrylic monomer can be initiated by valence band holes to produce cured polymeric coating on the particles surface. Therefore, PEGDA coating on Fe_3O_4 particles was performed by UV irradiation of water dispersion containing the magnetite previously synthesized. The magnetite/PEGDA ratio was modified in the range between 1.25 up to 15 phr. The size distribution curves for the bare Fe_3O_4 and for the coated particles with increasing Fe_3O_4 /PEGDA ratio are reported in Figure 5.2.

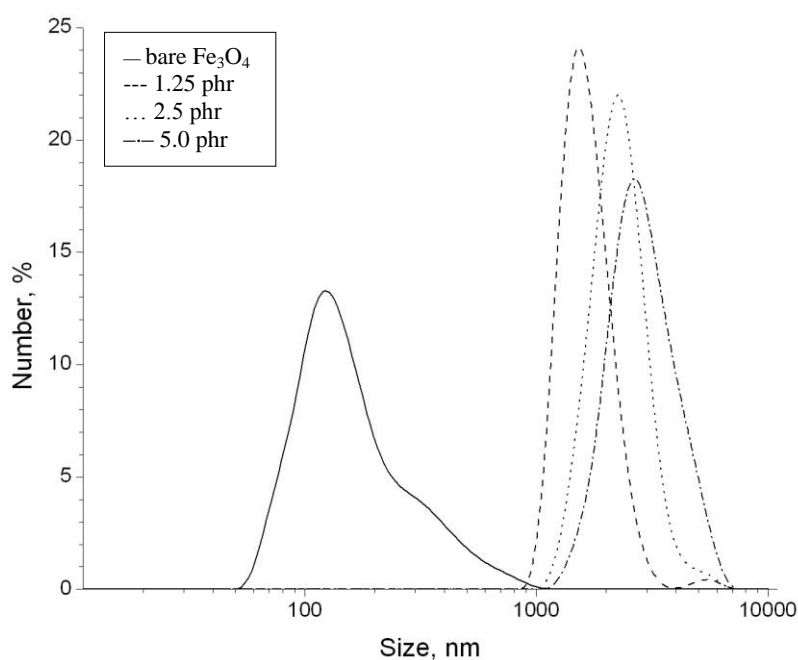


Figure 5.2: Size distribution curves for the bared Fe_3O_4 and for the PEGDA coated particles

From the distribution curves it can be seen that the size of magnetite particles has increased because of organic coating and also because of their possible aggregation. The increase of the average size and size distribution by increasing the magnetite content could be due to formation of smaller nanoparticles aggregates. This was further confirmed by TEM analysis. Coating the Fe_3O_4 particles with PEGDA endowed the particles with excellent

biocompatibility and hydrophilicity, which is a mandatory request for medical applications.

In order to confirm the PEGDA shell formation around magnetite nanoparticles, the XPS analyses were performed on the core-shell nanoparticles. The high resolution XPS spectra of survey and C 1s of functionalized nanoparticles are reported in Figure 5.3 and Figure 5.4 respectively.

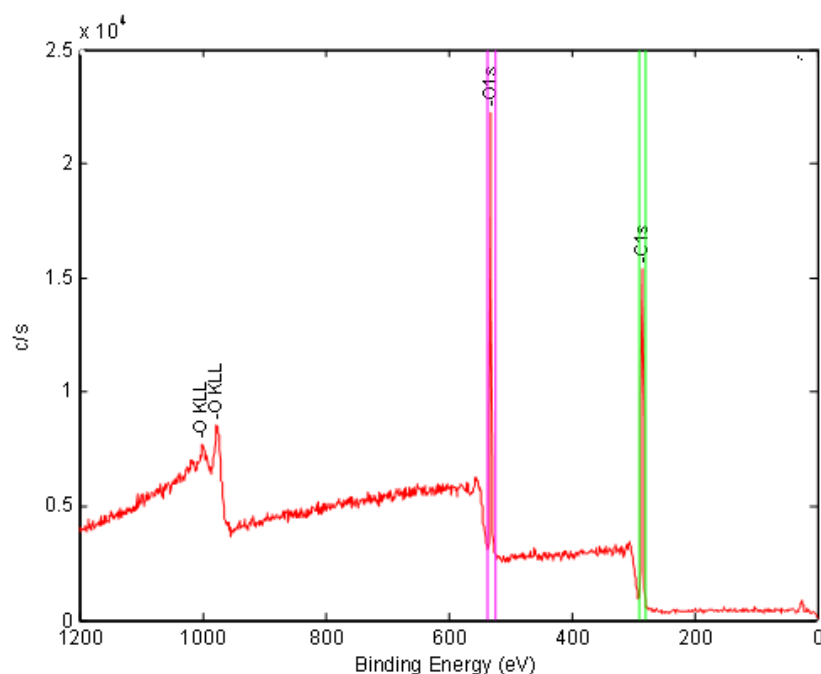


Figure 5.3: High resolution XPS spectra of survey spectra of functionalized Fe_3O_4 particles

In survey scan (Figure 5.3) we used 187.85 eV pass energy and 2 kV argon ion gun. In the survey spectra it is possible to observe typical spectrum of polymeric material (PEGDA), with evidence of Oxygen and Carbon signal. A mapping procedure on the investigated sample did not show any Iron signal from the nanoparticles. This is clear evidence that the PEGDA shell around the magnetite nanoparticles is at least 5 nm thick (which is the maximal depth resolution of XPS analysis).

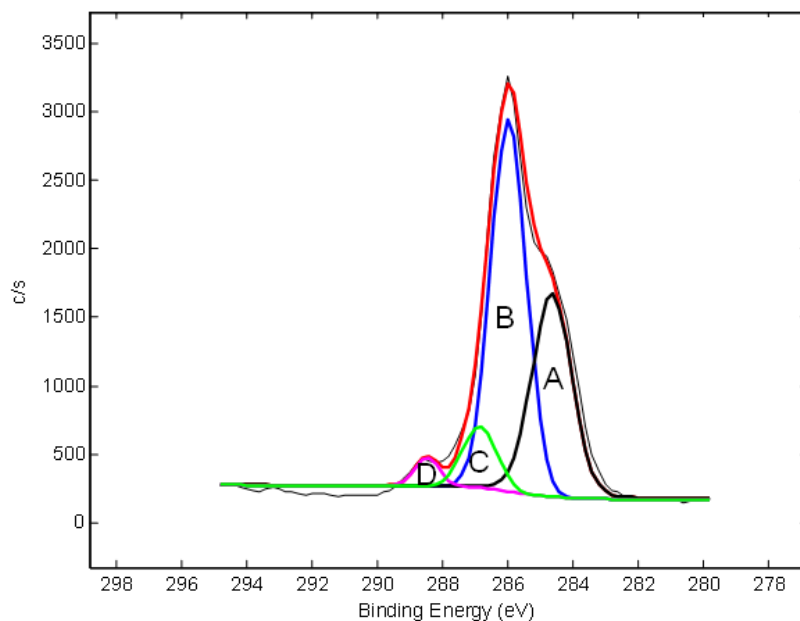


Figure 5.4: High resolution XPS spectra of C 1s of functionalized Fe_3O_4 particles

The high resolution spectra were carried on C1s with a pass energy of 23.5 eV. In Figure 5.4 it is reported the C1s signal with related deconvolution; the C1s signal were fitted with four components [4]. The 284.66 eV signal (A) corresponds to C-C bond, the 285.99 eV (B) correspond to C-C(=O)OR, the 286.87 eV (C) correspond COC, and 288.49 eV (D) is related to C(O)OR, as schematized in the Table 5.1.

Table 5.1: XPS C1s signal were fitted with four components

Attribution	B.E. eV (PEGDA)	Atomic Percentage (%)
A C-C	284.66	34.50
B C-C(=O)OR	285.99	54.06
C COC	286.87	8.58
D C(O)OR	288.49	2.85

From these analyses PEGDA seems uniformly distributed on magnetite. The degree of functionalization of the magnetite particles was evaluated through TGA analysis. The TGA curves for the bare Fe_3O_4 particles and for the PEGDA functionalized particles (samples achieved with a Fe_3O_4 content of 5 phr, as an example) are reported in Figure 5.5, depicting the variation of residual masses of the samples with temperature.

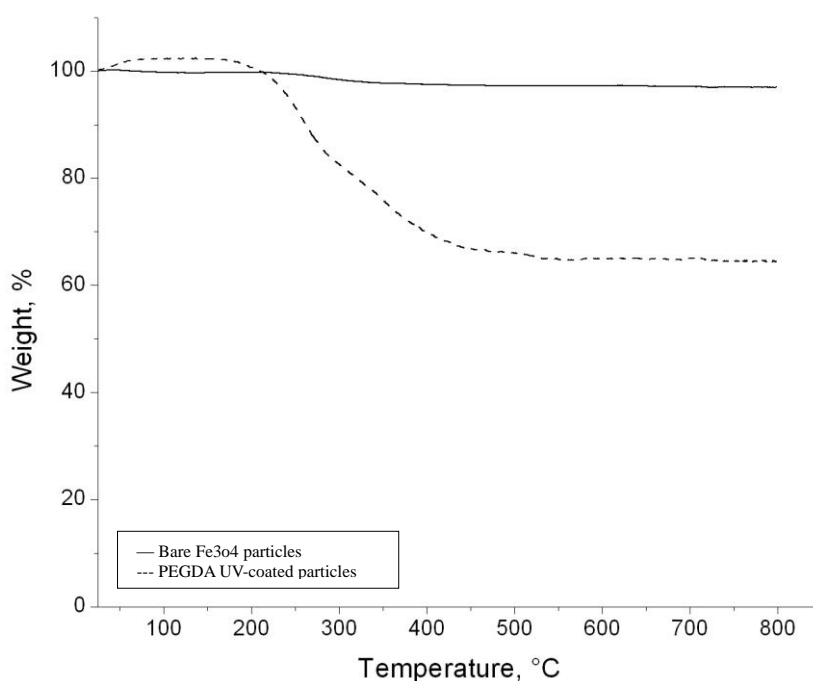
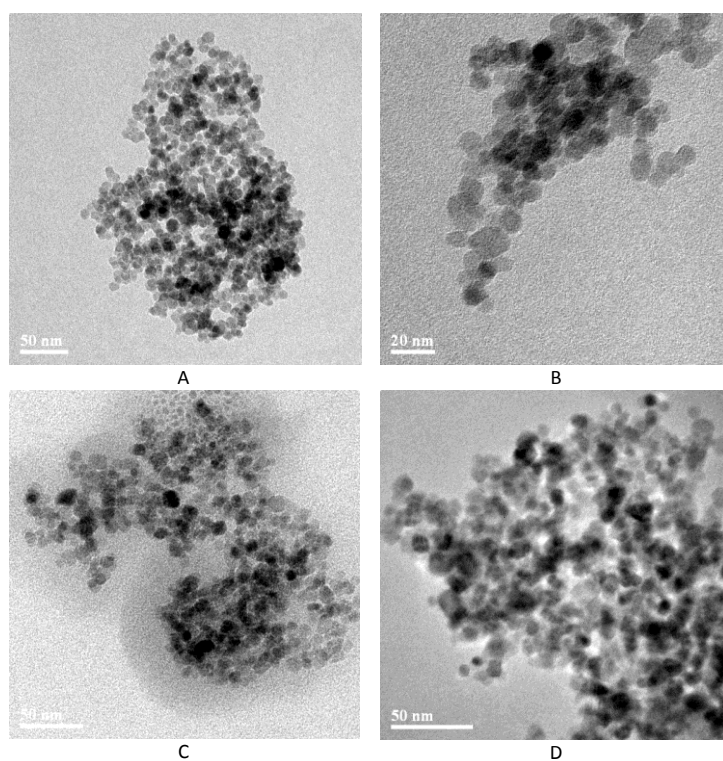


Figure 5.5: TGA curves of the bare Fe_3O_4 particles and of the PEGDA UV-coated particles

The absolute weight loss of the uncoated Fe_3O_4 is about 3,1% for the whole temperature range, due to the removal of adsorbed physical and chemical water. For PEGDA-coated particles, the main weight loss stage occurred at around 225 °C and can be attributed to the PEGDA decomposition. This curves indicated that the magnetite content was about 64%, with a PEGDA shell content which was calculated to be around 36% of the total weight.

The morphology of the coated magnetite particles was investigated by TEM analysis. The TEM micrographs of coated Fe_3O_4 particles achieved for the formulations containing 5 phr Fe_3O_4 are reported in Figure 5.6.



**Figure 5.6: TEM micrograph for the coated Fe₃O₄ particles
(A 2.5 phr 52000x, B 5.0 phr 110000x, C 1.25 phr 61000x, D 5 phr 89000x)**

It can be seen that the particles have a strong tendency to aggregate as a result of the interaction of the polymer coated on the nanoparticles. While the average size of the particles are in the nanometre range, within 3 to 10 nm, the large aggregates of the particles are around 1-2 μm in good agreement with the DLS analyses.

The magnetization curves for coated Fe₃O₄ nanoparticles are shown in Figure 5.7.

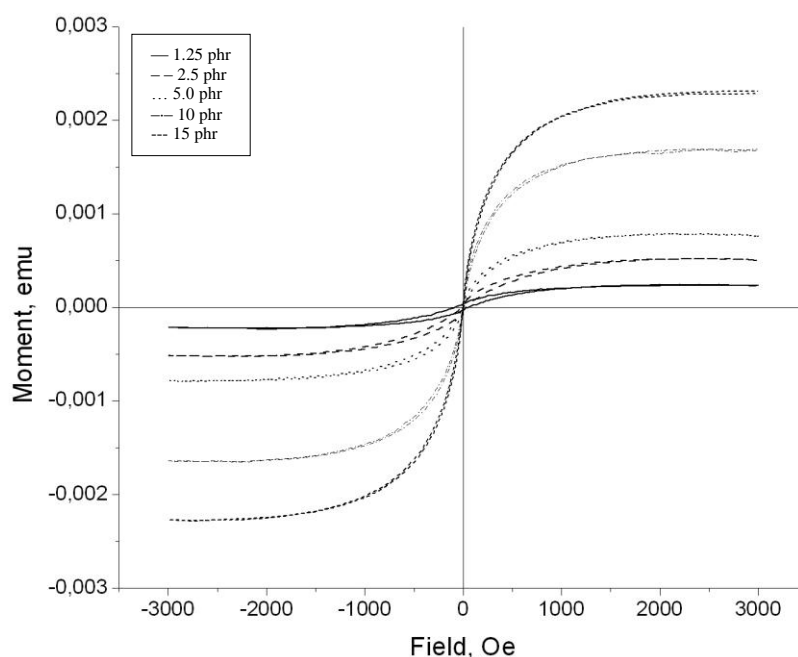


Figure 5.7: Magnetization versus applied magnetic field at room temperature

When the amount of magnetite is low with respect to the PEGDA (with a ratio within 1,5 to 2,5 phr) the hysteresis loop shows a non negligible coercivity and a remanence different from 0. This behaviour is not acceptable for biomedical applications, especially for in-vivo utilization. Nevertheless, it can be seen that by increasing the $\text{Fe}_3\text{O}_4/\text{PEGDA}$ ratio in the system up to 10-15 phr both remanence and coercivity values tend to zero: these samples show a superparamagnetic like behaviour, and therefore they are suitable for biomedical applications.

Conclusions

Magnetite nanoparticles were synthesized by a chemical co-precipitation of Fe^{2+} and Fe^{3+} ions under alkaline conditions the magnetization curves showed superparamagnetic property (i.e. no remanence effect) and relatively high magnetization values. The achieved magnetite nanoparticles were coated with PEGDA by UV-activation in water adapting a known methodology to nanoparticles coating for the very first time. After polymeric functionalization

DLS showed that size of magnetite particles has increased because of organic coating and also because of their possible aggregation. XPS analyses showed that the PEGDA shell around the magnetite nanoparticles is at least 5 nm thick and uniformly distributed on magnetite surface. From TEM morphological investigations, it is possible to observe that while the average size of the particles are in the nanometre range, within 3 to 10 nm, the large aggregates of the particles are around 1-2 μm in good agreement with the DLS analyses. The magnetization curves for coated Fe_3O_4 nanoparticles showed that only by increasing the $\text{Fe}_3\text{O}_4/\text{PEGDA}$ ratio in the system up to a value of 10-15 phr both remanence and coercivity tend to zero and makes the particles suitable for bio-medical applications. In conclusion, we have developed a novel and successful in-situ photochemical coating of magnetite nanoparticles which showed superparamagnetic-like behaviour.

5.2 PEG coated magnetite nanoparticles via UV-thiol-ene addition reaction

Magnetite nanoparticles were synthesized by a chemical co-precipitation of Fe^{2+} and Fe^{3+} ions under alkaline conditions, following previous method reported in literature[5][6][7][8][9][10]. The concentration of $\text{Fe}^{2+}/\text{Fe}^{3+}$ was 1:2 and the synthesis was carried out under inert atmosphere to prevent Fe^{2+} oxidation to Fe^{3+} . Citric acid was added during the synthesis in order to protect the nanoparticles avoiding macroscopic aggregations. The magnetization curves showed superparamagnetic property (i.e. no remanence effect) of the bare particles and relatively high magnetization values (see Figure 5.8).

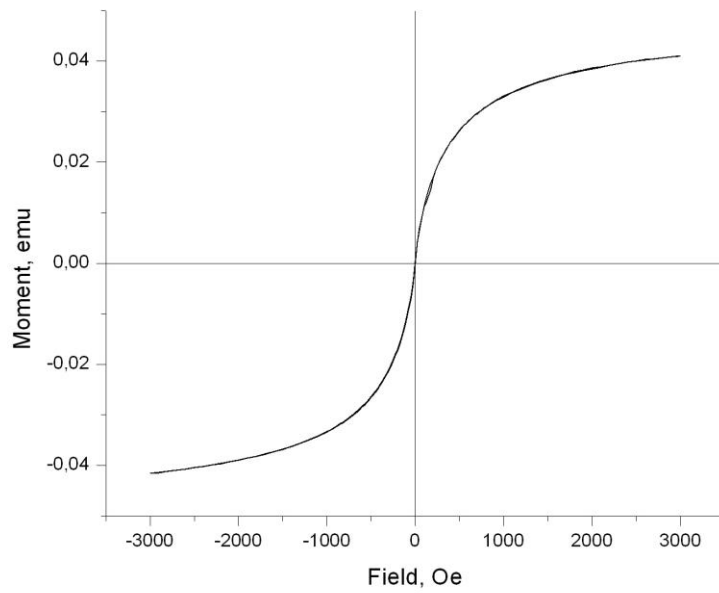


Figure 5.8: Magnetization versus applied magnetic field of synthesized bare Fe_3O_4 particles

DLS measurements showed an average size of Fe_3O_4 particles of about 30 nm (see DLS curve in Figure 5.9).

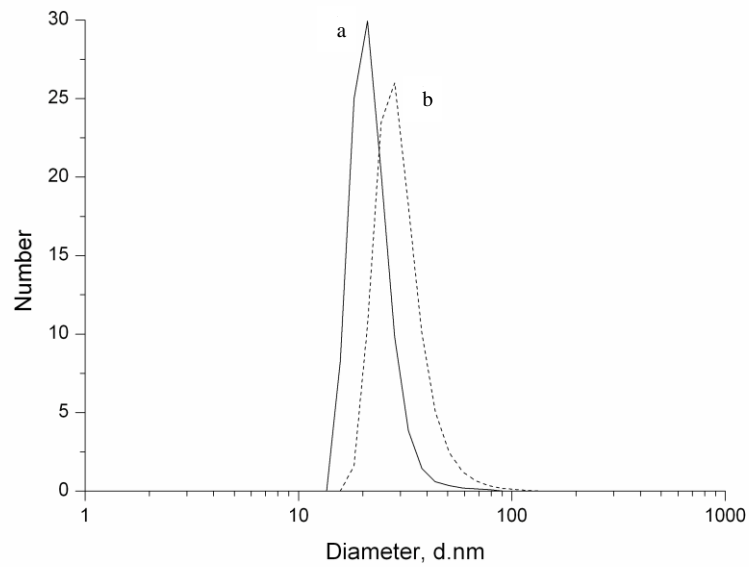


Figure 5.9: Size distribution curves for the bare Fe_3O_4 (curve a) and for the PEG-coated particles (curve b)

The achieved magnetite nanoparticles were functionalized with vinyl groups by using VTMS. The schematized reaction is represented in Figure 5.10.

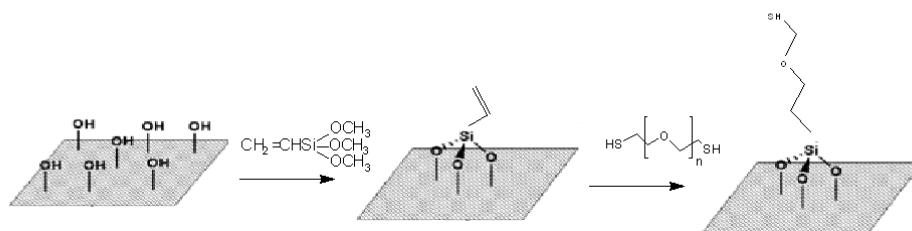


Figure 5.10: Schematic representation of the vinyl functionalization of magnetite surface and subsequent PEG-coating via thiol-ene reaction.

Modified magnetite nanoparticles were characterized by ATR spectroscopy as can be seen in Figure 5.11. The ATR-FTIR spectra are reported for respectively the bare Fe_3O_4 nanoparticles (spectra a) and for vinyl functionalized Fe_3O_4 nanoparticles (spectra b).

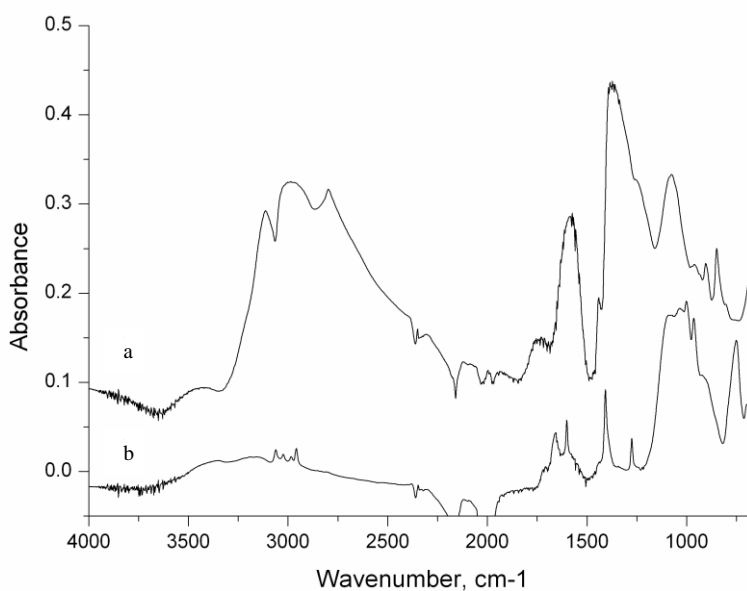


Figure 5.11: ATR-FTIR spectra of bared Fe_3O_4 (spectra a) and vinyl modified Fe_3O_4 (spectra b) nanoparticles.

In spectra b it can be seen that the strong and broad peak centered at around 3100 cm^{-1} disappeared, while a double peak centered at around 1600 cm^{-1} appeared after reactive functionalization of the nanoparticles. The disappearance of the peak centered at 3100 cm^{-1} can be attributed to the consumption of the hydroxyl groups present on the surface of Fe_3O_4 nanoparticles, during the silanization reaction, while the appearance of the double peak centered at 1600 cm^{-1} can be attributed to the vinyl groups present on the nanoparticles surfaces after reaction with VTMS (see the reaction scheme of Figure 5.10).

The achieved vinyl functionalized magnetite nanoparticles were coated with PEG-SH by UV-activation in water under nitrogen inlet. It is well known that under UV-light thiol groups can generate thyl radicals which are highly reactive towards C=C double bonds. The thiol-ene reaction is particularly interesting because it has all the desirable features of a “click” reaction, being highly efficient, simple to execute with no side products and proceeding rapidly to high yield. The UV-induced thiol-ene reaction is a free-radical process that proceeds by a step-growth mechanism, involving two main steps, a free-radical addition followed by a chain transfer reaction [11][12]. The UV activation of PEG-dithiol will allow to coat the vinyl functionalized Fe_3O_4 nanoparticles with a PEG shell.

The DLS measurements after coating the vinyl- Fe_3O_4 nanoparticles with PEG-SH showed an average size of nanoparticles of about 60 nm (see DLS curves b Figure 5.9). The increased size is due to the formation of the polymeric shell around the particles.

In order to confirm the polymer coating onto the surface of Fe_3O_4 particles via thiol-ene photochemical reaction, FT-IR spectra were recorded on dried samples. In Figure 5.12 the FT-IR spectra of coated magnetite nanoparticles is reported.

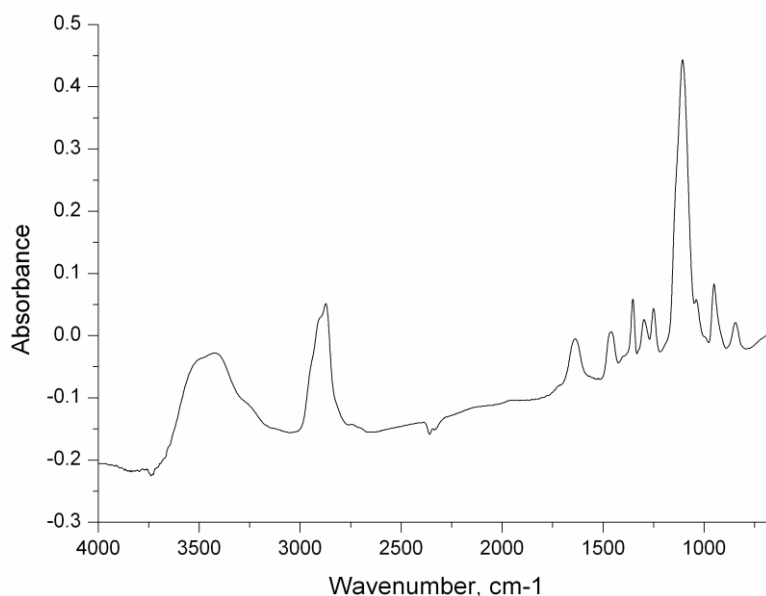


Figure 5.12: FT-IR of dried PEG-coated magnetite nanoparticles.

It can be assigned a strong absorption peak of stretching vibrations of ether bonds at 1100 cm^{-1} . Absorbent peaks were also evident at 2900 cm^{-1} belonging to asymmetric stretching vibration and scissoring bending vibration of CH_2 aliphatic groups. All these peaks are in accordance with the presence of a PEG shell around the magnetite particles. Furthermore the typical double peak centered at around 1600 cm^{-1} , which was previously observed on vinyl functionalized nanoparticles (Figure 5.11, spectra b), disappeared indicating the complete conversion of double bonds, due to the thiol addition. The broad peak centered at around 3500 cm^{-1} is due to the presence of water trace in the dried sample.

The TEM micrographs for magnetite coated particles are reported in Figure 5.13.

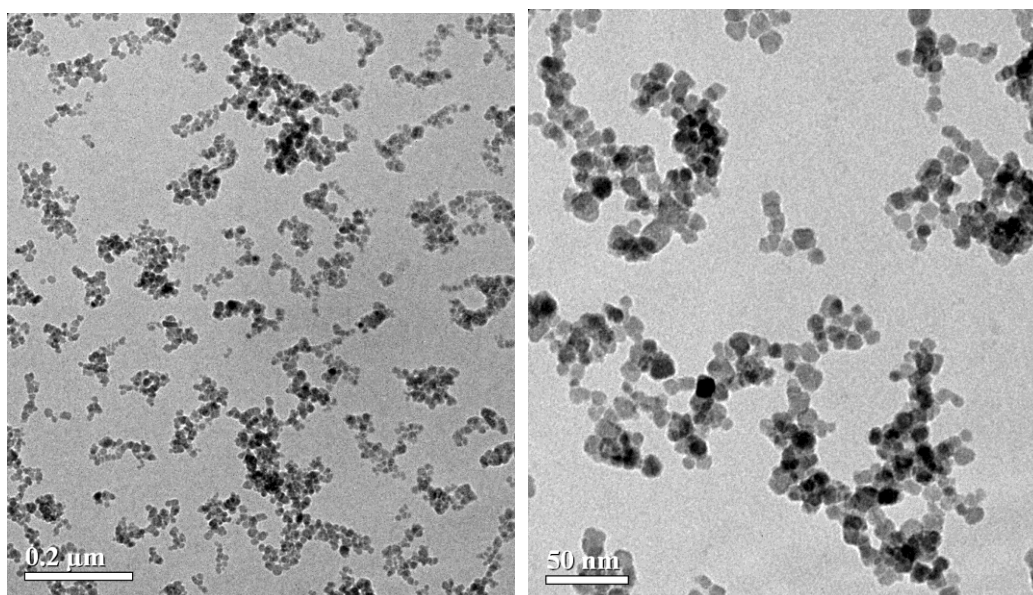


Figure 5.13: TEM micrograph for aqueous dispersion of the PEG-coated Fe_3O_4 nanoparticles

It is possible to observe that the single particles are in the nanometric size range with an average size of about 20-50 nm, they are well dispersed and they do not show strong tendency of microscopic aggregation. The TEM investigation is quite in a good agreement with DLS analyses which shows that by vinyl functionalization and following PEG coating it was possible to achieve nanometric size particles well distributed and not-aggregated.

Coating the Fe_3O_4 particles with PEG endowed the particles with excellent biocompatibility and hydrophilicity, which is a mandatory request for medical applications.

The degree of functionalization of the magnetite particles was evaluated through TGA analysis. The TGA curves for the PEG-coated Fe_3O_4 particles are reported in Figure 5.14, depicting the variation of residual masses of the samples with temperature.

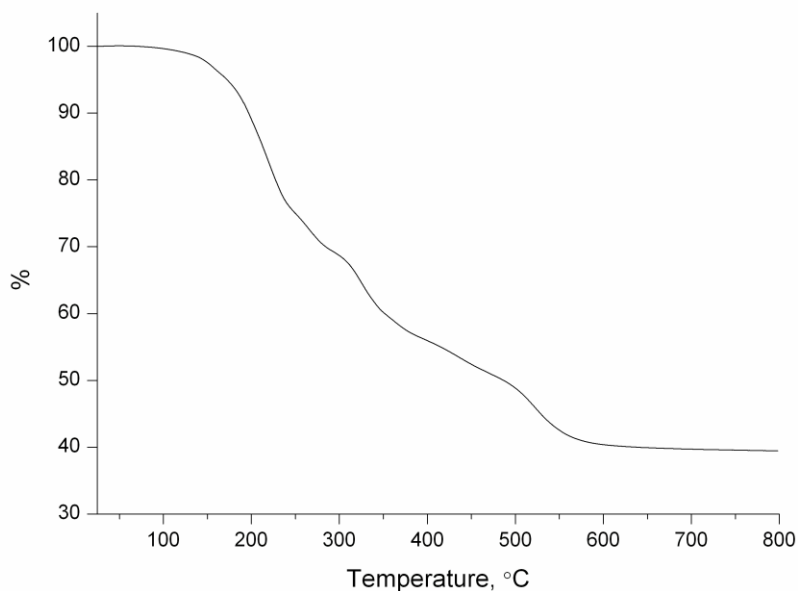


Figure 5.14: TGA curves of the PEG-coated Fe₃O₄ nanoparticles

The main weight loss stage occurred at around 225 °C and can be attributed to the PEG decomposition. This curve indicated that the magnetite content was about 40%, with a PEG-shell content which was calculated to be around 60% of the total weight.

The magnetization curve of the ferrofluid containing bare magnetite nanoparticles is shown in Figure 5.15.

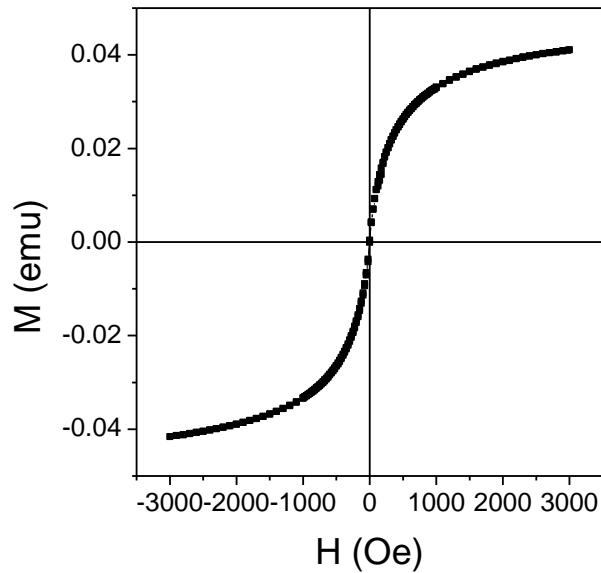


Figure 5.15: Room-temperature magnetization curve of the ferrofluid containing bare Fe_3O_4 nanoparticles

The curve exhibits superparamagnetic-like features (slow approach to saturation, absence of hysteresis) in spite of the rather large NP size. In fact, a simple calculation shows that almost spherical magnetite NPs of average size 30 nm (and volume $V \cong 1.4 \times 10^{-17} \text{ cm}^3$) are in the blocked state at room temperature, the blocking temperature being $T_B \cong 410 \text{ K}$, as is obtained from the usual expression $T_B = K_A V / 25k_B$ when the value of the magnetic anisotropy constant K_A is taken equal to that of bulk magnetite, $|K_A| = 1 \times 10^5 \text{ erg/cm}^3$, as appropriate to these nanoparticles [13][14]. Therefore, the superparamagnetic-like behavior is to be attributed to the fact that magnetic moments are affected by Brownian motion of the nanoparticles in a ferrofluid. A simple calculation shows that for a spherical nanoparticle of volume V the Debye relaxation time for rotation of NPs dissolved in water, $\tau = 3\eta V / k_B T$ [15], is of the order of 10 μs at room temperature, i.e. much shorter than the measurement time. As a consequence these NPs appear to be in a superparamagnetic state although their magnetization is blocked along an easy direction, because they are submitted to fast, random rotations of their crystallographic axes.

The magnetization curves of the ferrofluid containing coated Fe_3O_4 nanoparticles are shown in Figure 5.16a, b before and after subtraction of a strong diamagnetic signal which survives after subtraction of diamagnetic contributions from sample holder and solvent. Such a signal is ascribed to the polymeric shell surrounding the NPs.

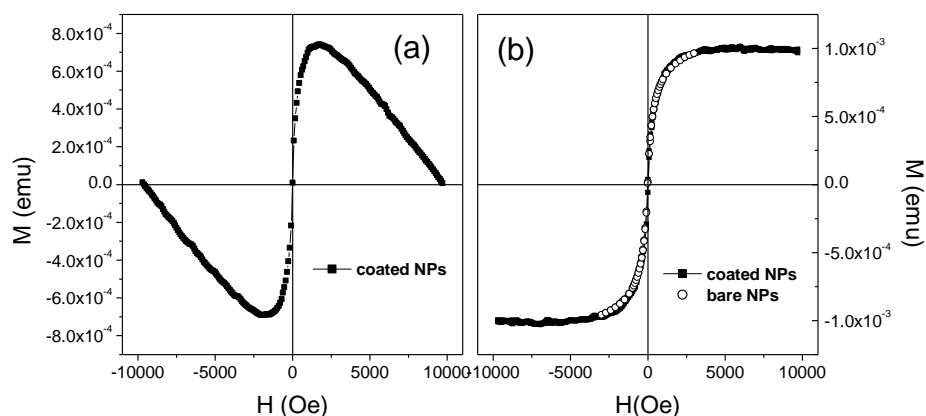


Figure 5.16: (■): room-temperature magnetization curves of the ferrofluid containing coated Fe_3O_4 nanoparticles; (a): before subtraction of diamagnetic from polymer coating; (b): after subtraction. (○) in (b): ferrofluid containing bare nanoparticles.

Again, the curve exhibits no detectable hysteresis in spite of the rather large NP size, for the reasons discussed above (although the larger volume of coated NPs entails a larger Debye relaxation time, this remains well below the measurement time). The symbols (○) in Figure 5.16b, which are exactly superimposed to the curve for coated NPs, refer to the bare nanoparticles, showing that their magnetic response is definitely not modified by polymeric coating.

Conclusions

Magnetite nanoparticles were synthesized by a chemical co-precipitation of Fe^{2+} and Fe^{3+} ions under alkaline conditions. The magnetization curves showed superparamagnetic property (i.e. no remanence effect) of the bare particles and relatively high magnetization values. DLS measurements showed an average size of Fe_3O_4 particles of about 30 nm. The achieved magnetite nanoparticles

were functionalized with vinyl groups by using VTMS, and they were further functionalized via thiol-ene reaction with PEG-SH under UV-activation. The DLS measurements after coating the vinyl-Fe₃O₄ nanoparticles with PEG-SH showed an average size of nanoparticles of about 60 nm. FT-IR analyses of the particles confirmed the presence of a PEG shell around the magnetite particles. The TEM micrographs for magnetite coated particles show that the single particles are nanometric size range with an average size of about 20-50 nm, they are well dispersed and they do not show strong tendency of microscopic aggregation. The degree of functionalization of the magnetite particles was evaluated through TGA analysis showing a PEG-shell content which was calculated to be around 60%.

Superparamagnetic-like behavior of coated Fe₃O₄ nanoparticles, which is typically looked after in biomedical applications, is ensured by the Brownian motion of magnetic NPs in the ferrofluid. Polymeric coating does not modify the magnetic response of the magnetite nanoparticles.

5.3 Polymer grafting onto magnetite nanoparticles via click-reaction

In this work, we aim to show the use of “click chemistry” for the preparation of magnetite-core/polymer-shell NPs. The overall strategy, as presented in Figure 5.17, is based firstly on the preparation of bromine-functionalized magnetite NPs, and then after azidation, the NPs are functionalized via click-reaction either with PCL or PEG polymeric shells.

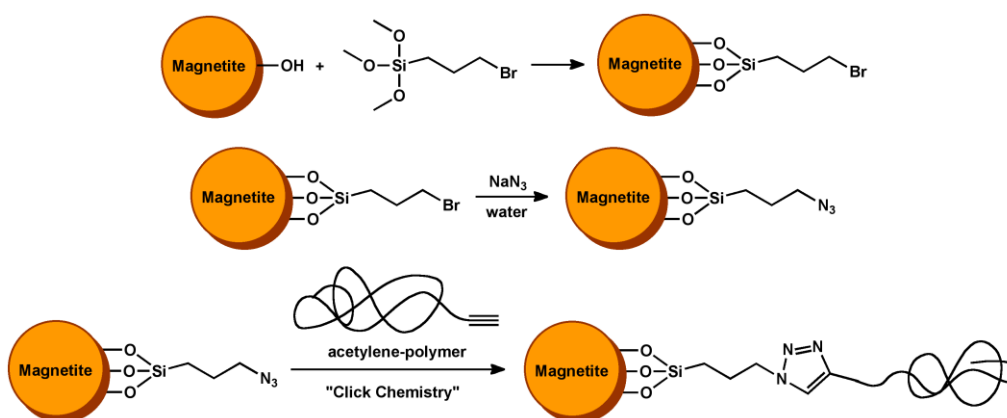


Figure 5.17: overall strategy of magnetite functionalization via „click“ reaction

Magnetite NPs were synthesized by a chemical co-precipitation of Fe^{2+} and Fe^{3+} ions under alkaline conditions, following previous method reported in literature [16][17][18][19][20][21]. Citric acid was added during the synthesis in order to protect the NPs avoiding macroscopic aggregations.

The magnetite NPs, prepared with the co-precipitation method, were functionalized with bromine groups by using 3-(bromopropyl)trimethoxysilane (see Figure 5.17). Modified magnetite NPs were characterized by FTIR spectroscopy. In Figure 5.18, the FTIR spectra are reported for respectively bare Fe_3O_4 NPs and bromine functionalized Fe_3O_4 NPs.

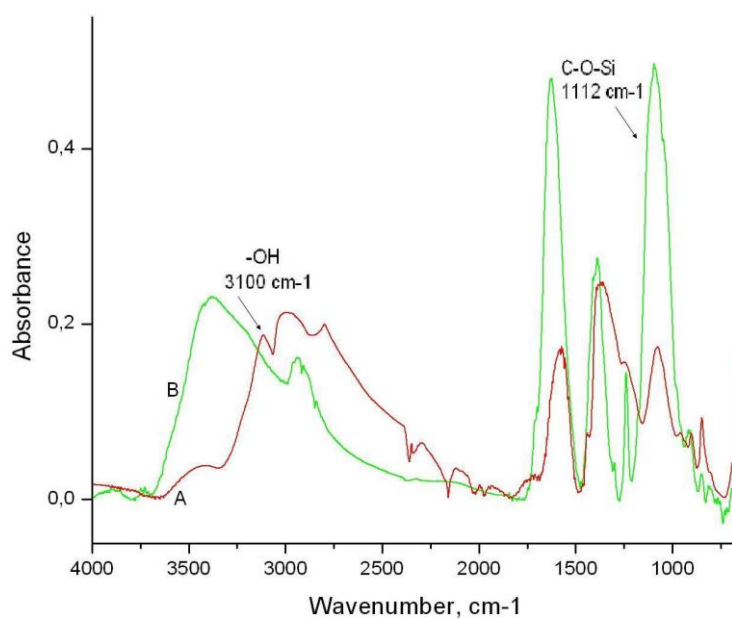


Figure 5.18: IR spectra of bare magnetite nanoparticles (A) and bromine functionalized nanoparticles (B).

In spectrum B, it can be seen that the strong and broad peak centered at around 3100 cm^{-1} disappeared, while a peak centered at around 1112 cm^{-1} appeared after reactive functionalization of the NPs. The disappearance of the peak centered at 3100 cm^{-1} can be attributed to the consumption of the hydroxyl groups present on the surface of Fe_3O_4 NPs, during the silanization reaction, while the appearance of the peak centered at 1112 cm^{-1} can be attributed to the C-O-Si stretching band.

The bromine-functionalized magnetite NPs were used as the starting point for “click” modification by conversion to an azide-functional surface through nucleophilic substitution. As a matter of fact the nanoparticles were azidated by reaction of the bromine groups with sodium azide. The successful azidation was confirmed by ATR spectrum. In Figure 5.19 the IR spectra of both bromine functionalized NPs and azide functionalized NPs are reported (A) with a zoom on the azide peak region (B).

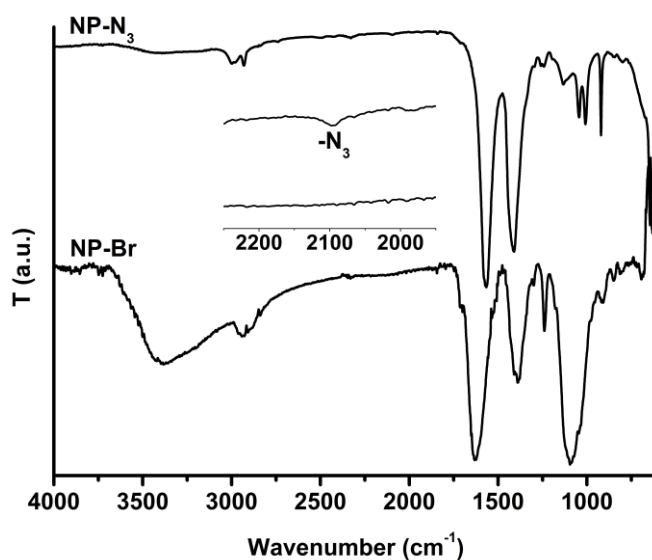


Figure 5.19: Confrontation of the magnetic nanoparticles IR spectra before and after azidation (A), zoom on the azide peak region (B).

The azidation of the NPs was confirmed by the appearance of the peak centered at 2100 cm^{-1} characteristic of the azide group.

For the subsequent click modification, alkyne-PCL and alkyne-PEG was synthesized as described in the experimental part.

In particular the alkyne-PCL (a-PCL) was prepared by Ring Opening Polymerization of ϵ -CL in bulk using tin(II) 2-ethylhexanoate as a catalyst and 4-pentyn-1-ol as an initiator, illustrated in Figure 4.3. The alkyne PCL was further characterized by ATR spectroscopy.

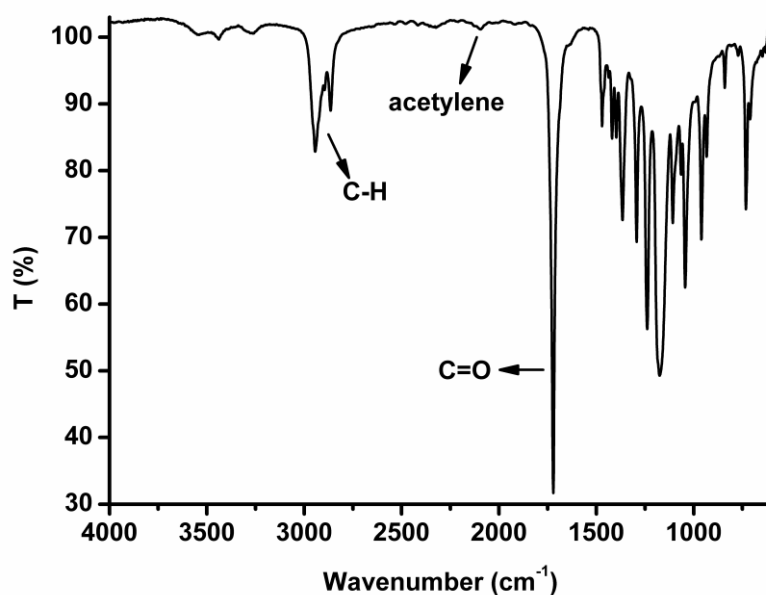


Figure 5.20: spectrum of the a-PCL.

As can be seen in Figure 5.20, the successful synthesis of alkyne PCL was confirmed by the alkyne stretching band around 2150 cm^{-1} and the typical bands of PCL such as C=O stretching at 1730 cm^{-1} , asymmetric C-O-C stretching at 1241 cm^{-1} or C-C stretching at 1047 cm^{-1} .

Regarding the alkyne-PEG (a-PEG), it was synthesized by the etherification reaction between 4-pentynoic acid and monohydroxyl functional PEG in CH_2Cl_2 (reaction scheme illustrated in Figure 4.4). The a-PEG was further characterized by ATR spectroscopy.

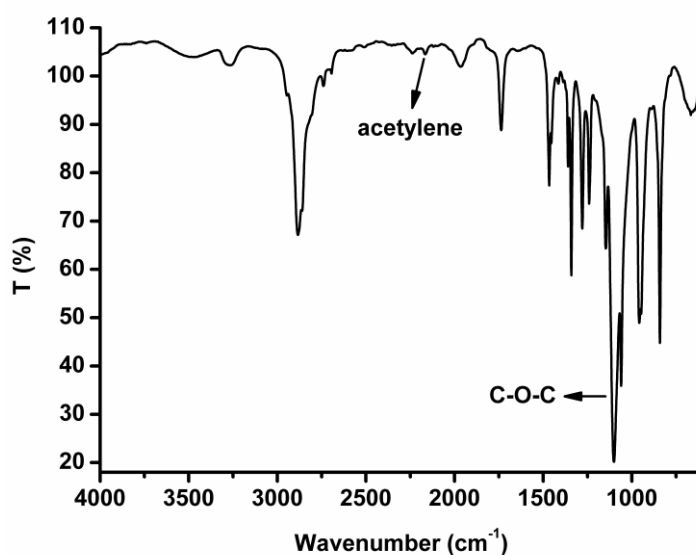


Figure 5.21: spectrum of a-PEG.

As can be seen in Figure 5.21, the successful synthesis of a-PEG was confirmed by the alkyne stretching band around 2150 cm^{-1} and the typical bands of PEG such as -COC vibration around 1010 cm^{-1} and out-of-plane bending of the -CH of the chain at 960 cm^{-1} .

The polymer functionalized NPs were characterized by ATR spectroscopy. In Figure 5.22 are reported the spectra of a-PCL and a-PCL functionalized magnetic NPs.

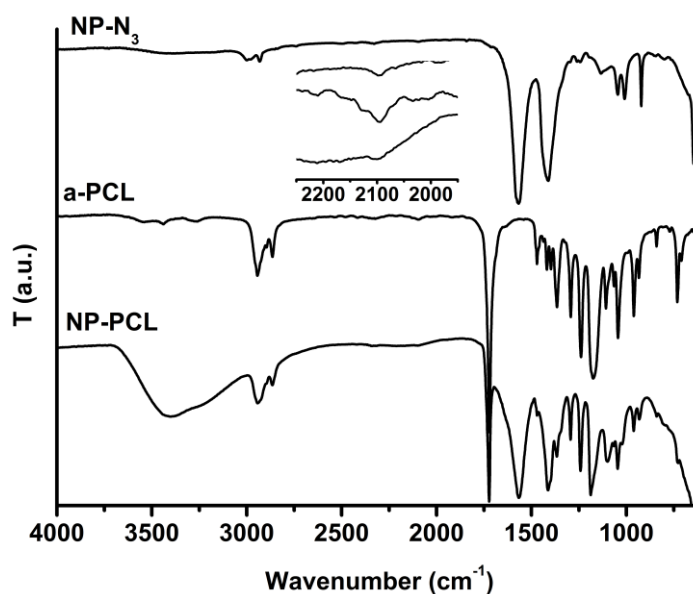


Figure 5.22: spectrum of the a-PCL (A) and of the PCL functionalized nanoparticles (B).

As can be seen from the spectrum, the alkyne peak around 2150 cm^{-1} respectively disappeared confirming the reaction between the azide group and the alkyne group. The functionalization is further confirmed by the presence of the typical peaks of PCL such as C=O stretching at 1730 cm^{-1} , asymmetric C-O-C stretching at 1241 cm^{-1} or C-C stretching at 1047 cm^{-1} and the disappearance of the alkyne stretching band at 2100 cm^{-1} .

The degree of functionalization of the magnetite particles was evaluated through TGA analysis. The TGA curve for the PCL-coated Fe_3O_4 particles is reported in Figure 5.23, depicting the variation of residual masses of the samples with temperature.

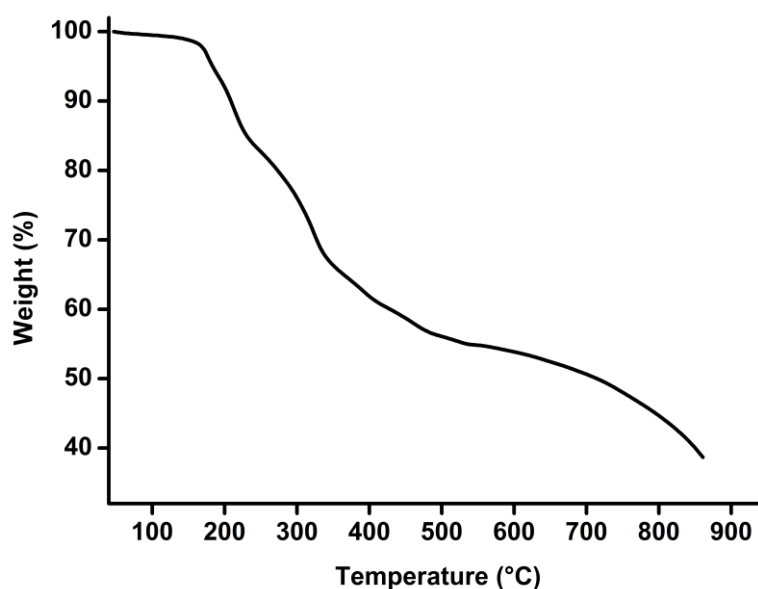


Figure 5.23: TGA of PCL functionalized magnetic nanoparticles.

The main weight loss stage occurred at around $200\text{ }^{\circ}\text{C}$ can be attributed to the PCL decomposition. This curve indicated that the magnetite content was about 40%, with a PCL-shell content which was calculated to be around 60% of the total weight.

In Figure 5.24 is reported the ATR spectrum of a-PEG functionalized NPs.

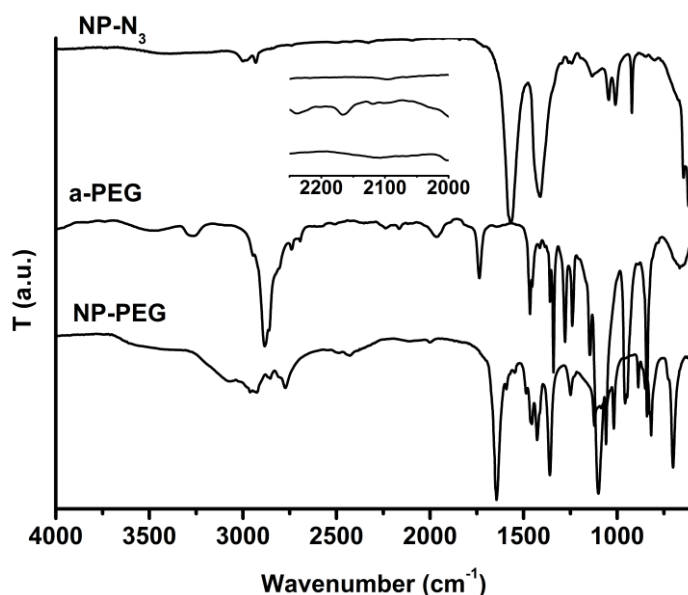


Figure 5.24: spectrum of PEG functionalized magnetite nanoparticles.

As can be seen on the spectrum the alkyne peak around 2150 cm^{-1} disappeared confirming the reaction between the azide group and the alkyne group. The functionalization is further confirmed by the presence of the typical peaks of PEG such as -COC vibration around 1010 cm^{-1} and out-of-plane bending of the -CH of the chain at 960 cm^{-1} .

The degree of functionalization of the magnetite particles was evaluated through TGA analysis. The TGA curve for the PEG-coated Fe_3O_4 particles is reported in Figure 5.25, illustrating the variation of residual masses of the samples with temperature.

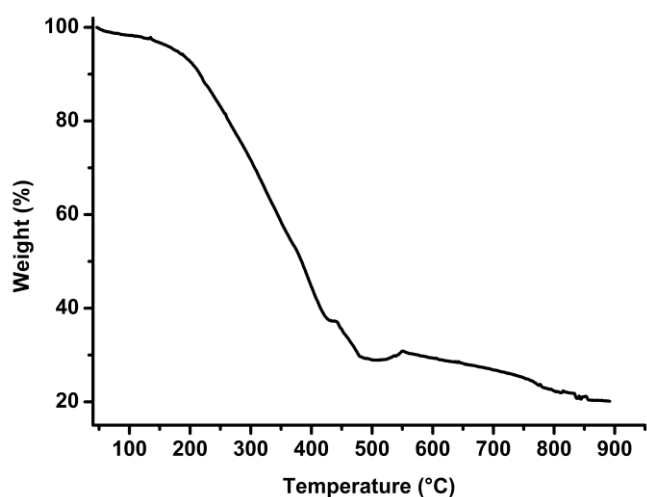


Figure 5.25: of PEG functionalized magnetite nanoparticles

The main weight loss stage occurred at around 225 °C and can be attributed to the PEG decomposition. This curve indicated that the magnetite content was about 20%, with a PEG-shell content which was calculated to be around 80% of the total weight.

Magnetization curves of PCL functionalized NPs and PEG functionalized NPs are reported respectively in Figure 5.26 and Figure 5.27.

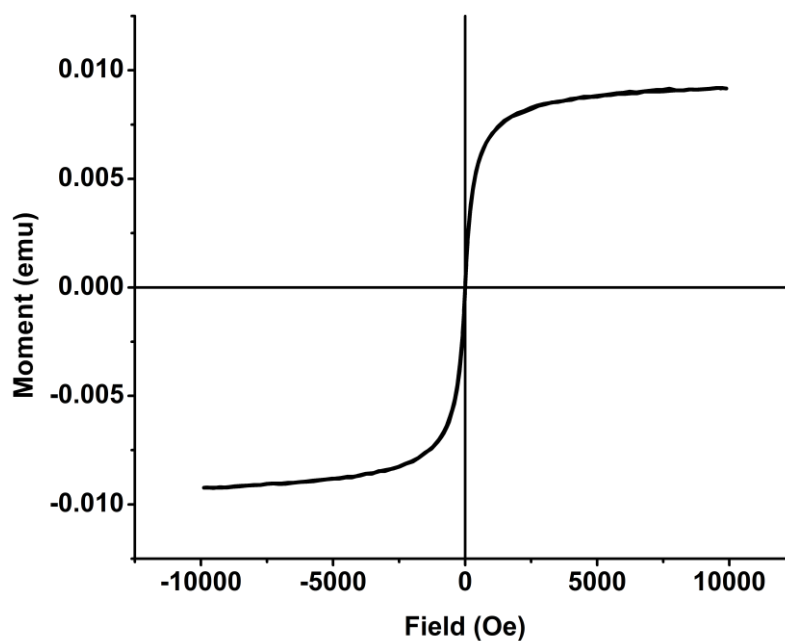


Figure 5.26: Magnetization curve of PCL coated magnetite nanoparticles

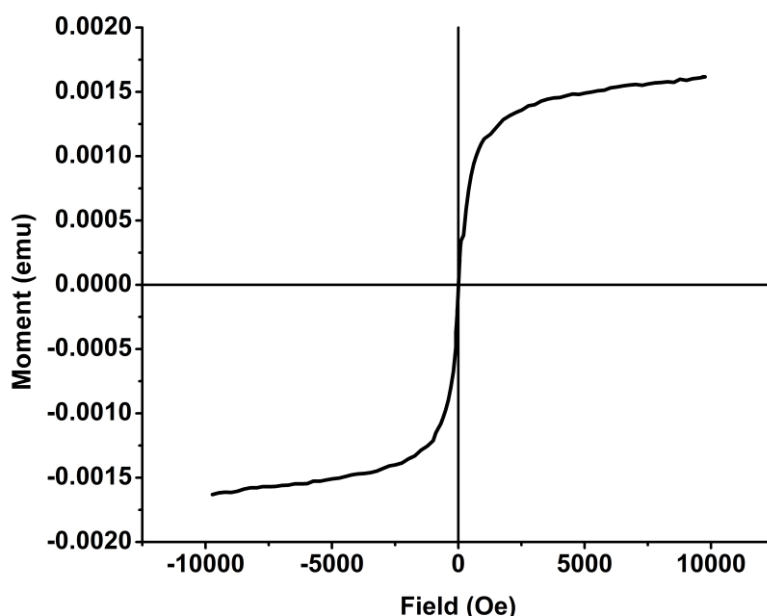


Figure 5.27: Magnetization curve of PEG coated magnetite nanoparticles

In both cases the hysteresis loop shows neither remanence nor coercivity, this confirms the fact that the polymer coated NPs have a superparamagnetic behavior and are, for this reason, suitable for biomedical applications.

The morphology of the coated NPs in aqueous solution has been investigated with TEM after transferring the aqueous solution to carbon coated copper grids. Figure 5.28 shows TEM micrograph of PCL coated NPs.

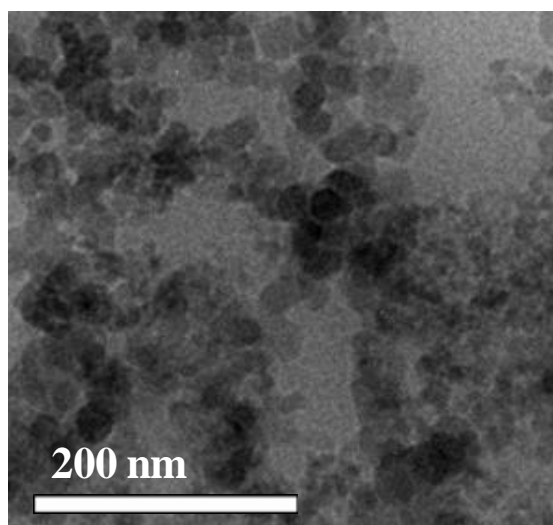


Figure 5.28: TEM micrograph for aqueous dispersion of the PCL-coated Fe_3O_4 nanoparticles

Figure 5.29 shows TEM micrograph of PEG coated NPs .

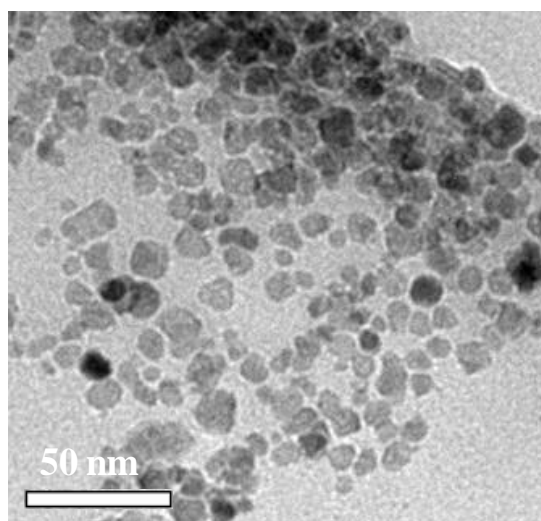


Figure 5.29: TEM micrograph for aqueous dispersion of the PEG-coated Fe_3O_4 nanoparticles.

The presence of aggregates may be due to the water droplet evaporation during TEM analysis. However, it is possible to observe that for both samples the single particles are in the nanometric size range with an average size of ranging between 20 and 50 nm. The TEM investigation shows that by functionalization via click reaction it was possible to achieve nanometric size particles which can be suitable for their magnetic properties to biomedical applications.

Conclusions

Magnetite nanoparticles (NPs) were functionalized with bromine groups using (3-Bromopropyl)trimethoxysilane, bromine groups were then substituted with azide groups using sodium azide. Successively the NPs were coated with a-PEG and a-PCL via click reaction, reacting alkyne groups of the polymers with azide groups on the surface of NPs. ATR analysis confirmed the presence of a polymeric shell in both cases. The degree of functionalization of the magnetite particles was evaluated through TGA analysis showing a PCL-shell content which was calculated to be around 60% and a PEG-shell content which was calculated to be around 80%. The analysis of the magnetization curves show that the NPs have a superparamagnetic behavior which is one of the most important requirements for intravenous administration in bio-medical

application. TEM analysis confirmed the nanometric size the narrow size distribution of the coated NPs. Moreover, coating the Fe₃O₄ particles with PEG and PCL endowed the particles with excellent biocompatibility and hydrophilicity, which is a mandatory request for medical applications.

References

- [1] Dilnawaz F., Singh A., Mohanty C., Sahoo S. K., *Biomaterials*, **2010**, 31, 3694-3706.
- [2] Hoffman A.J., Yee H., Mills G., Hoffmann M.R., *J. Phys. Chem.*, **1992**, 96, 5540-5547.
- [3] M. Sangermano, L. Vescovo, N. Pepino, L. Suber, G. Marchigiani, P. Allia, P. Tiberto, M. Coisson, *Macro. Chem. and Phys.*, **2010**, 211, 2530-2535.
- [4] De Giglio E., Cometa S., Cioffi N., Torsi L., Sabbatici L., *Anal. Bioanal. Chem.*, **2007**, 389, 2055-2063.
- [5] Zhiya M., Huizhou L., *Chin. Partic.*, **2007**, 5, 1-10.
- [6] Stella B., Arpicco S., Peracchia M. T., Desmaele D., Hoebeke J., Renoir M., D'Angelo J., Cattel L., Couvreur P., *J. Pharm. Sci.*, **2000**, 89, 1452-1464.
- [7] Zablotskaya A., Segal I., Maiorov M., Zablotsky D., Mishnev A., Lukevics E., Shestakova I., Domracheva I., *J. Magn. Magn. Mater.*, **2007**, 311, 135-139.
- [8] Mondini S., Cenedese S., Marinoni G., Molteni G., Santo N., Bianchi C. L., Ponti A., *J. Coll. Interf. Sci.*, **2008**, 322, 173-179.
- [9] Hyeon T., *Chem. Commun.*, **2003**, 8, 927.
- [10] Lee Y., Lee J., Jin Bae C., Park J., Noh H., Park J., Hyeon T., *Adv. Funct. Mater.*, **2005**, 15, 503-509.
- [11] C. Hoyle, Tai Yeon Lee, T. Roper, *J. Polym. Sci. Part A: Polym Chem*, **2004**, 42, 5301-5338.
- [12] N. B. Cramer, C. N. Bowman, *J. Polym. Sci. Polym. Chem.*, **2001**, 39,

3311.

- [13] Cullity B.D., *Introduction to Magnetic Materials*, Addison-Wesley, Reading, **1972**.
- [14] Allia P., Tiberto P., Coisson M., Chiolerio A., Celegato F., Vinai F., Sangermano M., Suber L., Marchegiani G., *J. Nanop. Res.* **2011**, 13, 5615-5626.
- [15] Debye P., *Polar Molecules*, Dover Publications, New York, **1945**.
- [16] Zhiya M., Huizhou L., *Chin. Partic.*, **2007**, 5, 1-10.
- [17] B. Stella, S. Arpicco, M. T. Peracchia, D. Desmaele, J. Hoebeke, M. Renoir, J. D'Angelo, L. Cattel, P. Couvreur, *J. Pharm. Sci.*, **2000**, 89, 1452-1464.
- [18] A. Zablotskaya, I. Segal, M. Maiorov, D. Zablotsky, A. Mishnev, E. Lukevics, I. Shestakova, I. Domracheva, *J. Magn. Magn. Mater.*, **2007**, 311, 135-139.
- [19] S. Mondini, S. Cenedese, G. Marinoni, G. Molteni, N. Santo, C. L. Bianchi, A. Ponti, *J. Coll. Interf. Sci.*, **2008**, 322, 173-179.
- [20] T. Hyeon, *Chem. Commun.*, **2003**, 8, 927.
- [21] Y. Lee, J. Lee, C. Jin Bae, J. Park, H. Noh, J. Park, T. Hyeon, *Adv. Funct. Mater.*, **2005**, 15, 503-509.

6. Photothermal therapy

6.1 Photochemical synthesis of gold-PEG core-shell nanoparticles

Gold-PEGDA core shell particles were prepared in water by adapting the method developed by our groups [1][2] in which gold nanoparticles were *in situ* generated from HAuCl_4 as precursor in the presence of a radical photoinitiator. It is well known that microcapsule formation can be achieved by photochemical means in water-acrylic emulsion [3]. In our work, free-emulsifier emulsion polymerization is performed by using PEGDA as hydrophilic monomer. It is expected that PEG nanospheres would be formed by UV-induced polymerization after adding the acrylic resin into water in dropwise manner. The nanospheres formed this way could integrate the gold precursor and generate gold nanoparticles by a reduction process occurring within the PEGDA droplets. The overall process is schematically represented in Figure 6.1.

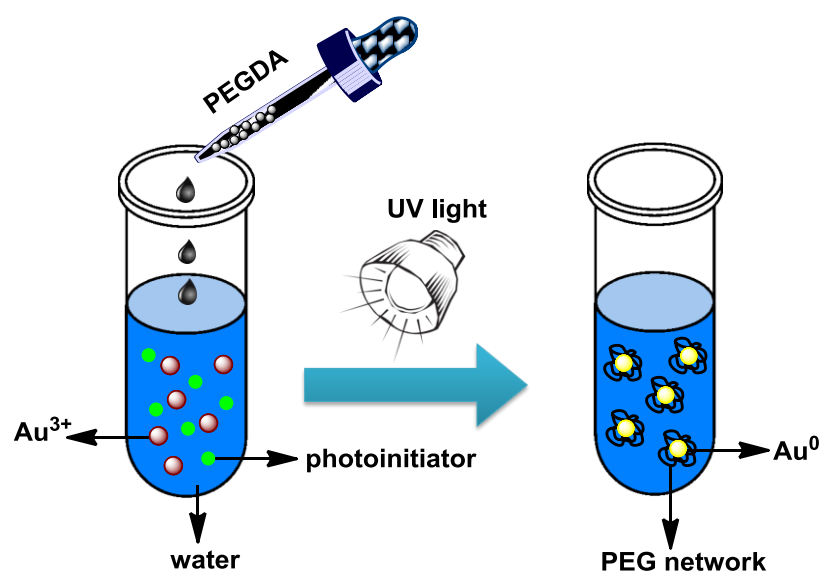


Figure 6.1: Photochemical synthesis of gold-PEG core-shell nanoparticles

Accordingly, the synthesis was conducted in a three-necked flask in which gold precursor and radical photoinitiator were previously added to a large amount of

water. While the acrylic resin was added dropwise, the UV irradiation was turned on. Different formulations were investigated using different photoinitiator content in the range between 2 to 6 wt% with respect to the amount of acrylic resin added to the water dispersion. During UV irradiation the solution turns from yellow to purple, indicating successful gold reduction. The photopolymerization process was investigated by real-time FT-IR analysis by plotting conversion curves as a function of irradiation time. In this analysis, while the plateau value gives the final acrylic double bond conversion, the slope of the curve corresponds to the polymerization rate. In Figure 6.2, the real time FT-IR kinetic curves for the different formulations containing increasing amount of radical photoinitiator are reported.

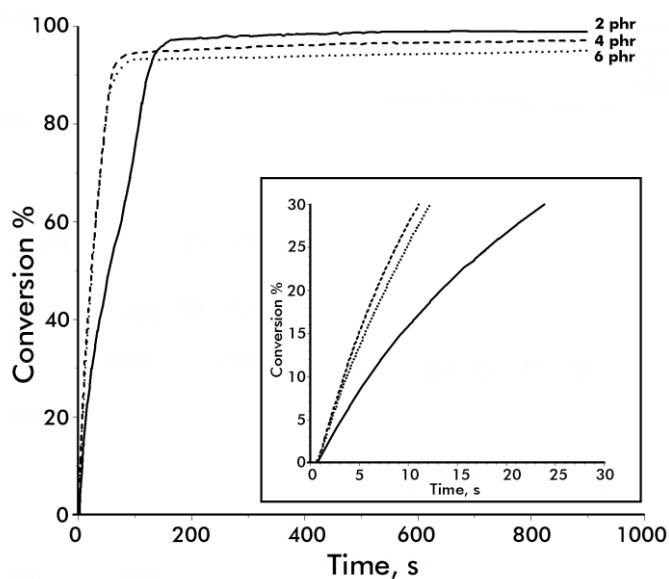


Figure 6.2: Conversion curves as a function of irradiation time for PEGDA/HAuCl₄ water dispersion containing the radical photoinitiator at 2 (-) 4 (- -) or 6 (··) wt% with respect to the PEGDA resin.

By increasing the photoinitiator concentration, an increase in the photopolymerization rate was observed. It should be noted that regardless of the photoinitiator concentration, an almost complete acrylic double bond conversion is achieved after few minutes of irradiation in all cases. In the batch system, where curing occurred in a very dilute PEGDA in water dispersion, the

curing time was prolonged for 30 minutes in order to assure complete acrylic double bond conversion in the shells around the gold particles.

Dynamic light scattering curves are reported in Figure 6.3 for the different water dispersion.

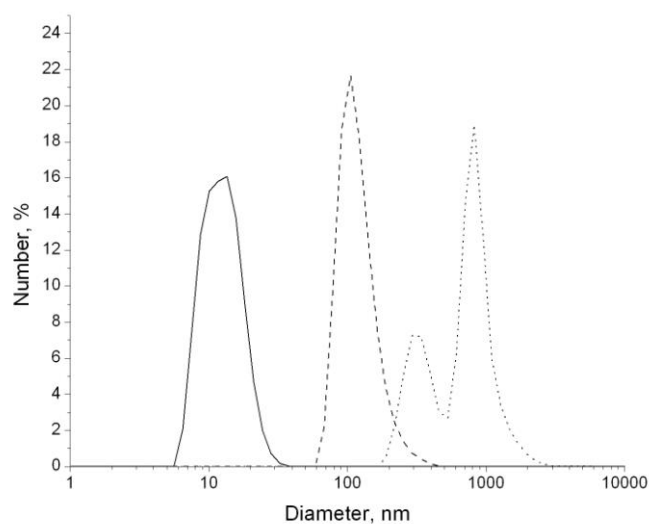


Figure 6.3: Size distribution obtained by DLS measurements of the water gold-PEGDA core-shell nanoparticles obtained from water formulations containing the radical photoinitiator at 2 (-) 4 (- -) or 6 (···) wt% with respect to the PEGDA resin

It is noted that the particles size increases by increasing the photoinitiator content. When 2 wt% radical photoinitiator is employed, rather homogenously distributed nanometric size particles are obtained. However, by increasing the photoinitiator content to 4 wt%, the average size is still nanometric but with larger dimension. Finally, when the photoinitiator content is increased up to 6 wt%, the particles formed are not in the nanometric size range anymore. The observed increase on particle dimension could be attributed to an increase of the acrylic thickness shell around the gold nanoparticles due to the larger concentration of active radicals available for PEGDA polymerization.

The morphology of the coated gold particles in aqueous solution has been investigated with TEM after transferring the aqueous solution to carbon coated copper grids. Figure 6.4 shows TEM micrograph for the formulations containing 2 wt% of radical photoinitiator.

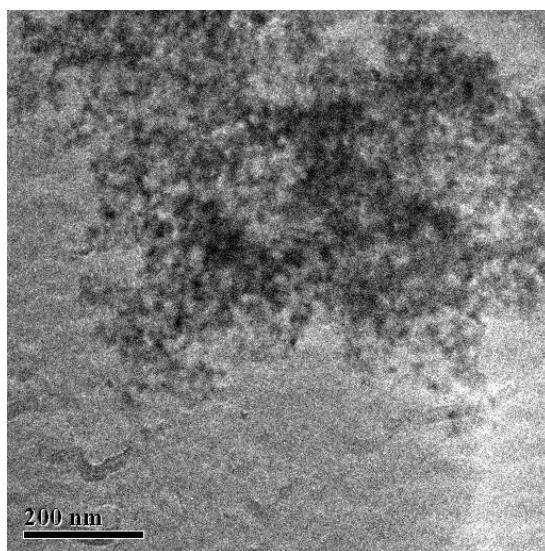


Figure 6.4: TEM micrograph of the gold/PEGDA core-shell nanoparticles obtained from the water formulations containing 2 wt% of radical photoinitiator. The aqueous solution was transferred to carbon coated copper grids

The presence of large aggregates formed by single particles of the average size within 10 to 50 nm is in a good agreement with the DLS analyses. The large aggregate may be due to the water droplet evaporation during TEM analysis: evaporation results in the increase in the concentration. As a consequence the number density and distance of the particles increase leading to the formation of large clusters.

In order to confirm the coating of PEGDA on the surface of gold particles by the described photochemical route, ATR spectra were recorded on dried samples. The ATR spectra of the gold-PEGDA core-shell nanoparticles obtained from the solution containing 2 wt% of radical photoinitiator is reported in Figure 6.5.

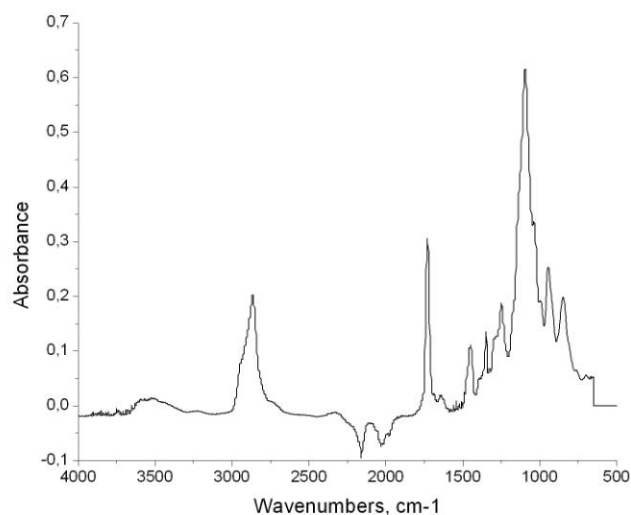


Figure 6.5: ATR spectrum of the of the dried gold/PEGDA core-shell nanoparticles obtained from the water formulations containing 2 wt% of radical photoinitiator.

The strong peak centred at 1700 cm^{-1} was attributed to the stretching vibration of the ester groups. Absorption bands of stretching vibrations of ether bond appeared at 1100 cm^{-1} . Absorbent peaks were also evident at 2900 cm^{-1} belonging to asymmetric stretching vibration and scissoring bending vibration of CH_2 aliphatic groups. All these peaks revealed the existence of PEGDA coating on the gold particles.

The gold nanoparticles functionalization was further confirmed by XPS analysis. XPS measurements allow determining the surface composition of functionalized gold particles. The XPS measurements were performed on gold-PEGDA core-shell nanoparticles obtained from the solution containing 2 wt % of radical photoinitiator.

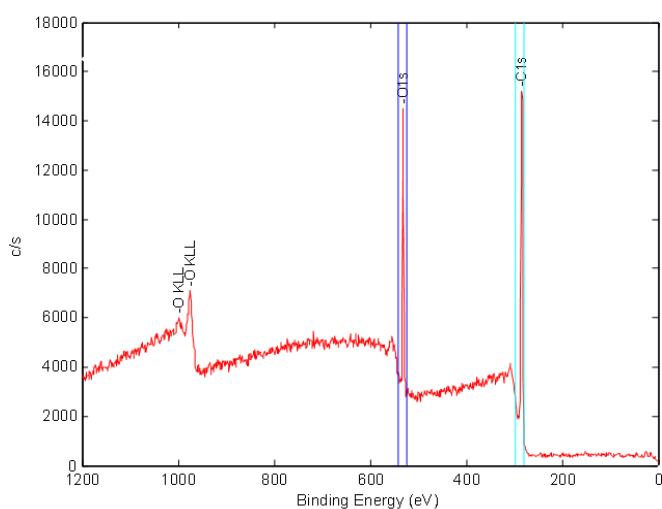


Figure 6.6: High resolution XPS spectra of survey spectra performed on gold-PEGDA core-shell nanoparticles obtained from the solution containing 2 wt% of radical photoinitiator.

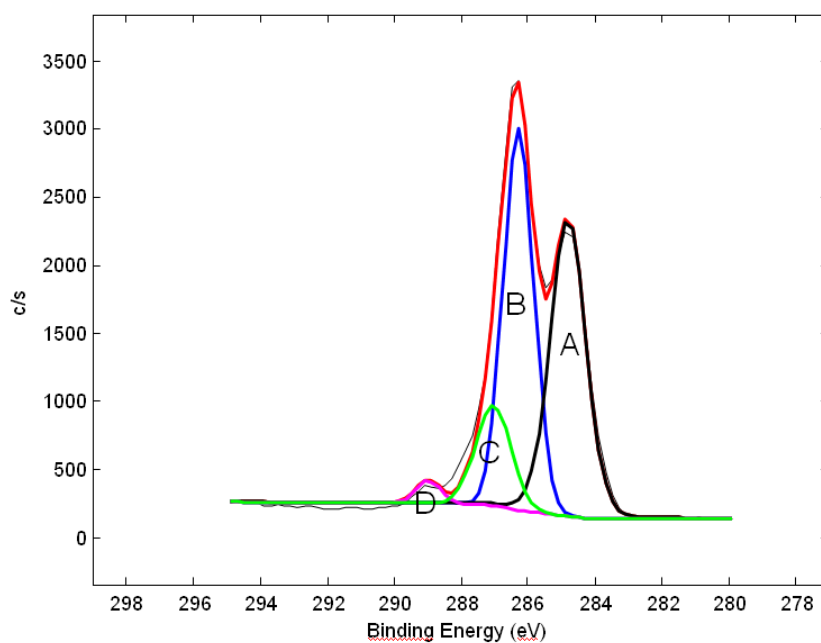


Figure 6.7: High resolution XPS spectra of C 1s of gold-PEGDA core-shell nanoparticles obtained from the solution containing 2 wt% of radical photoinitiator

In the survey scan (Figure 6.6), O1s signal in the 523-543 eV region, C1s signal in the 228-298 eV region was evidenced. , However, Au 4f, in the (80-

98 eV) region was not detected. This finding is a clear evidence of the fact that the PEGDA shell around the gold nanoparticles is at least 5 nm thick (as discussed in paragraph 5.1). In the high resolution spectra of C1s region (Figure 6.7), fitted with four components and related atomic percentage, were reported. The same information with relative atomic percentage was depicted in Table 6.1.

Table 6.1: XPS attribution of the different signals recorded on dried gold-PEGDA core-shell structure. The reference shift was performed on C1s peak at 284.8 eV correspond to C-C signal.

Attribution	B.E. eV (PEGDA)	Atomic Percentage (%)
A C-C	284,79	41,24
B C-C(=O)OR	286,26	43,43
C COC	287,02	13,25
D C(=O)OR	288,98	2,08

The reference shift was performed on C1s peak at 284,8 eV corresponds to C-C signal [4]. The observed second peak at 286,26 eV is related to C-C(=O)OR labelled with B according to reference. The third shoulder, (labelled with C) corresponds to COC signal, and finally, the last component D could be related to C(=O)OR bound.

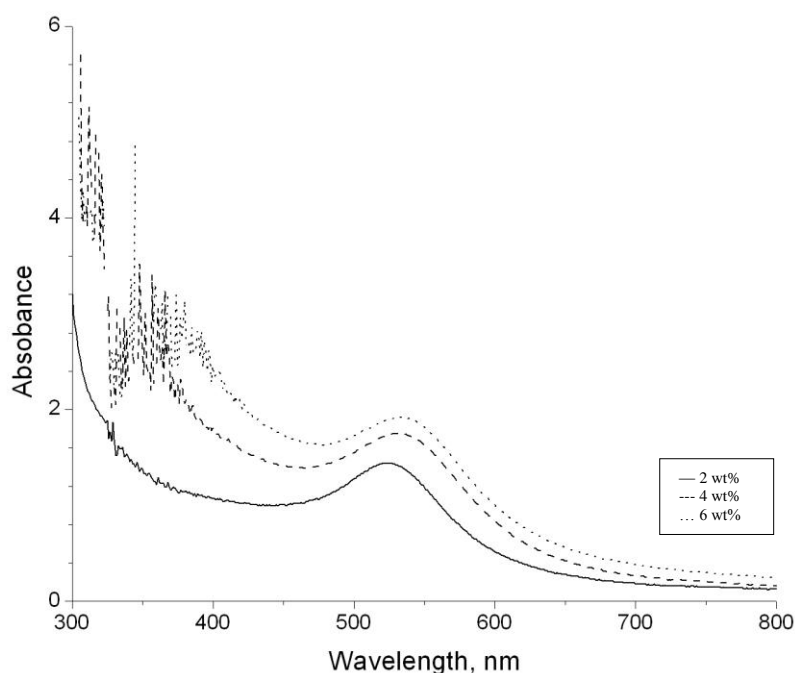


Figure 6.8: UV-vis spectra of the water gold-PEGDA core-shell nanoparticles obtained from water formulations containing the radical photoinitiator at 2 (-) 4 (- -) or 6 (···) wt% with respect to the PEGDA resin

In Figure 6.8 the UV-Vis spectrum of the water dispersions show the presence of a strong absorption peak centred at around 550 nm, which is close to the reported surface plasmon resonance for gold nanoparticles in solution [5]. The size and shape of metal nanoparticles determine the spectral position of plasmon band absorption. It is evident from the spectra reported in Figure 6.8, a slight shift of the maximum peak of the plasmon resonance toward infrared wavelength by increasing the amount of radical photoinitiator. This can be attributed to the increased thickness of the polymeric shell around the gold nanoparticles, as already evidenced by DLS analyses.

Conclusions

Gold-PEGDA core shell particles were prepared in water via a photoinduced electron transfer and free-radical polymerization of an acrylic formulation. DLS measurements reveal the achievement of nanometric size distribution of

the synthesized particles. The TEM micrographs showed that the particles are in the nanometre range, within 10 to 50 nm, which is in good agreement with the DLS analyses. ATR and XPS analyses confirmed the formation of PEGDA shell around the gold particles. All the identified IR peaks revealed the existence of PEGDA coating on the gold particles. The C1s peaks deconvolutions further evidence XPS signals from PEGDA, which overlap homogeneously Au nanoparticles. UV-vis spectra showed the presence of a surface plasmon resonance, which is a size-related electronic feature. Homogenous core-shell structured nanoparticles obtained this way are expected to find important applications in bio-medical fields.

6.2 Hollow-gold nanoparticles

The HGNs were prepared by adapting the method found in literature [6] in which the synthesis is based on templating using cobalt (Co) nanoparticles as initial seeds via a galvanic reaction with Au^{3+} ions. It is essential that the oxidation state of the seed metal ion (Co^{2+} in this case) be lower than that of the metal ion to be reduced (Au^{3+} here) [6]. Since the reduction potential of the $\text{AuCl}_4^-/\text{Au}$ redox couple (0,935 V vs SHE) is indeed much higher than that of the Co^{2+}/Co redox couple (- 0,377 V vs. SHE), AuCl_4^- will be reduced to Au atoms as soon as Co nanoparticles are added into the solution due to the big gap between the potential of these two redox couples. In addition, because the reduced gold atoms are largely confined to the vicinity of sacrificial template outer surface, the diameter of Co nanoparticles determines that of the resulting gold hollow nanostructures. Therefore, the fabrication of Co nanoparticles is a critical foundation in the whole preparation procedure [7]. The gold shell at its formation stage should have an incomplete porous structure so that Co^{2+} and HAuCl_4^- can continuously diffuse into the shell. The porous structure allows the remaining active Co “core” to be continuously oxidized to Co^{2+} by H^+ when there is not sufficient supply of HAuCl_4^- [7]. The overall process is represented in Figure 6.9

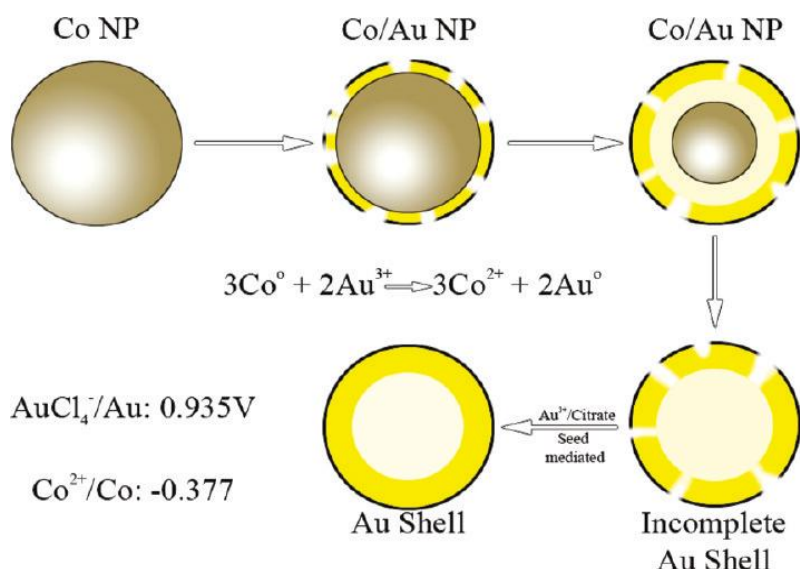


Figure 6.9: schematic representation of HGNs formation

The combination of shell diameter and thickness determines the peak position of the SPR absorption. Moreover, on the basis of theoretical calculation, the SPR bandwidth depends sensitively in the uniformity of the shell diameter and thickness, and poorer uniformity results in broader spectral width [6]. For these reasons we decided to realize different formulations to assess the relation between the surface plasmon resonance position and the morphology of the device. The results obtained are reported in Table 6.2 hereafter. The mean external and internal diameters have been measured on at least 100 TEM pictures.

Table 6.2: Effect of the variation of the reaction parameter on shell thickness and SPR localization

Sample Nber	Sod citrate μL	NaBH_4 μL	CoCl_2 μL	HAuCl_4 μL	Ext diam nm	Int diam nm	Max SPR nm
1	400	100	100	250	32,86	21,48	600
2	400	100	100	700	68,46	44,07	606
3	190	180	100	700	63,93	49,24	677
4	330	250	100	700	53,26	40,16	639
5	900	100	100	700	63,97	46,76	619
6	190	180	100	450	59,41	48,4	683
7	330	250	100	450	34,65	22,1	586
8	900	100	100	450	55,59	37,64	611

As can be seen from Table 6.2 varying the reaction parameters it is possible to obtain a wide range of internal and external diameters, hence a wide range of shell thicknesses. Namely, we obtained external diameters going from 32,86 nm to 68,46 nm and internal diameters going from 21,48 nm to 49,24 nm as can be seen in Figure 6.10.

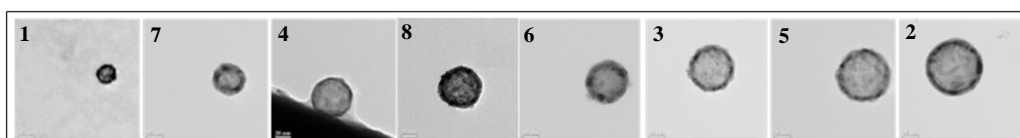


Figure 6.10: TEM images of HGNS samples

In this way we obtained SPR localized between 586 nm and 683 nm, into the near infrared region. However, looking at the absorbance spectra reported in Figure 6.11 it is possible to see that the shift of the absorbance peak, compared to the one of gold, is not directly correlated to the external diameter.

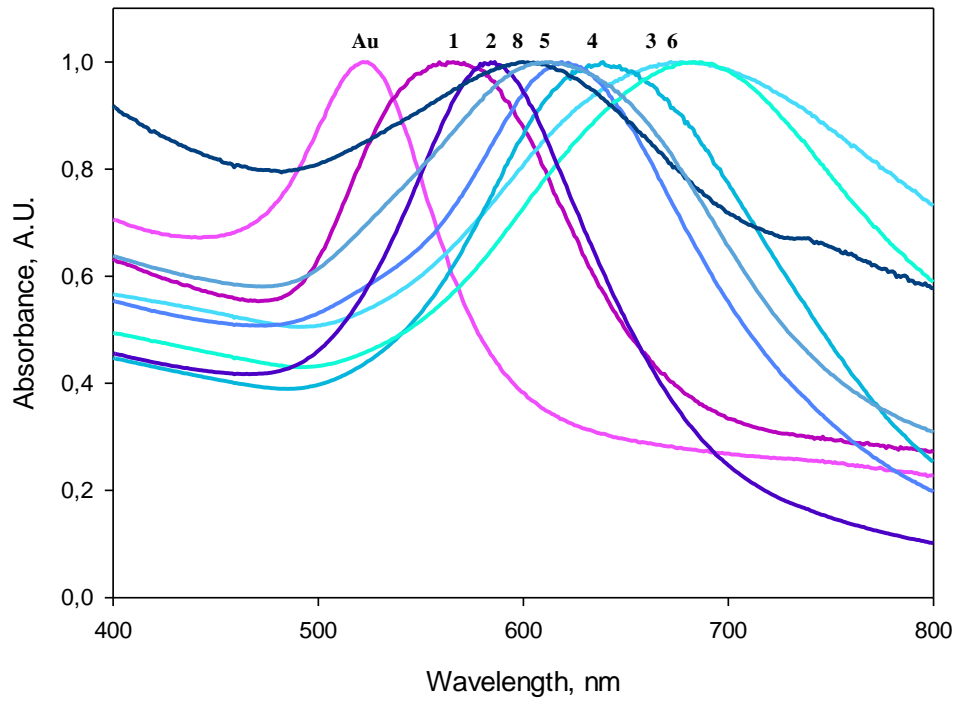


Figure 6.11: absorbance spectra of HGNS samples and 15 nm gold nanoparticles (Au)

Plotting the different data in our possession we eventually found the correlation between the localization of the SPR and the ratio between the external diameter and the internal diameter as can be seen on Figure 6.12.

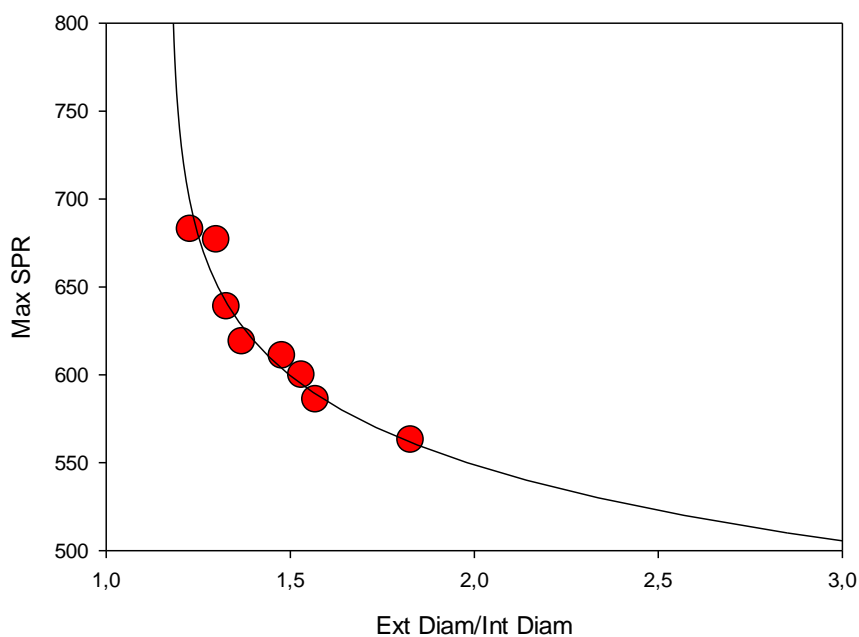


Figure 6.12: correlation between the SPR localization and the ratio external diameter on internal diameter

The relation between these 2 parameters is exponential, and the typical equation would be:

$$f(x)=y+ae^{-bx}$$

to our knowledge, it is the first time that such a correlation is found.

From an experimental point of view this means that there are 2 regimes: in the first one, when the ratio is superior to 1,2, little variation of this ratio leads to important shift of the SPR while, when the ratio is inferior to 1,2, the SPR shift is a lot more difficult to control by varying the ratio. Moreover, we can see that smaller is the ratio value more significant is the SPR shift toward NIR region.

In a second time, another sample was prepared, sample 9. The size and the morphology of the new nanoparticles were studied by TEM, the pictures are reported in Figure 6.13.

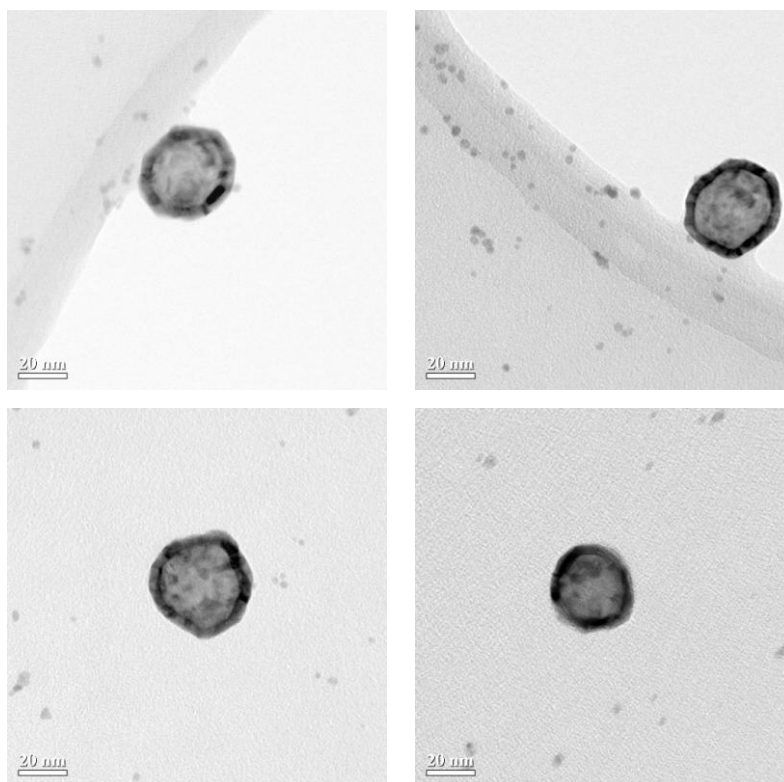


Figure 6.13: TEM pictures of Sample 9

The nanoparticles are nearly spherical and monodisperse. The external mean diameter is 51.1 ± 9.7 nm and the internal mean diameter is 30.2 ± 7.2 nm (mean diameters measured on 100 HGNS).

These nanoparticles were then coated with poly(ethylene glycol) methyl ether thiol using the affinity between thiol groups and gold. The nanoparticles size and granulometric distribution were studied by DLS analysis, the results are reported on Table 6.3.

Table 6.3: DLS analysis of bare and coated hollow gold nanoparticles

Sample Name	Z average (nm)	PDI
Bare nanoparticles	60.22	0.114
Coated nanoparticles	78.00	0.140

The DLS analysis demonstrates a mean diameter increase of about 18 nm while

the polydispersity index is not significantly changed, this confirm the successful coating of the nanoparticles. Moreover the absorbance of the 2 colloidal suspension was measured and the confronted in Figure 6.14.

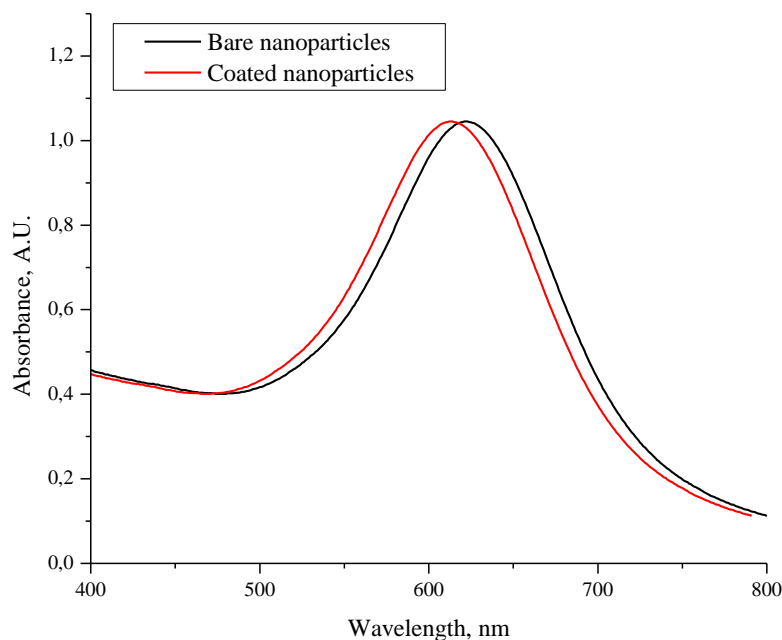


Figure 6.14: Uv-Vis spectra of bare nanoparticles (black) and coated nanoparticles (red)
The absorbance spectra of bare nanoparticles and coated nanoparticles are slightly shifted, the first one is at 623 nm and the second one at 614 nm.

Conclusions

Hollow gold nanoparticles were synthesized by reduction of gold salts on the surface of cobalt nanoparticles. By varying the reaction parameters we were able to obtain a wide range of diameters and shell thicknesses. In this way it was possible to study the shift of the surface plasmon resonance in function of the variation of these parameters. We found an exponential correlation between the ratio of the external diameter and the internal diameter and the surface plasmon resonance localization, to our knowledge this correlation has never been reported in literature. Moreover, we were able to coat hollow gold nanoparticles with a biocompatible polymer (PEG) in order to make them suitable for biomedical applications. This polymeric coating did not

significantly shift the SPR peak, leaving it in the NIR region which is compulsory for photothermal therapy.

6.3 *SiO₂@Au nanoshell*

Metal nanoshells are a class of interesting subwavelength photonic particles with highly tunable plasmonic properties. A perfect nanoshell is composed of a spherical dielectric core homogeneously coated with a concentric nanoscale metallic shell. The nanoshell plasmon resonance frequencies and lineshapes are strongly dependent on the relative ratio between core and shell dimensions, the overall size of nanoshells, and the dielectric properties of surrounding medium. Recent advances in the chemistry of molecular self assembly and surface modification of both dielectric and metal colloids have provided the essential elements that enables the immobilization of metal nanoparticles onto the surface of larger dielectric cores as described on Figure 6.15 [8][9][10][11][12].

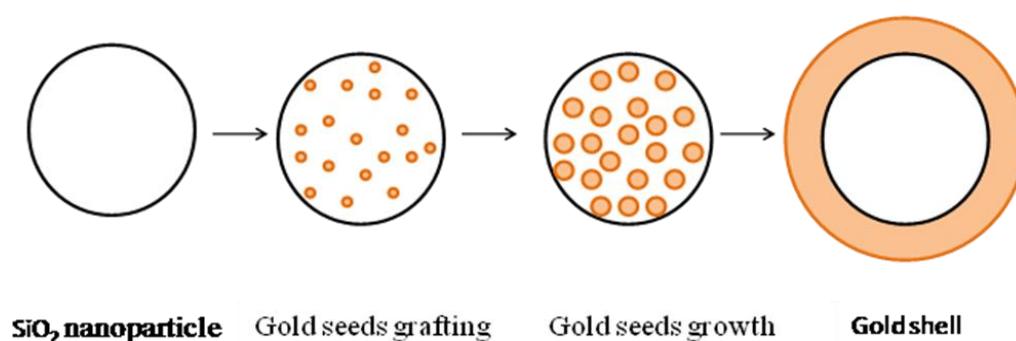


Figure 6.15: schematic representation of nanoshell formation

Spherical silica nanoparticles were grown following the well known method described by Stöber et al. [13]. Their size and morphology were studied by TEM and the pictures are reported on Figure 6.16.

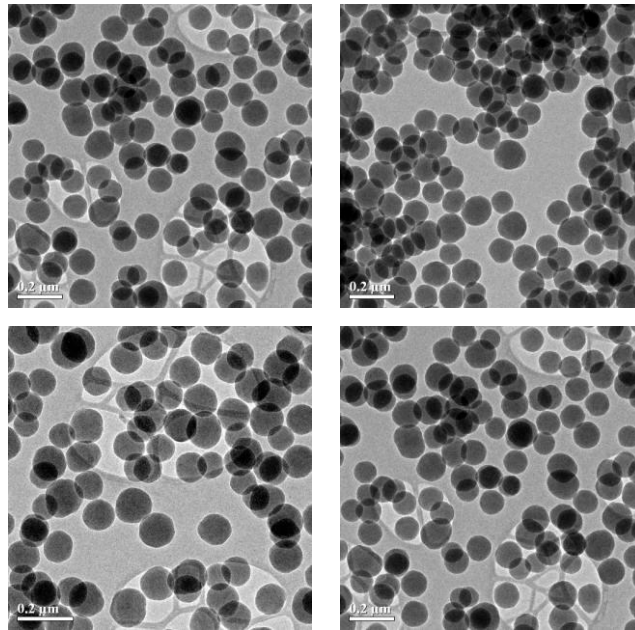


Figure 6.16: TEM pictures of SiO₂ nanoparticles

The nanoparticles obtained are spherical with a diameter of 110 nm and are fairly well dispersed.

Successively, the small gold nanoparticles (GNPs) were prepared by reduction of chloroauric acid with THPC as described by Duff et al. [15]. The mean diameter of GNPs nanoparticles was studied via DLS analysis the granulometric distribution can be seen on Figure 6.17.

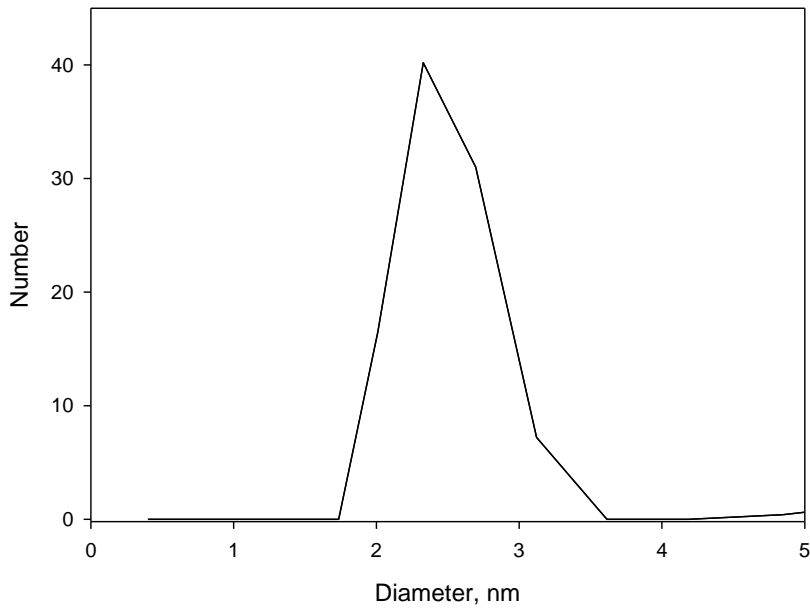


Figure 6.17: DLS analysis of GNPs

We can see that the mean diameter of the nanoparticles is around 4 nm and the size distribution is fairly narrow. The morphology of the nanoparticles was further studied by TEM (see Figure 6.18).

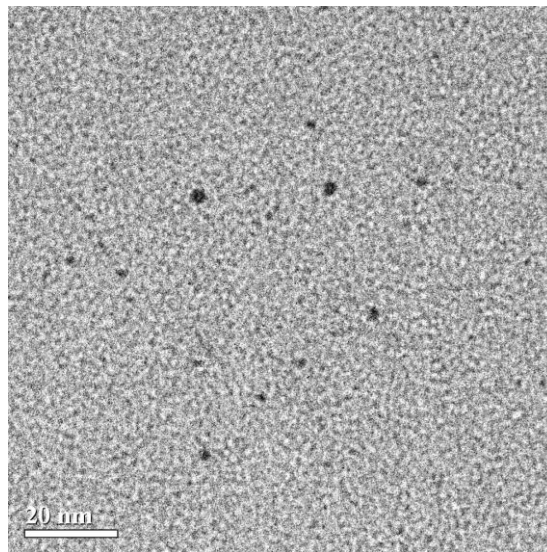


Figure 6.18: TEM picture of GNPs

The nanoparticles seem fairly dispersed and their diameter is in agreement with DLS analysis.

The attachment of the small GNPs on the surface of silica nanoparticles was carried out by functionalizing the silica nanoparticles with APTES and having these groups react with the surface of GNPs. The morphology of the nanoparticles was studied by TEM, the pictures can be seen on Figure 6.19.

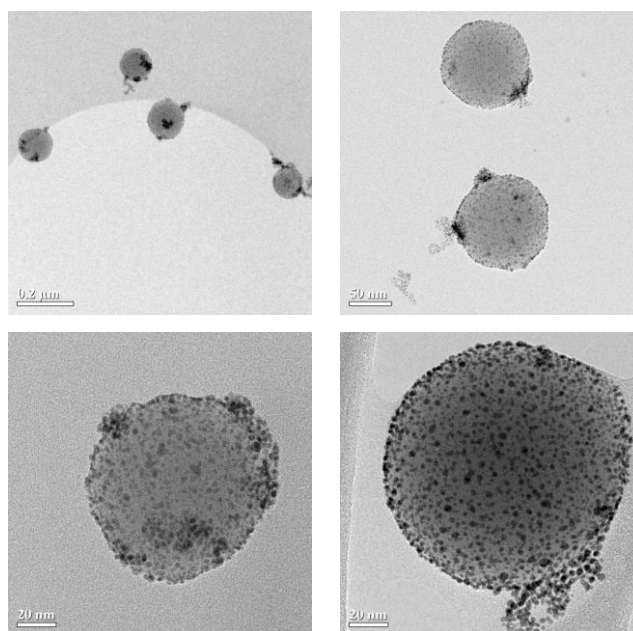


Figure 6.19: TEM pictures of SiO₂_APTES nanoparticles functionalized with GNPs

The size distribution of the nanoparticles is a little bit wider, between 110 and 170 nm. Moreover, the GNPs seem rather well dispersed on the nanoparticles surfaces. For the formation of the gold shell in the next reaction step, it is important that all non-attached GNPs are removed from the dispersion of the gold-functionalized silica nanoparticles.

The principal idea for the formation of the gold-shell is to grow the small GNPs attached to the silica nanoparticles surface larger by soft reduction of gold onto them. After some initial growth these gold particles begin to coalesce, and finally a continuous gold shell is formed. This shell may then be grown further to a thicker shell. To get well defined, uniform, and closed shells,

it is important that all small nanoclusters are growing simultaneously (not only the larger seeds) so that, after the clusters have grown a few nanometers, all clusters have coalesced and the resulting gold shell acquires a uniform thickness. On the other hand, it is important that the newly added gold ions are only reduced on the small gold nanoclusters attached on the gold shells. Besides growth on gold clusters in the solution, the new nucleation of gold nuclei should also be prevented.

The nanoshell diameter was studied by TEM analysis on an average of 100 nanoparticles for each sample and the surface plasmon resonance was obtained on a spectrophotometer.

The results obtained are reported in Table 6.4.

Table 6.4: Mean external diameter, mean internal diameter and SPR localization of samples Nanoshell 8 to Nanoshell 13

	Diam Ext	Diam Int	SPR
	nm	nm	nm
Nanoshell 8	176.2±14.4	115.3±5.9	552
Nanoshell 9	174.8±11.7	115.6±2.4	556
Nanoshell 10	159.1±14.5	114.9±3.9	554
Nanoshell 11	146.0±13.9	113.7±3.1	615
Nanoshell 12	161.2±13.5	113.6±3.5	556
Nanoshell 13	137.4±12.8	113.8±6.3	755

The TEM pictures of the different samples are reported hereafter in Figure 6.20, Figure 6.21, Figure 6.22, Figure 6.23, Figure 6.24 and Figure 6.25:

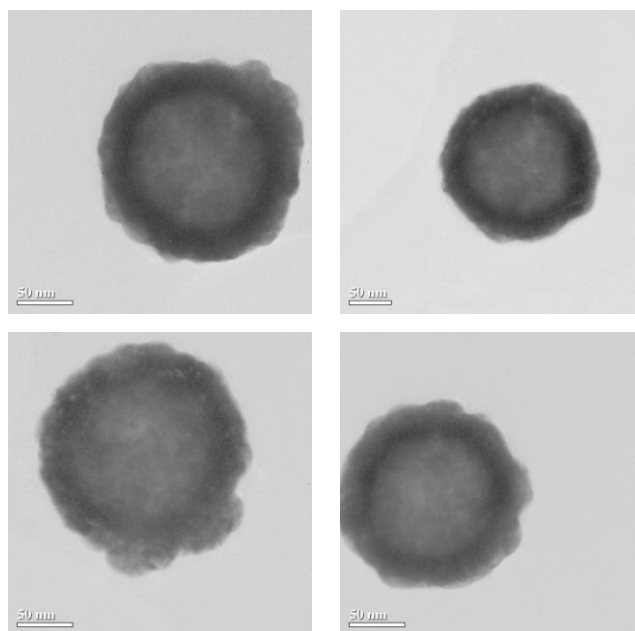


Figure 6.20: Nanoshell 8

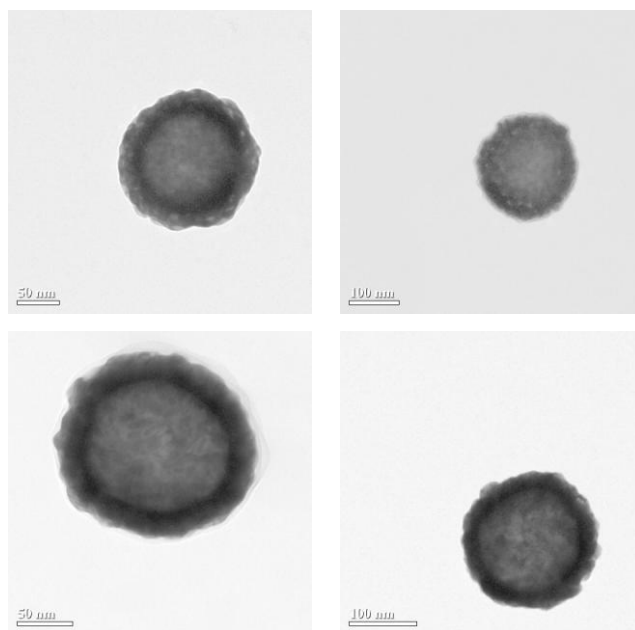


Figure 6.21: Nanoshell 9

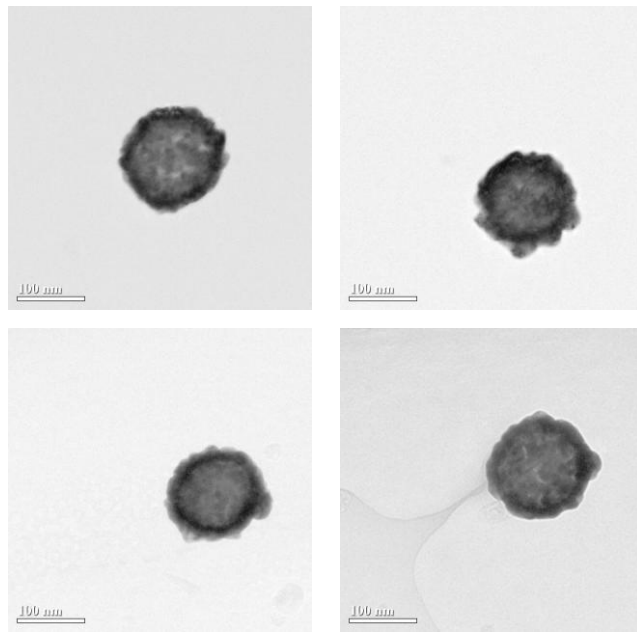


Figure 6.22: Nanoshell 10

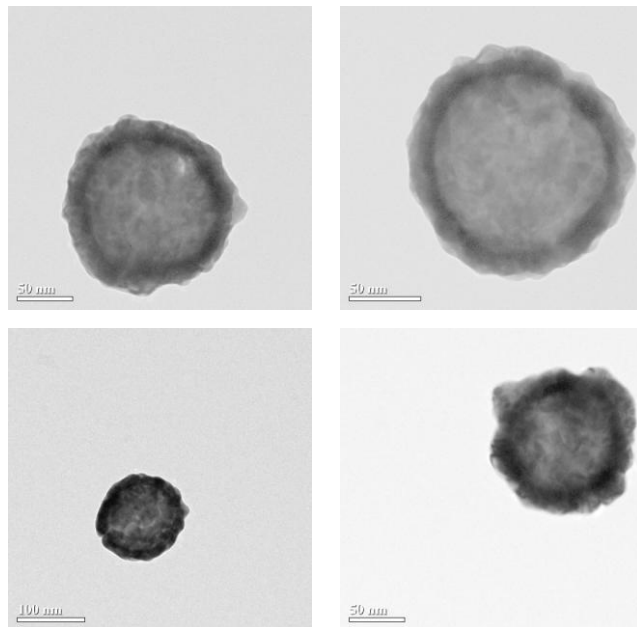


Figure 6.23: Nanoshell 11

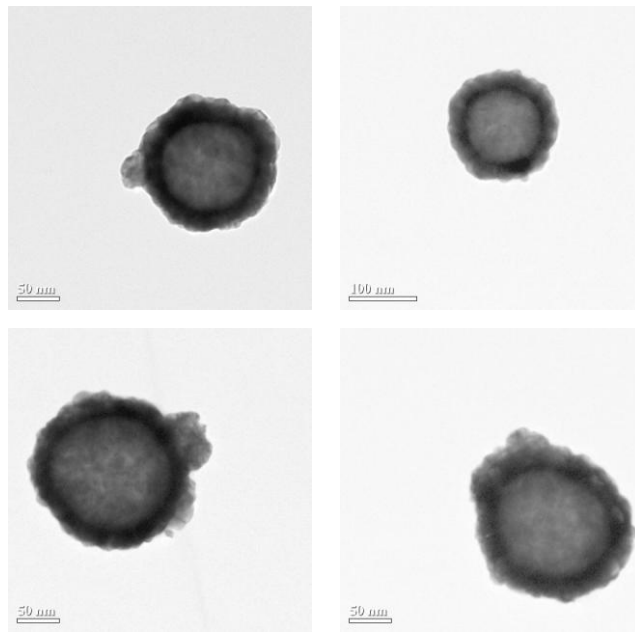


Figure 6.24: Nanoshell 12

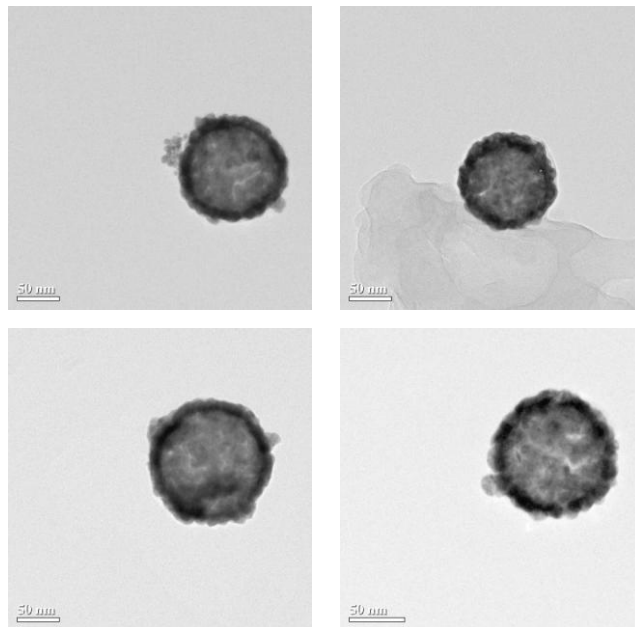


Figure 6.25: Nanoshell 13

We can clearly see that the internal diameter remains constant in all samples and consistent with the initial diameter of SiO_2 nanoparticles while the external diameter is varying with the volume of Kcarb solution added. This variation of the shell thickness leads to a shift of the surface plasmon resonance localization

as can be seen in Table 6.4. We plotted Figure 6.26 to understand the correlation between these 2 parameters.

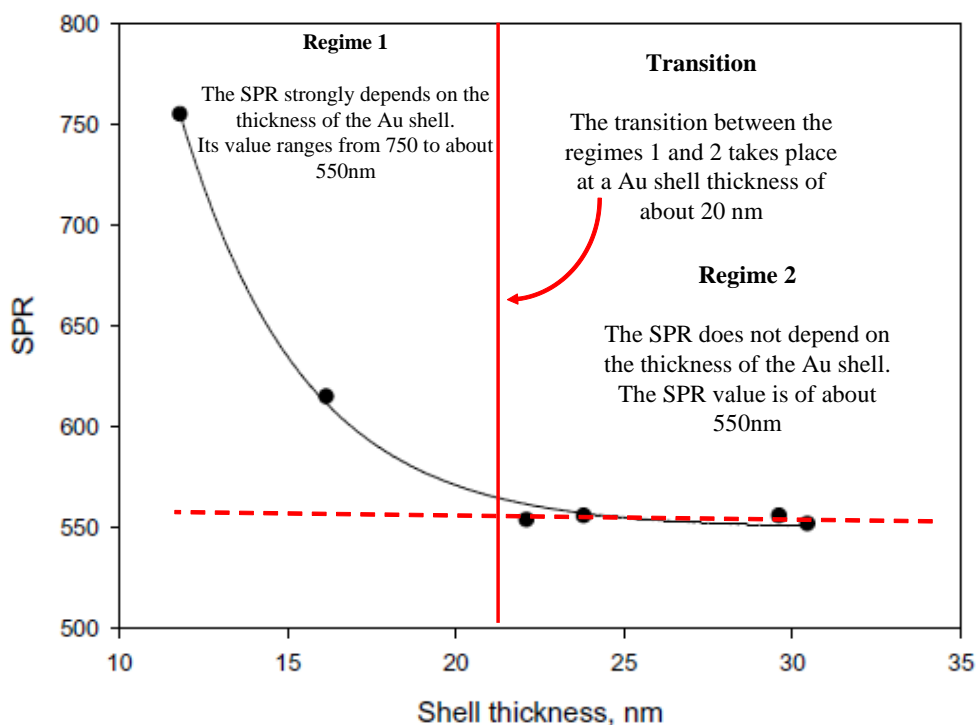


Figure 6.26: Surface Plasmon resonance localization in function of the gold shell thickness

On this figure we can see that the surface plasmon resonance localization depends strongly on the shell thickness, indeed there is an exponential correlation between these 2 parameters. Moreover, as reported on the graph, this correlation is composed by 2 different regimes. In the first one, for a shell thickness inferior to 20 nm, the SPR localization undergoes significant variation (from 550 nm to 750 nm), varying the shell thickness. In the second regime, for a shell thickness superior to 20 nm the SPR localization does not depend on the shell thickness anymore and is situated around 550 nm. To conclude, it was possible to shift the surface plasmon resonance of the nanoparticles to 750 nm, deep into the near infra-red, which is good for our application; however the external diameter of the nanoparticles is going from 136 nm to 177 nm hence too large for intravenous administration.

For this reason we decided trying to adapt the Stöber method to obtain smaller SiO₂ nanoparticles. More precisely, in this particular reaction ammonia is used as a catalyst, for this reason we decided to modify its concentration and check the effect on nanoparticles diameter.

The SiO₂ nanoparticles obtained this way were characterized by TEM (at least 100 nanoparticles were measured for each sample to determine the mean diameter), the results obtained are reported in Table 6.5 and in Figure 6.27:

Table 6.5: Diameter of the SiO₂ nanoparticles varying the NH₄OH concentration

	NH ₄ OH	Diam
	mL	nm
SiO ₂ NPs 5	1.7	27.64 ± 3.04
SiO ₂ NPs 6	2.0	36.94 ± 4.61
SiO ₂ NPs 7	2.3	51.33 ± 5.49
SiO ₂ NPs 8	2.6	65.36 ± 6.88

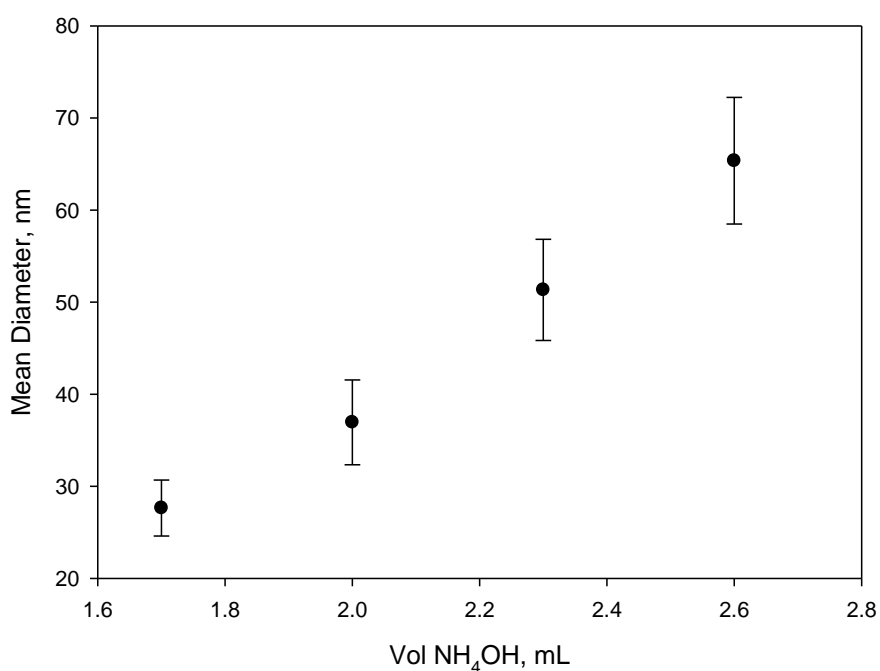


Figure 6.27: Variation of the SiO₂ nanoparticles diameter varying the NH₄OH concentration

We note that, as expected, the diameter of the SiO₂ nanoparticles increases, increasing the NH₄OH concentration. The TEM pictures of the samples are reported in Figure 6.28, Figure 6.29, Figure 6.30 and Figure 6.31.

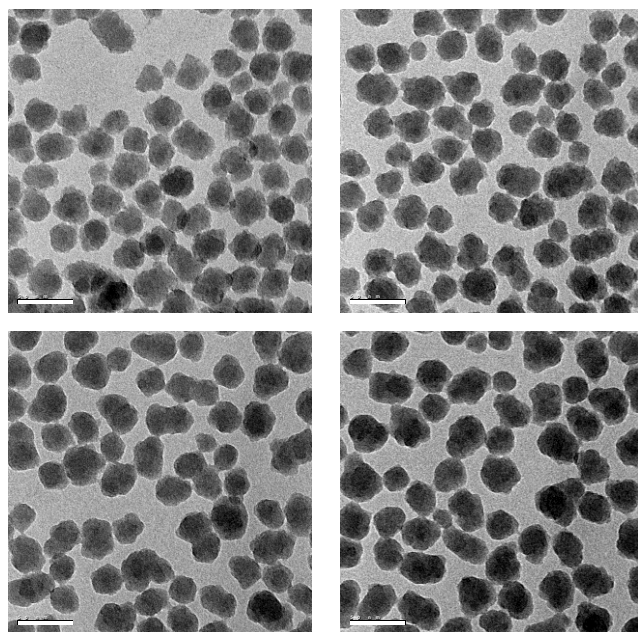


Figure 6.28: SiO₂ NPs 5

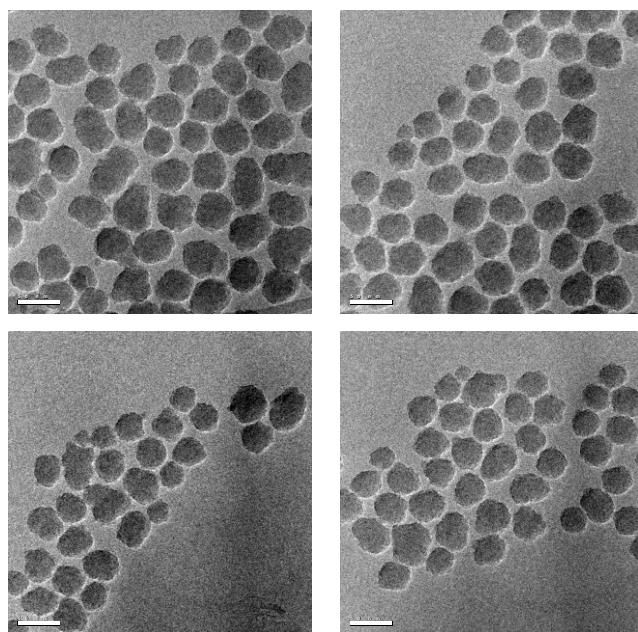


Figure 6.29: SiO₂ NPs 6

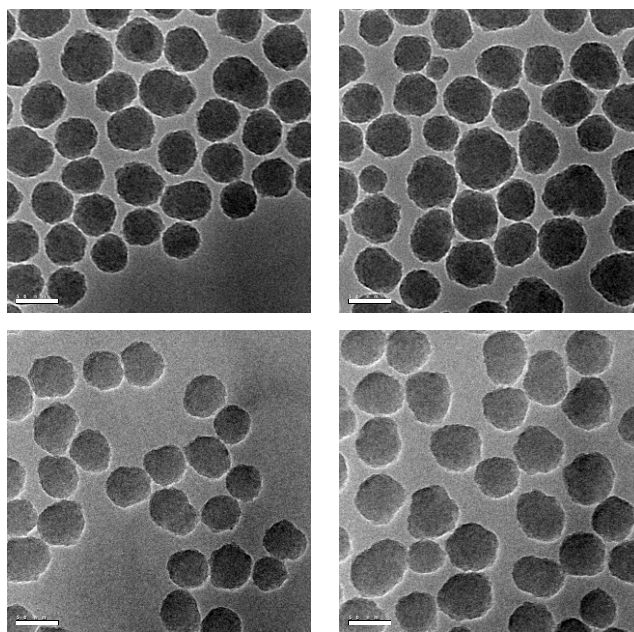


Figure 6.30: SiO₂ NPs 7

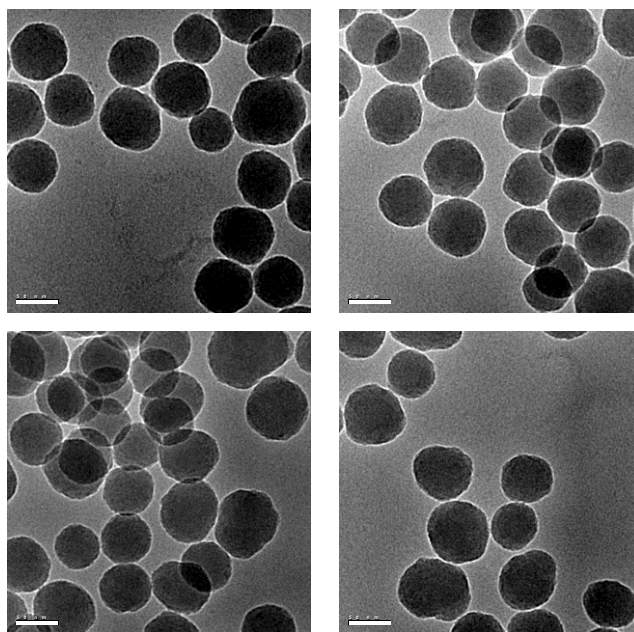


Figure 6.31: SiO₂ NPs 8

We observe that increasing the NH₄OH concentration the regularity of the nanoparticles increases as well as the mean diameter.

For the following part we decided to use the sample **SiO₂ NPs 6** as it represents a good compromise between mean diameter (small enough) and regularity of the morphology. These SiO₂ nanoparticles were functionalized with gold seeds as described before and the gold seeds were grown until forming a gold shell using the Kcarb solution. The volume of Kcarb solution added to the reaction was increased progressively until obtaining a complete and homogeneous gold shell (checked by TEM observations), this was obtained for Sample 3 (by adding 5 mL of Kcarb solution), while on Sample 1 and 2 the gold shell was incomplete. The morphology of these nanoshells is reported on Figure 6.32.

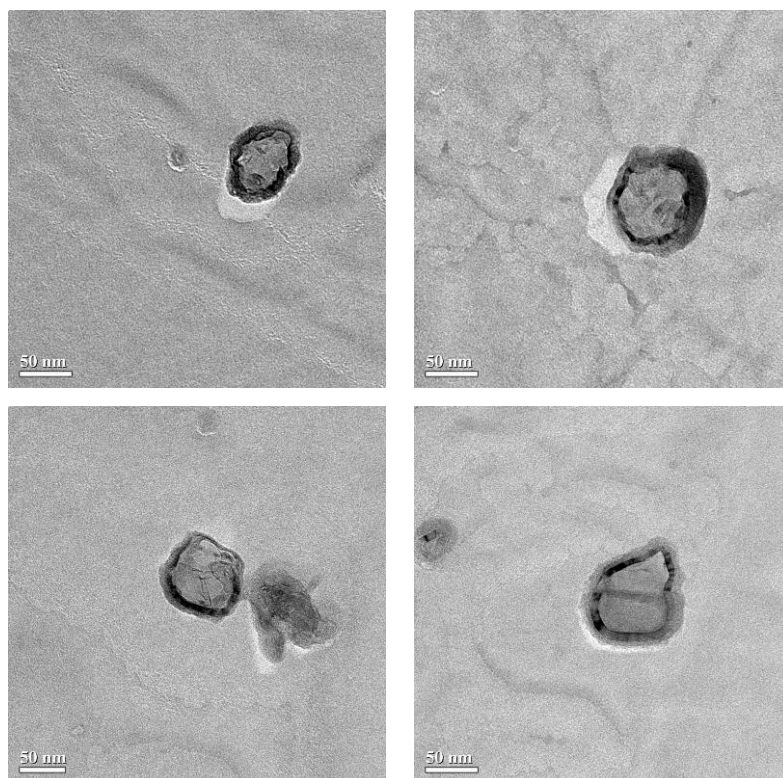


Figure 6.32: TEM pictures of Sample 3 Nanoshells

These Nanoshells have a mean diameter of 45.3 nm (see Figure 6.34), they have a nearly spherical shape and are fairly well dispersed. Moreover the colloidal suspension of Nanoshells in water shows a very strong absorbance peak at 979nm as can be seen on Figure 6.33.

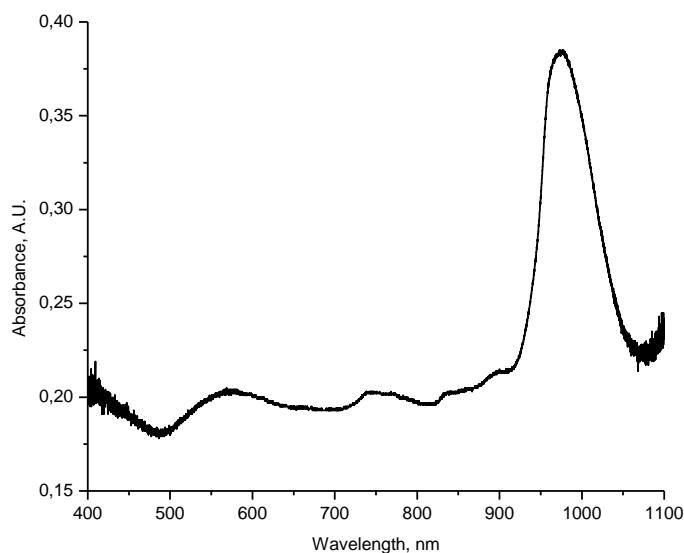


Figure 6.33: UV-Vis spectrum of colloidal suspension of Nanoshells in water

Eventually, the Nanoshells were coated with poly(ethylene glycol) methyl ether thiol (MeO-PEG-SH), using the natural affinity between thiol groups and gold, in order to have a biocompatible device suitable for intravenous administration. The success of the coating was checked using DLS analysis, the size distribution curves of nanoshells before and after coating are reported in Figure 6.34.

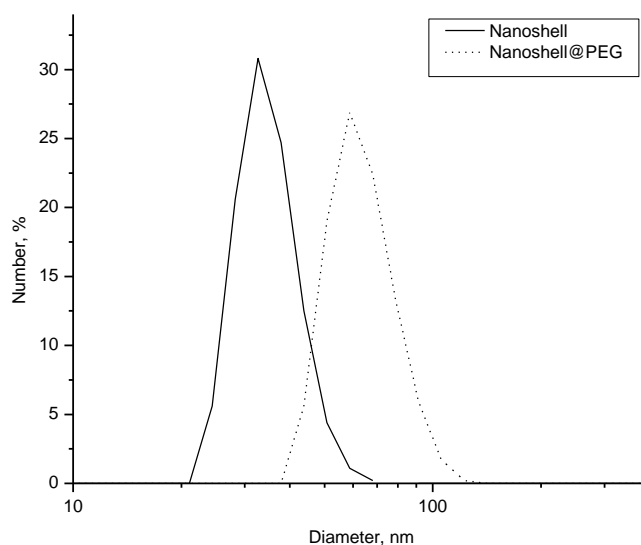


Figure 6.34: DLS analysis of Nanoshells before and after coating with MeO-PEG-SH

The increase in the nanoparticles mean diameter (from 45.3 nm before coating to 74.6 nm afterward) demonstrate the success of the polymeric coating. Moreover the size distribution curve stays fairly narrow which confirms the absence of aggregation. The UV-Vis spectrum of the coated Nanoshells in colloidal suspension shows a shift of the SPR from 979 nm to 972 nm, this variation is not significant for the application we are interested in, staying always in the range of interest.

Conclusions

In a first part, nanoshells were prepared following methods described in literature. SiO₂ nanoparticles of 110 nm diameter were obtained and functionalized with APTES, successively GNPs were grafted on their surface and these GNPs were grown until forming a uniform gold shell. By varying the amount of gold salts added in the last step of the synthesis it was possible to obtain a wide range of shell thicknesses and to study the shift of surface plasmon resonance in function of this parameter. Therefore, we were able to find the correlation between shell thickness and SPR localization. In a second part, the Stöber process was slightly modified in order to obtain smaller nanoparticles, with diameters between 25 nm and 65 nm. In this way it was possible to obtain nanoshells smaller than those reported in literature. In a third part one sample was coated with poly(ethylene glycol) methyl ether thiol, using the natural affinity between thiol groups and gold, in order to have a device suitable for biomedical applications.

References

- [1] Yagci Y., Sangermano M., Rizza G., *Chem. Comm.*, **2008**, 24, 2771.
- [2] Yagci Y., Sangermano M., Rizza G., *Macromolecules*, **2008**, 41, 7268.
- [3] Xiao D., Rong M.Z., Zhang M.Q., *Polymer*, **2007**, 48, 4765.
- [4] De Giglio E., Cometa S., Cioffi N., Torsi L., Sabbatici L., *Anal. Bioanal. Chem.*, **2007**, 389, 2055.

- [5] Du J. Z., Chen Y.M. , Zhang M. Y. H. , Han C. C., Fischer K., Schmidt M., *J. Am. Chem. Soc.*, **2003**, 125, 14710.
- [6] J.Z. Zhang, *J. Phys. Chem. Lett.*, **2010**, 1, 686.
- [7] H. Liang, L. Wan, C. Bai, L. Jiang, *J. Phys. Chem. B*, **2005**, 109, 7795.
- [8] S.J. Oldenburg, R.D. Averitt, S.L. Westcott, N.J. Halas, *Chem. Phys. Lett.*, **1998**, 288, 243-247.
- [9] Y. Wang, W. Qian, Y. Tan, S. Ding, H. Zhang, *Talanta*, **2007**, 72, 1134-1140.
- [10] M.R. Choi, K.J. Stanton-Maxey, J.K. Stanley, C.S. Levin, R. Bardhan, D. Akin, S. Badve, J. Sturgis, J.P. Robinson, R. Bashir, N.J. Halas, S.E. Clare, *Nano. Lett.*, **2007**, 7, 3759-3765.
- [11] H. Wang, J. Kundu, N.J. Halas, *Angew. Chem. Int. Ed.*, **2007**, 46, 9040-9044.
- [12] S. Lal, S. Link, N.J. Halas, *Nature Photonics*, **2007**, 1, 641-648.
- [13] W. Stöber, A. Fink, E. Bohn, *J. Coll. Int. Sci.*, **1968**, 26, 62-69.
- [14] D.J. Wu, X.J. Liu, L.L. Liu, W.P. Qian, *Appl. Phys.*, **2008**, A 92, 279-282.
- [15] D. G. Duff, A. Baiker, *Langmuir*, **1993**, 9, 2301-2309.

Conclusions

As explained in the introduction, the preparation of nanodevices for biomedical application, and more specifically to be at direct contact with blood, imply a certain number of rules and requirements. Particularly, all the materials employed and their method of preparation have to meet precise specifications and characteristics while bringing the innovation needed and potential improvements in the applications of interest.

The first application is hyperthermia for which magnetite nanoparticles were synthesized by a chemical co-precipitation of Fe^{2+} and Fe^{3+} ions under alkaline conditions; magnetization curves showed superparamagnetic property (i.e. no remanence effect) and relatively high magnetization values. The achieved magnetite nanoparticles were coated with PEGDA by UV-activation in water adapting a known methodology to nanoparticles coating for the very first time. It was possible to observe that while the average size of the particles are in the nanometre range, within 3 to 10 nm, the large aggregates of the particles were around 1-2 μm in good agreement with the DLS analyses. The magnetization curves for coated Fe_3O_4 nanoparticles showed that only by increasing the Fe_3O_4 /PEGDA ratio in the system up to a value of 10-15 phr both remanence and coercivity tend to zero and makes the particles suitable for bio-medical applications. This first type of nanoparticles was suitable for hyperthermia but slightly too large for intravenous administration, for this reason and other preparation method was implemented.

Firstly, in order to reduce the aggregation tendency of magnetite it was stabilized with citric acid, which didn't modify the magnetic behaviour. Then, the achieved magnetite nanoparticles were functionalized with vinyl groups by using VTMS, and they were further functionalized via thiol-ene reaction with PEG-SH under UV-activation. The DLS measurements after coating the vinyl- Fe_3O_4 nanoparticles with PEG-SH showed an average size of nanoparticles of about 60 nm, and TEM observations demonstrated that they were well dispersed and did not show strong tendency of microscopic aggregation. The degree of functionalization of the magnetite particles was evaluated through

TGA analysis showing a PEG-shell content which was calculated to be around 60%. Superparamagnetic-like behavior of coated Fe₃O₄ nanoparticles, was ensured by the Brownian motion of magnetic NPs in the ferrofluid and polymeric coating did not modify the magnetic response of the magnetite nanoparticles. These nanoparticles seem to meet all the requirements described before.

Another method was studied which consisted in coating magnetite nanoparticles with a-PEG and a-PCL via click reaction, reacting alkyne groups of the polymers with azide groups on the surface of magnetic NPs. ATR analysis confirmed the presence of a polymeric shell in both cases. The degree of functionalization of the magnetite particles was evaluated through TGA analysis showing a PCL-shell content which was calculated to be around 60% and a PEG-shell content which was calculated to be around 80%. The analysis of the magnetization curves show that the NPs had a superparamagnetic behavior. TEM analysis confirmed the nanometric size and the narrow size distribution of the coated NPs.

The second application considered in this work is photothermal-therapy: Gold-PEGDA core shell particles were prepared in water via a photoinduced electron transfer and free-radical polymerization of an acrylic formulation. DLS measurements reveal the achievement of nanometric size distribution of the synthesized particles. The TEM micrographs showed that the particles are in the nanometric range, within 10 to 50 nm. However the SPR of these NPs was not shifted enough into the NIR to be efficient in this kind of application, for this reason other gold core morphologies were studied.

Hollow gold nanoparticles were synthesized by reduction of gold salts on the surface of cobalt nanoparticles. By varying the reaction parameters we were able to obtain a wide range of diameters and shell thicknesses. In this way it was possible to study the shift of the surface plasmon resonance in function of the variation of these parameters. We found an exponential correlation between the ratio of the external diameter and the internal diameter and the surface plasmon resonance localization, to our knowledge this correlation has never been reported in literature. Moreover, we were able to coat hollow gold NPs

with a biocompatible polymer (PEG). This polymeric coating didn't significantly shift the SPR peak, leaving it in the NIR region which is compulsory for photothermal therapy.

Last but not least, nanoshells were prepared following methods described in literature. SiO₂ nanoparticles of 110 nm diameter were obtained and functionalized with APTES, successively GNPs were grafted on their surface and these GNPs were grown until forming an uniform gold shell. By varying the amount of gold salts added in the last step of the synthesis it was possible to obtain a wide range of shell thicknesses and to study the shift or surface plasmon resonance in function of this parameter. Therefore, we were able to find the correlation between shell thickness and SPR localization. In a second part, the Stöber process was slightly modified in order to obtain smaller nanoparticles, with diameters between 25 nm and 65 nm. In this way it was possible to obtain nanoshells smaller than those reported in literature. In a third part one sample was coated with poly(ethylene glycol) methyl ether thiol, using the natural affinity between thiol groups and gold, in order to have a biocompatible device without significantly shifting the SPR.

The role of the material sciences engineer is to propose new material and devices to biologists and medical researchers following precise specifications, in this perspective I prepared different devices complying with the requirements for biomedical applications; the next step would be now to test these devices *in vitro* and *in vivo* to check if they indeed can bring improvement in cancer therapies.

List of Publications

J. Amici, E. Celasco, P. Allia, P. Tiberto, M. Sangermano.

“Poly(ethylene glycol)-coated magnetite nanoparticles: preparation and characterization”.

Macromolecular Chemistry and Physics, **2011**, 212, DOI: 10.1002/macp.201000707.

J. Amici, P. Allia, P. Tiberto, M. Sangermano.

“Poly(ethylene glycol)-coated Fe₃O₄ nanoparticles by UV-thiol-ene addition of PEG-dithiol on vinyl functionalized magnetite surface”.

Macromolecular Chemistry and Physics, **2011**, 212, DOI: 10.1002/macp.201100072.

J. Amici, M.U. Kahveci, P. Allia, P. Tiberto, Y. Yagci, M. Sangermano.

“Polymer grafting onto magnetite nanoparticles by "click" reaction”.

Journal of Materials Science, **2012**, 47, DOI: 10.1007/s10853-011-5814-z.

J. Amici, M. Sangermano, E. Celasco, Y. Yagci.

“Photochemical synthesis of gold-polyethyleneglycol core-shell nanoparticles”.

European Polymer Journal, **2011**, 47, DOI: 10.1016/j.europolymj.2011.03.007.

Proceedings:

J. Amici, P. Allia, P. Tiberto.

"Preparation and characterization of PEGDA coated magnetic nanoparticles under UV irradiation for diagnosis and treatment of cancer".

European Symposium of Photopolymer Science (ESPS): 28th november - 2nd december 2010, Mulhouse, France.

J. Amici, P. Allia, P. Tiberto, M. Sangermano.

"Fe₃O₄-Polyethyleneglycol coated nanoparticles achieved by UV-thiol-ene addition of PEG-di-Thiol on vinyl functionalized magnetite nanoparticles".

European Congress and Exhibition on Advanced Materials and Processes (EUROMAT), 12th-15th September 2011, Montpellier, France.

J. Amici, P. Allia, P. Tiberto, M. Sangermano.

"Polymeric coated metal oxide and metal nanoparticles for biomedical applications".

Macrogiovani, 13th December 2012, Milan, Italy.

J. Amici, P. Allia, P. Tiberto, Y. Yagci, M. Sangermano.

"Polymeric coated metal oxide and metal nanoparticles for biomedical applications".

European Symposium of Photopolymer Science (ESPS), 04th-07th September 2012, Turin, Italy.

Acknowledgements

Looking back at these three years I can say that it has been a really wonderful time, I wish it never has to end, but here we are..... so I have a lot of person to thank for making all of this possible:

First of all my supervisor, Marco Sangermano, for giving me the opportunity to become a PhD student, trusting me on a subject as new for him as it was for me, leaving me a great freedom to conduct my research while being always available in case of doubts and interrogations, and allowing me to spend three months in Istanbul and one year in Paris, where I met and worked with wonderful people. You really helped me find my professional way and, for that, I am and I will stay extremely grateful!

All my colleagues at Politecnico: Gio', Anna, Igna, Ale, Fede e le due italiane nel cuore, Sophie e Flo, for welcoming me into your group and becoming, through the years, very close friends. Thank you for introducing the bio-girl that I was to the world of material sciences and polymers, working beside you every day have been a lot of fun, and I surely hope it's not over yet!

Prof. Dr. Yusuf Yagci for welcoming me in his lab in Istanbul technical University, and teaching me all about "click chemistry". Muhammet Kahveci for his help and patience in the experimental part, and Cagatay, Mustafa, Selim, Deniz, Gokhan, Gorkem, Kubra, Atilla, Demet, Binnur, for their help and support! Thank you very much guys I really enjoyed these three months with you, I learned a lot and I fell in love with your city!!!

Giancarlo Rizza, Martine Soyer and Henry-Jean Drouin, for welcoming me at LSI (Ecole Polytechnique, Paris); Jean-Eric Wegrowe for accepting to be my second advisor; Marie-Claude Clochard, Thierry Gacoin and Sandrine Perruchas for their scientific help and support; Abdallah (peace, kiss and love), PEC, Enrico (yo, les cocos!!!), Mohamed, Chung, Federico, Francesco, Vincent, Jerome, Haad and Willem, for all the fun, I had the best time with all of you guys! And Marie, I had a great time in Japan with you, and a lot of nice

Acknowledgements

memories!

Paola Tiberto and Paolo Allia for all the work on the magnetic characterization.

And all my friends, old and new, always here supporting me.

Fred, my bank advisor for her infinite patience,...

La Scuola Interpolitecnica for the financial support that allowed me to spent 1 year in Paris and 1 week in Japan.

Giuseppe, for being always by my side, even when we are 10000 km apart....

And of course a special thank goes to all my family, for their support and for always believing in me! And specially to my sister for being my very own psychiatrist and English corrector, I don't know what I'd do without you.....

